Title
Field-Induced Phase Transformations in Relaxor Ferroelectric Single Crystals

Author
Gallagher, John Alfred

Publication Date
2014

Peer reviewed|Thesis/dissertation

UNIVERSITY OF CALIFORNIA

Los Angeles

Field-Induced Phase Transformations in Relaxor Ferroelectric Single Crystals

A dissertation submitted in partial satisfaction of the

requirements for the degree Doctor of Philosophy

in Mechanical Engineering

by

John Alfred Gallagher

2014

ABSTRACT OF THE DISSERTATION

Field-Induced Phase Transformations in Relaxor Ferroelectric Single Crystals

By

John Alfred Gallagher

Doctor of Philosophy in Mechanical Engineering

University of California, Los Angeles, 2014

Professor Christopher S. Lynch, Chair

The goal of this dissertation is to develop a better understanding of the large field behavior and field induced phase transformations in relaxor ferroelectric single crystals. Development of relaxor ferroelectric single crystals requires experimental characterization of the thermo-electro-mechanical behavior to determine the linear coefficients as a function of stress, electric field, and temperature, and the limitations on linear behavior imposed by field driven phase transformations. The characterization of the large field behavior including dielectric loss, material coefficients, non-linear field induced phase transformations, and the mechanical, electrical, and thermal thresholds for linear behavior are discussed in detail. The full characterization of many compositions of $[001]_C$ and $[011]_C$ cut and poled single crystal lead indium niobate – lead magnesium niobate – lead titanate, $x\mathrm{Pb}(\mathrm{In}_{1/2}\mathrm{Nb}_{1/2})\mathrm{O}_3$-$(1-x-y)\mathrm{Pb}(\mathrm{Mg}_{1/3}\mathrm{Nb}_{2/3})\mathrm{O}_3$-$y\mathrm{PbTiO}_3$ (PIN-PMN-PT), is presented and the effect of composition on the field induced phase transformation is discussed. PIN-PMN-PT with low PT concentrations was

found to have a distributed phase transformation over a range of applied fields while PIN-PMN-PT with higher PT concentrations had discontinuous phase transformation behavior. Increasing the PT concentration or decreasing the PIN concentration increased the material coefficients but decreased the transformation threshold. A new approach to characterizing the large field behavior of relaxor ferroelectric single crystals was developed based on a combination of a work-energy based model of the driving forces for the phase transformation together with electric field loading while monitoring strain and electric displacement, and a measurement of mechanical compliance. The model was verified using the results from experimental characterization of PIN-PMN-PT and was found to accurately simulate the phase transformation behavior under combined mechanical, electrical, and thermal loads.

The dissertation of John Alfred Gallagher is approved.

Gregory P. Carman

Nasr Ghoniem

Ertugrul Taciroglu

Christopher S. Lynch, Committee Chair

University of California, Los Angeles

2014

For my beloved wife,

Stephanie

TABLE OF CONTENTS

LIST OF FIGURES

LIST OF TABLES

LIST OF SYMBOLS

E – Electric field

E_C – Electric coercive field

E_i – Electric field tensor

E_3 – Electric field in the crystallographic "3" direction

E_a – Electric field amplitude

E_m – Mean electric field associated with the phase transformation

ΔE – Electric field change

$E_m^{\text{R-O start}}$ – Electric field threshold corresponding to the start of the electric field driven phase transformation

$E_3^{\text{R-O finish}}$ – Electric field threshold corresponding to the end of the electric field driven phase transformation

V_{in} – Input voltage

V_{out} – Output voltage

σ – Stress

σ_{ij} – Stress tensor

σ_{22} – Normal stress in the crystallographic "2" direction

σ_{33} – Normal stress in the crystallographic "3" direction

σ_m – Mean stress associated with the phase transformation

$\Delta\sigma$ – Stress change

$\sigma_{ij}^{\text{R-O start}}$ – Stress threshold corresponding to the start of the stress driven phase transformation

D – Electric displacement

D_i – Electric displacement tensor

D_3 – Electric displacement in the crystallographic “3” direction

D_a – Electric displacement amplitude

ΔD – Change in electric displacement associated with a phase transformation

$\Delta D^{\alpha \rightarrow \beta}$ – Change in electric displacement when transforming from an α-phase to a β-phase

D_3^{el} – Reversible electric displacement

D_3^{s} – Spontaneous electric displacement

$D_3^{R\text{-}O\ start}$ – Electric displacement at the start of the phase transformation

$\hat{D}_3$ – Volume average electric displacement

P – Polarization

P_i – Polarization tensor

P_S – Spontaneous polarization

P_r – Remnant polarization

ε - Strain

ε_{ij} – Strain tensor

ε_{kl}^{r} – Remanent strain

ε_{22} – Axial strain in the crystallographic “2” direction

ε_{33} – Axial strain in the crystallographic “3” direction

$\Delta\varepsilon$ – Change in strain associated with a phase transformation

$\Delta\varepsilon^{\alpha \rightarrow \beta}$ – Change in strain when transforming from an α-phase to a β-phase

ε_{22}^{el} – Reversible strain

ε_{22}^{s} – Spontaneous strain

$\varepsilon_{22}^{\text{R-O start}}$ – Strain at the start of the phase transformation

$\hat{\varepsilon}_{22}$ – Volume average strain

T – Temperature

ΔT – Temperature change

T_{C} – Curie temperature

T_{B} – Burns temperature

$T_{\text{R/T}}$ – Rhombohedral to tetragonal phase transition temperature

S – Entropy

q – Thermal energy

U – Internal energy

ϕ – Internal energy

G – Gibbs function

w – External work

w^{m} – Mechanical work

w^{e} – Electrical work

w^{irr} – Irreversible work

$w^{\alpha\beta}$ – Work required to change from state α to β

w^{C} – Work constant required for transformation to occur

$\Delta w^{\alpha\to\beta}$ – Change in work required to transform from an α-phase to a β-phase

σ^{std} – Standard deviation

s_{ijlk}^{E} – Compliance coefficients

c_{ijkl}^{E} - Stiffness coefficients

d_{ijk} – Piezoelectric coefficients

d_{31} – Piezoelectric 31 mode

d_{32} – Piezoelectric 32 mode

d_{33} – Piezoelectric 33 mode

κ_{ij}^{σ} – Dielectric coefficients

κ^* – Complex dielectric coefficient

κ' – Real dielectric coefficient

κ'' – Imaginary dielectric coefficient

α_{ij}^{E} – Thermal expansion coefficients

q_i^{σ} – Pyroelectric coefficients

Δ – Change

δ – Dielectric phase lag

tan δ – Dielectric loss tangent

L_e – Electrical loss

ω – Angular frequency

f_D^e – Dielectric damping factor

a – Coefficients of the expansion function

Q_{abij} – Electrostrictive coefficients

IDE – Interdigitated electrode

MFC – Macro fiber composite

MEMS – Micro electro-mechanical system

FE_R – Ferroelectric rhombohedral phase

FE_O – Ferroelectric orthorhombic phase

FE_T – Ferroelectric tetragonal phase

FE_M – Ferroelectric monoclinic phase (FE_{MA}, FE_{MB}, FE_{MC})

PE_C – Paraelectric cubic phase

AFE – Antiferroelectric phase

MPB – Morphotropic phase boundary

ABO_3 – Perovskite unit cell structure

AB'B"O_3 – Perovskite unit cell structure

PZ – Lead zirconate, $PbZrO_3$

PT – Lead titanate, $PbTiO_3$

PZT – Lead zirconate titanate, $Pb(Zr_xTi_{1-x})O_3$

PLZT – Lanthanum-doped lead zirconate titanate, $Pb_{1-x}La_x(Zr_{1-y}Ti_y)_{(1-x/4)}O_3$

PMN – Lead magnesium niobate, $Pb(Mg_{1/2}Nb_{2/3})O_3$

PIN – Lead indium niobate, $Pb(Mg_{1/3}Nb_{2/3})O_3$

PMN-PT – Lead magnesium niobate – lead titanate, $(1-x)Pb(Mg_{1/2}Nb_{2/3})O_3$-$xPbTiO_3$

PZN-PT – Lead zinc niobate – lead titanate, $(1-x)Pb(Zn_{1/3}Nb_{2/3})O_3$-$xPbTiO_3$

PIN-PMN-PT – Lead indium niobate – lead magnesium niobate – lead titanate $xPb(In_{1/2}Nb_{1/2})O_3$-$(1-x-y)Pb(Mg_{1/3}Nb_{2/3})O_3$-$yPbTiO_3$

ACKNOWLEDGEMENTS

There are many people who I wish to acknowledge for their support and help in this work. First, I sincerely thank Professor Christopher Lynch for inviting me into his laboratory and allowing me to pursue my academic goals. This work would not be possible without Dr. Lynch's knowledge, support, and advisement. Working with him and learning from him these past few years has been an incredible experience. I would also like to thank my committee members and the many other Professors, colleagues, and laboratory members with whom I have worked closely and collaborated with. My experiences talking to them and learning from them have been highly influential. I would like to acknowledge the support of Progeny Systems and H. C. Materials, through Navy SBIR Grant N00014-12-C-339, for this research.

I am grateful for my friends for offering their support and a means to unwind during the difficult times. I especially thank those I have met during my time in California, even though without them I could have probably finished this work a year earlier.

Most importantly I would like to thank my family for believing in me and supporting me throughout this process. I thank Buster, my dog, for always reminding me during stressful times to take a little break and play. Lastly, I especially want to thank my wife, Stephanie. This could never have been completed without her love, unbelievable patience, and unwavering support.

VITA

EDUCATION

2010 MS, Mechanical Engineering, Boston University, Boston, MA, USA

2005 BS, Mechanical Engineering, Union College, Schenectady, NY, USA

Czech Technical University (via Union College), Prague, CZ

PROFESSIONAL

2010-2014 Graduate Research Assistant, University of California, Los Angeles, Los Angeles, CA, USA

2009-2010 Graduate Research Assistant, *Boston University Orthopedic and Developmental Biomechanics* Laboratory, Boston University, Boston, MA, USA

2008-2012 Engineering Consultant, SignalQuest Inc., Lebanon, NH, USA

2006-2008 Production Manager, SignalQuest Inc., Lebanon, NH, USA

2005-2006 Process Engineer, SignalQuest Inc., Lebanon, NH, USA

REFEREED JOURNAL PUBLICATIONS

[1] Gallagher, J. A. and Lynch, C. S., Combining Experiments and Modeling to Characterize Field Driven Phase Transformations in Relaxor Ferroelectric Single Crystals, *Acta Materialia*, (Submitted: July, 2014).

[2] Gallagher, J. A., Tian, J., and Lynch, C. S., Composition Dependence of Field Induced Phase Transformations in $[011]_C$ PIN-PMN-PT Relaxor Ferroelectric Single Crystals with d_{32} Piezoelectric Mode, *Acta Materialia,* (Accepted: June, 2014).

[3] Gallagher, J. A., Tian, J., and Lynch, C. S., Composition Dependence of Electro-Mechanical Properties and Field Induced Phase Transformations in $[001]_C$ PIN-PMN-PT Single Crystals, *Smart Materials and Structures*, (Accepted: July, 2014).

[4] Gallagher, J. A., Tian, J., and Lynch, C. S., Effects of Composition and Temperature on the Large Field Behavior of $[001]_C$ Relaxor Single Crystals, *IEEE Transactions on Ultrasonics, Ferroelectrics, and Frequency Control*, (Submitted May, 2014).

[5] Gallagher, J. A., Tian, J., and Lynch, C. S., Effects of Composition and Temperature on the Large Field Behavior of $[011]_C$ Relaxor Single Crystals, *Applied Physics Letters*, (Submitted April, 2014).

[6] Gallagher, J. A., Pisani, D. M., Smith-Stewart, B., and Lynch, C. S., Stress and Electric Field Gradient Contributions to Dielectric Loss in Ferroelectrics with Interdigitated Electrodes, *Journal of Intelligent Materials Systems and Structures*, 2014, 10.1177/1045389X14533433.

[7] Gallagher, J. A., Jo, H. R., and Lynch, C. S., Large Field Dielectric Loss in Felaxor Ferroelectric PLZT, *Smart Materials and Structures*, 23, 2014, 035007.

[8] Gallagher, J. A. and Lynch, C. S., Characterization of Ferroelectric Single Crystals with Field Induced Phase Transformations, *Smart Materials and Structures*, 22 (2013) 094004.

[9] Gallagher, J. A., Liu, T. Q., and Lynch, C. S., Effect of Field Driven Phase Transformations on the Loss Tangent of Relaxor Ferroelectric Single Crystals, *Journal of Applied Physics*, 113(8), 2013.

[10] Goljahi, S., Gallagher, J. A., Zhang, S. J., Luo, J., Sahul, R., Hackenberger, W., and Lynch, C. S., A Relaxor Ferroelectric Single Crystal Cut Resulting in Large d_{312} and Zero d_{311} for a Shear Mode Accelerometer and Related Applications, *Smart Materials and Structures*, 21(5), 2012.

CHAPTER 1

INTRODUCTION

1.1. Motivation

Relaxor ferroelectric single crystals are used in the design of high performance ultrasonic and sonar transducers [1-5], as energy harvesters [6], and in industries ranging from aerospace to sporting goods [7-9]. The anisotropic in-plane strain of the $[011]_C$ cut has been used as a test bed to study the behavior of magnetoelectric heterostructures under biaxial strain loading [10, 11]. Relaxor ferroelectric single crystals are highly linear within their operating range, have piezoelectric coefficients an order of magnitude larger than traditional ferroelectric ceramics, and have considerably lower material loss [12, 13]. However, the operating range of these crystals is restricted by field induced phase transformations caused by electrical, mechanical, and thermal loads. Depending on the temperature and composition, single crystals naturally occur in different phases [14]. In transducer applications single crystals undergo electrical, mechanical, and thermal loading that can lead to polarization switching and phase transitions [15-19]. The application of bias external fields can either promote or delay the phase transition of a given composition.

Recent work on improving these materials has focused on the development of binary and ternary compositions and on the addition of dopants with the goal of increasing the thermal operating range and increasing hardening against mechanically and electrically driven phase transformations while maintaining the extraordinary piezoelectric properties. Phase transformations are being explored for use in energy harvesting applications but need to be

avoided in acoustic transducer applications. Characterization of the large field ferroelectric behavior of each composition is needed for the design of devices for specific applications.

A number of single crystal compositions have been experimentally characterized using an external loading combination of stress, electric field, and temperature to determine the contributions of field induced phase transformations to the material behavior [15, 16, 18, 20]. The experimental characterization is often performed using an arrangement that allows for simultaneous application of mechanical, electrical, and thermal loads while measuring the strain and electric displacement. This requires a series of experiments. Electric field is cycled at several preload stresses and stress is cycled at several bias electric fields. This procedure is then repeated at several different temperatures and repeated for different crystallographic orientations. The procedure is very time consuming and requires equipment that may not be readily available to most transducer and crystal designers. It is therefore advantageous to develop a technique that will enable more rapid characterization of new crystals using a simpler experimental approach that reduces the number of experiments required to fully characterize the large field behavior. This work presents the characterization of the large field behavior of several compositions of lead indium niobate – lead magnesium niobate – lead titanate single crystals, $x\mathrm{Pb}(\mathrm{In}_{1/2}\mathrm{Nb}_{1/2})\mathrm{O}_3$-$(1-x-y)\mathrm{Pb}(\mathrm{Mg}_{1/3}\mathrm{Nb}_{2/3})\mathrm{O}_3$-$y\mathrm{PbTiO}_3$ (PIN-PMN-PT). The results of this work are being used to advance the fundamental understanding of the thermodynamics of these field induced phase transformations and being used to validate a model that will reduce the complexity of experimental characterization. The results are used to map out effects of composition and temperature and on the energy barrier to these transformations.

Previous studies by Liu et al. have shown through integration of experimental data that a constant amount of work is required for a phase transformation to occur [21]. This represents

overcoming an energy barrier. This critical energy has been found to be independent of the combination of electric field and stress that induces the transformation. A new characterization method was developed that relies on a model of the underlying mechanism of single crystal behavior including the critical energy barrier for transformation. This results in a more limited set of experiments required for characterization of new compositions. The proposed approach uses a combination of experimental work and modeling to generate the full set of characterization curves, including phase transformations, from data interpolation. Extensive validation of the technique was conducted through experimental characterization of many different crystal compositions and comparison to the predicted values from the model.

1.2. Contents of the Dissertation

In the following chapters experimental techniques are used to characterize various ferroelectric materials including relaxor ferroelectric single crystals, composites, and ceramics. A model is developed to aide in the characterization of new materials by reducing the number of tests required to determine the material behavior under combined mechanical, electrical, and thermal loads. This will expedite characterization of new compositions allowing crystal and transducer designers to more rapidly assess the material behavior and aide in transducer design.

Background literature is reviewed in Chapter 2. The piezoelectric effect is reviewed. Ferroelectricity is discussed in terms of the multiscale governing behavior arising from polarization in the unit cell structure. Ferroelectric phase transformations are discussed in terms of polarization reorientation and domain structure. Previous experimental characterization results are reviewed as well.

Dielectric loss in ferroelectric materials is addressed in Chapter 3. In Chapter 3 a new approach to experimentally characterizing large field dielectric loss is developed and demonstrated for ferroelectric single crystal lead magnesium niobate – lead titanate, $0.68Pb(Mg_{1/3}Nb_{2/3})O_3$-$0.32PbTiO_3$ (PMN-0.32PT), single crystals. The method equates the area within the experimental electric displacement – electric field hysteresis loop to an equivalent area ellipse. The results collapse the measured loss as a function of bias stress and electric field amplitude reasonably close to a single curve. This technique is then used to determine the large field dielectric loss in ferroelectric ceramic lanthanum-doped lead zirconate titanate, $Pb_{0.92}La_{0.08}(Zr_{0.35}Ti_{0.65})_{0.98}O_3$ (PLZT 8/65/35), as a function of preload stress and temperature, and to determine the large field dielectric loss in a commercial lead zirconate titanate, $Pb(Zr_xTi_{1-x})O_3$ (PZT-5A), macro fiber composite (MFC) with interdigitated electrodes (IDEs). This is compared to the large field dielectric loss in a plate of the same ferroelectric material. A finite element model is then used to explain the difference in loss between the MFC and the plate. The results indicate the IDE arrangement has additional loss associated with domain wall motion and ferroelastic switching in the field concentration regions. The finite element model uses a micromechanics based constitutive law.

Experimental characterization of relaxor ferroelectric single crystal PIN-PMN-PT is presented in Chapters 4 and 5, with characterization of the $[011]_C$ cut presented in Chapter 4 and the $[001]_C$ cut presented in Chapter 5. For both crystal cuts the effect of compositional variations near the morphotropic phase boundary that separates the ferroelectric rhombohedral and ferroelectric tetragonal phases on the linear behavior and nonlinear field induced phase transformation behavior was determined under various bias electric field, preload stresses, and temperatures. The material properties are presented. The electric displacement – electric field –

strain – stress behavior is shown as three-dimensional surface plots to demonstrate the effect of composition and temperature on the ferroelectric rhombohedral (FE_R), ferroelectric orthorhombic (FE_O), and phase transformation behavior. The results are presented in terms of a mechanical, electrical, and thermal threshold required to maintain linear behavior and in terms of an energy barrier to the ferroelectric phase transformation.

A new approach to characterizing the large field behavior of relaxor ferroelectric single crystals is presented in Chapter 6. This approach is based on a combination of a work-energy based model of the driving forces for the phase transformation together with electric field loading while monitoring strain and electric displacement, and a measurement of mechanical compliance. The model is verified using the experimental characterization results of PIN-PMN-PT presented in Chapters 4 and 5. This characterization method is based on a combination of a limited number of measurements. Using this combination of a mechanism based model with limited experiments provides a number of benefits. It offers a simplified means of verification of the behavior of individual pieces of as-received materials or a spot check of batches of material received by device manufacturers. It also offers a simplified approach to quality control for crystal producers. The model enables rapid characterization of new compositions, speeding the process of compositional development and characterization.

The final chapter of this dissertation summarizes the major findings of this research. The contributions to the field due to the research presented in this dissertation are discussed.

CHAPTER 2

BACKGROUND

2.1. History of Piezoelectrics and their Applications

In 1880 brothers Jacques and Pierre Curie experimentally observed that a surface charge developed on specially prepared quartz, SiO_2, crystals when placed under a mechanically induced stress [22]. The piezoelectric effect was therefore defined as a surface charge induced by mechanical pressure. Through geometric analysis of the crystals they found that piezoelectricity was a product of non-conducting materials that lack a center of symmetry. Lippmann then determined through a thermodynamic analysis of piezoelectric crystals that the inverse of piezoelectricity must exist as well. In 1881 Lippmann mathematically predicted electrostriction, deformation under an applied electric field, from the fundamental laws of thermodynamics [23]. Following Lippmann's prediction the Curie brothers experimentally confirmed the existence of electrostriction as the converse of the piezoelectric effect [24]. Although the Curie brothers first published their study on piezoelectricity in 1880, it was not until the start of World War I that piezoelectric materials appeared as central components for application design. Langevin designed and built an ultrasonic submarine detector using a transducer made from a mosaic of thin quartz crystals glued between two steel plates [25]. This prototype sonar transducer device was used to transmit a high-frequency signal into water and measure the distance to an object by timing the return echo.

In 1921, Valasek discovered dielectric hysteresis in Rochelle salt which gave rise to ferroelectricity, the development of spontaneous polarization in a material [26]. Since then the

ferroelectric effect has been observed in many other types of materials. Many piezoceramic compounds were studied during World War II with the goal of creating materials with very large dielectric constants for large capacitors. Barium titanate, $BaTiO_3$, was discovered through this research. The large dielectric constant in barium titanate was attributed to the ferroelectric behavior [27, 28]. In the early 1950's lead zirconate titanate, $Pb(Zr_xTi_{1-x})O_3$ (PZT), was discovered and was found to have material properties preferred over barium titanate in sonar applications such as lower dielectric loss and higher Curie temperature [29, 30]. Changing the ratio of lead zirconate, $PbZrO_3$ (PZ), to lead titanate, $PbTiO_3$ (PT), in PZT was found to dramatically change the material properties. In addition, doping with additives such as lanthanum has been shown to change the constitutive behavior and adjust the Curie temperature [31]. Research on compositional changes in PZT led to the discovery of a region of compositions with exceptional piezoelectric behavior, called the morphotropic phase boundary (MPB) [32]. Lead magnesium niobate, $Pb(Mg_{1/2}Nb_{2/3})O_3$ (PMN), was discovered shortly after PZT and is in the class of relaxor ferroelectrics. PMN has been shown to exhibit extraordinary electromechanical properties and reduced hysteresis [12]. In the 1990s researchers began placing PMN in a solid solution with PT to form the binary relaxor ferroelectric single crystal lead magnesium niobate – lead titanate, $(1-x)Pb(Mg_{1/2}Nb_{2/3})O_3$-$xPbTiO_3$ (PMN-*x*PT). This new class of material showed dramatically higher piezoelectric strains than PZT [12]. The high electromechanical coupling and low energy loss and heat generation, made PMN-PT ideal for transducer and actuator design.

PMN-PT with compositions near the MPB on the rhombohedral side (x = 0.28 to 0.33) has a coercive field E_C ~ 0.25 MV/m, a rhombohedral to tetragonal phase transition temperature $T_{R/T}$ < 100°C, and a Curie temperature T_C ~ 150°C [33-36]. The elastic, piezoelectric, and dielectric coefficients have strong temperature dependence and the range of operating electric

field is reduced to zero as $T_{R/T}$ is approached. This has led to the development of ternary crystals with a higher $T_{R/T}$. The addition of lead indium niobate (PIN, T_C ~ 320°C [37]) to PMN-PT has increased $T_{R/T}$ to 137°C and T_C to approximately 200°C [35, 36, 38-40] with minimal degradation of the piezoelectric or electromechanical properties. Ternary lead indium niobate – lead magnesium niobate – lead titanate, xPb($In_{1/2}Nb_{1/2}$)O_3-(1-x-y)Pb($Mg_{1/3}Nb_{2/3}$)O_3-$y$$PbTiO_3$ (PIN-PMN-PT), [41-44] can be grown in large boules with high quality [35, 40, 41]. Ternary PIN-PMN-PT single crystals have higher phase transition thresholds, higher Curie temperatures, and a higher coercive field (E_C up to 0.7 MV/m) [35, 38-40, 45] than binary PMN-PT. This expands the thermal and electrical operating ranges and reduces the temperature dependence of the material constants [35, 46].

2.2. Ferroelectrics

2.2.1. *Perovskite Structure*

Piezoelectricity in crystals only occurs when the crystal does not possess a center of symmetry [47]. Of the 32 crystallographic point groups listed in Table 2-1, 11 of the point groups have a center of symmetry and are therefore non-piezoelectric crystals. Of the remaining 21 non-centrosymmetric groups only one is non-piezoelectric due to other symmetry elements. The piezoelectric effect is observed in the remaining 20 point groups: *1*, *2*, *m*, *222*, *2mm*, *4*, $\bar{4}$, *422*, *4mm*, $\bar{4}2m$, *3*, *322*, *3m*, *6*, $\bar{6}$, *622*, *6mm*, $\bar{6}2m$, *23*, and $\bar{4}3m$. Of the 20 piezoelectric point groups, 10 experience spontaneous polarization and are ferroelectric. These possess a permanent dipole and are point groups: *1*, *2*, *m*, *2mm*, *4*, *4mm*, *3*, *3m*, *6*, and *6mm*. Relaxor ferroelectric materials have structure symmetry in the cubic, tetragonal, rhombohedral, orthorhombic, and

monoclinic crystal systems. Spontaneous polarization is dependent on temperature and is called pyroelectricity. When materials that exhibit spontaneous polarization are heated above the Curie temperature they lose their spontaneous polarization and become paraelectric. The research presented in the following chapters focuses on single crystals with macroscopic *4mm*, *2mm*, and *3m* symmetry.

Table 2-1. Crystallographic classes for piezoelectric and ferroelectric materials. (') indicates a piezoelectric system and (") indicates a system that experiences spontaneous polarization.

Crystal Systems	Point Groups						
Triclinic	1 "	$\bar{1}$					
Monoclinic	2 "	m "	$\frac{2}{m}$				
Orthorhombic	222 '	$2mm$ "	mmm				
Tetragonal	4 "	$\bar{4}$ '	$\frac{4}{m}$	422 '	$4mm$ "	$\bar{4}2m$ '	
Rhombohedral	3 "	$\bar{3}$	322 '	$3m$ "	$\bar{3}m$		
Hexagonal	6 "	$\bar{6}$ '	$\frac{6}{m}$	622 '	$6mm$"	$\bar{6}2m$ '	$\frac{6}{m}mm$
Cubic	23 '	$\frac{2}{m}3$	432	$\bar{4}3m$ '	$\frac{4}{m}3\frac{2}{m}$		

Ferroelectricity is the development of a spontaneous polarization and strain in a material. The polarization can be reoriented between different distinct crystallographic directions through the external application of either mechanical or electrical loads [48-50], known respectively as

ferroelastic and ferroelectric switching. Ferroelectricity generally occurs in a class of crystals called perovskites that have the unit cell crystal structure of ABO_3 or $AB'B''O_3$ in which the unit cell is composed of a small tetravalent metal ion, B, placed within a lattice of larger divalent metal ions, A, at the $<111>_C$ corners and oxygen atoms at the centers of the $\{001\}_C$ faces. Piezoelectricity arises from charge displacement about the center of the unit cell. For example, PT has a perovskite structure with oxygen on the face centers, lead at the eight corners, and titanium at the center of the unit cell. A dipole forms when the material is placed under an electric field. The titanium ion displaces from the neutral cubic position at the center of the unit cell to balance charge. The other atoms in the perovskite structure can deviate from their respective neutral positions as well. This displacement causes strain and polarization of the unit cell.

Long-range Coulomb forces favor ferroelectric states while short-range repulsions prefer the undistorted paraelectric cubic state [51, 52]. Ferroelectricity in PT arises from the Pb-O and Ti-O hybridizations weakening the short-range repulsions causing the long-range forces to dominate and promote ferroelectric behavior. PT has larger remanent strains and remanant polarizations than barium titanate. This is thought to be because the two hybridization effects in PT (Pb-O and Ti-O) have a greater effect on reducing the short range repulsions than the one hybridization effect in barium titanate (Ti-O). The short range repulsion in barium titanate is stronger than in PT.

2.2.2. *Multiscale Governing Behavior*

Single crystals are defined by being made entirely of a repetitive crystal lattice. The lattice is continuous in three dimensions throughout the material. Single crystals are therefore constructed of a single grain. Grain boundaries in polycrystalline ferroelectric materials have been shown to give rise to residual strains between grains caused due to incompatibilities between the electric field induced strains between grains with different crystallographic orientations. The lack of defects and residual strains associated with grain boundaries gives rise to unique properties, resulting in many single crystals being useful for technological applications such as optics and electronics.

Ferroelectric material behavior is governed by multiscale phenomena where microscopic behavior governs the macroscopic constitutive behavior. Understanding the behavior at each length scale enables the development of multiscale models. Ferroelectric ceramics consist of a large number of single crystal grains where the macroscale ferroelectric effect arises from the volume average of the contributions of individual grains. Each grain is connected to neighboring grains resulting in localized stresses and electric fields. The polarization of each grain is not uniform. Each grain contains domains which are regions of similar polarization. The polarization of each grain can be represented as the volume average of the polarization its domains. The polarization of each domain arises from the dipole moment per unit volume of each unit cell. The multiscale behavior of the ceramic is depicted in Figure 2-1.

In the unit cell the separation of the dipole charges is directly related to the spontaneous strain and polarization. Unit cells with the same spontaneous polarization orientations group together forming domains, reducing the elastic and electrostatic energy. The boundary between two adjacent domains is called a domain wall. Domain wall orientation aligns with certain

crystallographic planes that reduce the internal strains and depolarizing internal fields [48]. Numerous domains tend to form in a single specimen. Polarization reorientation occurs when an applied field exceeds the coercive field. This is the result of the polarization switching to another variant, or possibly to another phase. This effect is not a homogeneous process. Domain walls are either already present or they must nucleate. With the increase of field the domain walls then sweep through the crystal as the polarization of each unit cell reorients. Figure 2-2 shows a simplified schematic of a single tetragonal unit cell of PT undergoing a phase transformation as it is cooled and then having its polarization switched from that of one crystal variant to another under electrical and mechanical loading. Spontaneous polarization and strain occur as the material is cooled below the Curie temperature (T_C) as shown in Figures 2-2 (a) and (b). The spontaneous polarization and strain can align with any one of the $[001]_C$ directions. This defines the six tetragonal variants of the ferroelectric tetragonal crystal. Application of an electric field can induce 180° switching between variants, shown in Figure 2-2(c), and can induce 90° switching through different orientations of the applied electric field. Stress can induce only 90° switching between variants, shown in Figure 2-2(d). The red arrows in Figure 2-2 show the direction of spontaneous polarization, P_s.

The composition vs. temperature phase diagrams of many ferroelectric materials display morphotropic phase boundaries. These boundaries represent compositions where multiple phases can coexist. Certain relaxor ferroelectric single crystals have a MPB that separates a tetragonal from a rhombohedral structure. Multiple phases can exist at the MPB including orthorhombic and monoclinic. The presence of an MPB increases the possible polarization directions and typically enhances the electromechanical properties [53, 54]. Application of fields above a

certain threshold can induce phase transformations, where each phase is defined by distinct crystal symmetry and associated dielectric, piezoelectric, and elastic properties.

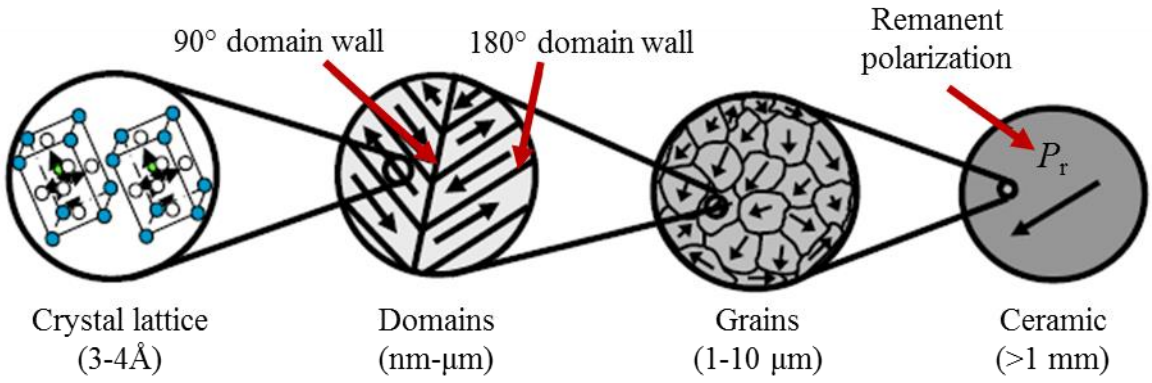

Figure 2-1. Primary length scales and multiscale governing behavior of ferroelectric materials [55].

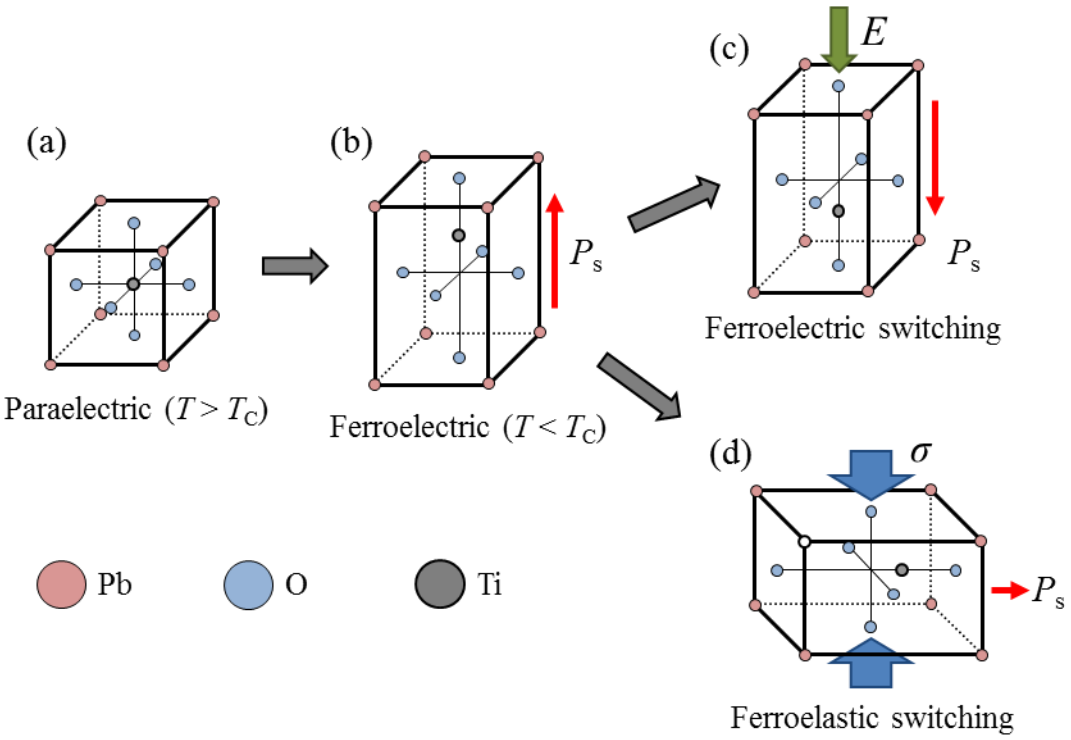

Figure 2-2. Idealized ferroelectric unit cell of PT. (a) At high temperatures the unit cell is cubic and exhibits no polarization. (b) When cooled below the Curie temperature the unit cell exhibits spontaneous polarization. One of the tetragonal variants is populated. Application of (c) electric field and (d) stress can cause 180° ferroelectric switching and 90° ferroelastic switching, respectively. Distortion of the unit cell is exaggerated for visualization purposes.

2.2.3. *Thermodynamics and Devonshire Theory*

The thermodynamic framework used by Devonshire to describe ferroelectricity is used extensively in the work presented in this dissertation on the development of a new characterization technique and is therefore discussed in some detail. Devonshire Theory has been used in phenomenological models of phase transformations [56-58]. The behavior of ferroelectric materials can be described using a thermodynamics based approach outlined by

Devonshire [59]. The internal energy, U, of a body under mechanical, electrical, and thermal loads can be written in differential form, equation (2-1),

$$\mathrm{d}U = \sigma_{ij}\mathrm{d}\varepsilon_{ij} + E_m\mathrm{d}D_m + T\mathrm{d}S\,, \tag{2-1}$$

where σ_{ij} is the stress, E_m is the electric field, ε_{ij} is the strain, D_m is the electric displacement, T is the temperature, and S is entropy. The dependent variables can be expressed by taking the partial derivatives of the internal energy as shown in equations (2-2) through (2-4),

$$\sigma_{ij} = \frac{\partial U}{\partial \varepsilon_{ij}}, \tag{2-2}$$

$$E_m = \frac{\partial U}{\partial D_m}, \tag{2-3}$$

$$T = \frac{\partial U}{\partial S}. \tag{2-4}$$

In this case the dependent variables are stress, electric field, and temperature, while the independent variables are strain, electric displacement, and entropy.

The Gibbs energy function defines the energy available to do work and can be expressed as equation (2-5),

$$G = U - \sigma_{ij}\varepsilon_{ij} - E_m D_m - TS\,. \tag{2-5}$$

Several Gibbs functions can be defined depending on the chosen dependent and independent variables. For the purposes of this analysis the dependent variables are strain (ε_{ij}), electric field (E_m), and entropy (S), the independent variables are stress (σ_{kl}), electric displacement (D_n), and temperature (T), and are used to define the "elastic" Gibbs function. A series expansion of the Gibbs function yields the constitutive laws governing the ferroelectric behavior. The Gibbs free energy is a thermodynamic potential useful for the description of phase transformations. Strain, electric field, and entropy are respectively expressed as equations (2-6) through (2-8),

$$\begin{aligned}\varepsilon - \varepsilon_0 = {} & \frac{\partial \varepsilon_{ij}}{\partial \sigma_{kl}}\sigma_{kl} + \frac{\partial \varepsilon_{ij}}{\partial D_n}D_n + \frac{\partial \varepsilon_{ij}}{\partial T}\left(T - T_0\right) + \frac{1}{2!}\left[\frac{\partial^2 \varepsilon_{ij}}{\partial \sigma_{kl}\partial \sigma_{qr}}\sigma_{kl}\sigma_{qr} + \frac{2\partial^2 \varepsilon_{ij}}{\partial \sigma_{kl}\partial D_n}\sigma_{kl}D_n\right. \\ & \left. + \frac{2\partial^2 \varepsilon_{ij}}{\partial \sigma_{kl}\partial T}\sigma_{kl}\left(T - T_0\right) + \frac{\partial^2 \varepsilon_{ij}}{\partial D_n \partial D_o}D_n D_o + \frac{2\partial^2 \varepsilon_{ij}}{\partial D_n \partial T}D_n\left(T - T_0\right) + \frac{\partial^2 \varepsilon_{ij}}{\partial T^2}\left(T - T_0\right)^2\right] + \cdots\end{aligned}, \tag{2-6}$$

$$\begin{aligned}E - E_0 = {} & \frac{\partial E_m}{\partial \sigma_{kl}}\sigma_{kl} + \frac{\partial E_m}{\partial D_n}D_n + \frac{\partial E_m}{\partial T}\left(T - T_0\right) + \frac{1}{2!}\left[\frac{\partial^2 E_m}{\partial \sigma_{kl}\partial \sigma_{qr}}\sigma_{kl}\sigma_{qr} + \frac{2\partial^2 E_m}{\partial \sigma_{kl}\partial D_n}\sigma_{kl}D_n\right. \\ & \left. + \frac{2\partial^2 E_m}{\partial \sigma_{kl}\partial T}\sigma_{kl}\left(T - T_0\right) + \frac{\partial^2 E_m}{\partial D_n \partial D_o}D_n D_o + \frac{2\partial^2 E_m}{\partial D_n \partial T}D_n\left(T - T_0\right) + \frac{\partial^2 E_m}{\partial T^2}\left(T - T_0\right)^2\right] + \cdots\end{aligned}, \tag{2-7}$$

and

$$S - S_0 = \frac{\partial S}{\partial \sigma_{kl}}\sigma_{kl} + \frac{\partial S}{\partial D_n}D_n + \frac{\partial S}{\partial T}(T - T_0) + \frac{1}{2!}\left[\frac{\partial^2 S}{\partial \sigma_{kl}\partial \sigma_{qr}}\sigma_{kl}\sigma_{qr} + \frac{2\partial^2 S}{\partial \sigma_{kl}\partial D_n}\sigma_{kl}D_n + \frac{2\partial^2 S}{\partial \sigma_{kl}\partial T}\sigma_{kl}(T - T_0) + \frac{\partial^2 S}{\partial D_n \partial D_o}D_n D_o + \frac{2\partial^2 S}{\partial D_n \partial T}D_n(T - T_0) + \frac{\partial^2 S}{\partial T^2}(T - T_0)^2\right] + \cdots \quad \text{. (2-8)}$$

Devonshire [59] originally explained the phase transformations in $BaTiO_3$ by using a sixth order expansion of the Gibbs energy in terms of polarization. This series expansion with respect to polarization as the order parameters is expressed in equation (2-9),

$$\Delta G = a_{ij}P_iP_j + a_{ijkl}P_iP_jP_kP_l + a_{ijklmn}P_iP_jP_kP_lP_mP_n - Q_{abij}\sigma_{ab}P_iP_j - E_mP_m, \quad \text{(2-9)}$$

where *a* are the coefficients of the expansion function, *Q* are the electrostrictive coefficients, and the higher order terms are used to describe the effect of the crystal structure on the ferroelectric behavior. The coefficients have been well documented in previous studies for a number of materials. Phase transformations and nonlinearities in the material behavior are characterized by discontinuities in the derivatives of the Gibbs free energy function. In equation (2-9) electric displacement is replaced by polarization, *P*, because $P >> \varepsilon_0 E$, when $D = \varepsilon_0 E + P$ and ε_0 is the permittivity of free space (ε_0 = 8.854e-12 Fm^{-1}). Using reduced notation, the Gibbs expansion can be written as equation (2-10),

$$\begin{aligned}\Delta G = {} & a_1\left(P_1^2 + P_2^2 + P_3^2\right) + a_{11}\left(P_1^4 + P_2^4 + P_3^4\right) + a_6\left(P_1^6 + P_2^6 + P_3^6\right) \\ & + a_{12}\left(P_1^2 + P_2^2 + P_3^2\right)^2 + a_{112}\left(P_1^2 + P_2^2 + P_3^2\right)^3 + a_{123}\left(P_1^2P_2^2P_3^2\right). \\ & + \ldots + \textit{higher order terms}\end{aligned} \quad \text{(2-10)}$$

Linear piezoelectric constitutive laws are obtained by neglecting temperature and higher order terms. The partial derivatives represent various material constants. Substituting the material constants for the partial derivatives into the Gibbs function for the case of linear piezoelectricity gives equation (2-11),

$$G = \frac{1}{2} s^{E}_{ijkl} \sigma_{ij} \sigma_{kl} + d_{mij} E_m \sigma_{ij} + \frac{1}{2} \kappa^{\sigma}_{mn} E_m E_n . \tag{2-11}$$

The associated piezoelectric constitutive laws, neglecting temperature, are given by equations (2-12) and (2-13),

$$\varepsilon_{ij} = s^{E}_{ijkl} \sigma_{kl} + d_{ijm} E_m + \varepsilon^{r}_{ij} \tag{2-12}$$

and

$$D_m = d_{mij} \sigma_{ij} + \kappa^{\sigma}_{mn} E_n + D^{r}_{m} , \tag{2-13}$$

where ε_{ij} is the total linear strain, ε^{r}_{ij} is the remanent strain, s_{ijkl} is the compliance, d_{ijm} is the piezoelectric coefficient, D_m is the total linear electric displacement, D^{r}_{m} is the remanent electric displacement, and κ_{mn} is the dielectric permittivity. The subscript indices range from 1 to 3. Superscripts E, and σ respectively refer to constant electric field and stress. The material constants are respectively defined as equations (2-14) through (2-16),

$$s_{ijkl}^{E} = \frac{\partial \varepsilon_{ij}}{\partial \sigma_{kl}}, \tag{2-14}$$

$$d_{mij} = \frac{\partial \varepsilon_{ij}}{\partial E_m} = \frac{\partial D_m}{\partial \sigma_{ij}}, \tag{2-15}$$

and

$$\kappa_{mn}^{\sigma} = \frac{\partial D_n}{\partial E_m}. \tag{2-16}$$

2.2.4. *Relaxor Ferroelectrics*

Relaxor ferroelectric single crystals exhibit piezoelectric and electromechanical properties superior to those of ferroelectric ceramics, and reduced hysteresis due to their crystal symmetry [12, 60, 61]. They are distinguished from other ferroelectrics by their frequency dependent dielectric response and diffuse phase transition about the Curie temperature [62]. These single crystals are used in advanced sonar transducers and medical ultrasound transducers [1-5], as energy harvesters [6], and the anisotropic in-plane strain of the $[011]_C$ cut has been used to study the behavior of magnetoelectric heterostructures under biaxial strain loading [10, 11]. Electrical, mechanical, and thermal loading can lead to phase transitions [15-19]. Although this limits the linear behavior desired in acoustic transducer applications, it provides extraordinarily large changes of polarization and strain that are beneficial to energy harvesting and

magnetoelectric applications. The phase transition coincides with a decrease in the compliance, piezoelectric, and dielectric coefficients by nearly an order of magnitude [16, 63].

Relaxor ferroelectric single crystals loaded in certain crystallographic directions exhibit reduced hysteresis due to the near elimination of domain wall motion associated with the crystal symmetry [12]. This results in a region with linear behavior and very low loss. Dielectric loss is an important metric in transducer design. Dielectric loss is commonly expressed as tan δ, where δ is a measurement of the phase lag between the applied electric field, E, and the resulting electric displacement, D, under sinusoidal loading [64, 65]. Larger dielectric loss reduces the quality factor, Q, in resonant devices. Härdtl found that losses in ferroelectric ceramics are dominated by domain wall motion [66]. Domain engineered single crystals are designed to minimize the driving forces for domain wall motion and reduce or eliminate dielectric loss [12, 63, 67].

2.2.5. *Phase Transformations*

Relaxor ferroelectrics display a phase transition when cooled from the cubic phase that is distributed about a mean Curie temperature [62]. Chemical heterogeneity at the nanometer length scale is understood to be the origin of the broad Curie temperature region and frequency-dispersive properties of relaxor ferroelectrics [68, 69]. The material behavior and crystal structure are temperature dependent. At high temperatures the material is paraelectric. A transformation from paraelectric to the ergodic relaxor phase occurs when cooled below the Burns temperature. This cooling results in the development of nanoscale polar regions associated with randomly distributed dipoles that give rise to enhanced dielectric and piezoelectric behavior

[69]. Spontaneous polarization develops as temperature is reduced below the Curie temperature (T_C ~ 200°C for PIN-PMN-PT) and the material enters a ferroelectric phase. When the temperature is below the rhombohedral to tetragonal phase transformation temperature ($T_{R/T}$ ~ 137°C for PIN-PMN-PT), ferroelectric crystals with ferroelectric tetragonal structure transform to ferroelectric rhombohedral and exhibit large coercive fields (E_C up to 0.7 MV/m for PIN-PMN-PT) [35, 36, 38-40]. It has been proposed that spatially distributed chemical and structural heterogeneities may contribute to the observed distributed field-induced phase transformations as well [70].

Mechanical and electrical loading above a certain threshold can induce phase transformations in ferroelectric single crystals. Similar to thermally induced phase transformations, when a field induced phase transformation occurs the polarization vector does not switch within a family of crystallographic directions associated with that phase, but transitions to a different set of crystallographic directions associated with a different crystal phase. Figure 2-3 shows the different crystal variants of the paraelectric cubic (PE_C) phase: the ferroelectric rhombohedral (FE_R), ferroelectric orthorhombic (FE_O), and ferroelectric tetragonal (FE_T) phases. In Figure 2-3 the spontaneous strain of the unit cells has been greatly exaggerated for visualization purposes. Figures 2-4 (a) and (b) show the binary phase diagram for PMN-PT [71] and the ternary phase diagram for PIN-PMN-PT at room temperature [72]. PMN-PT single crystals exhibit the PE_C, FE_R, FE_O, FE_T, and ferroelectric monoclinic (FE_M) phases depending on composition and temperature. Similarly, at room temperature PIN-PMN-PT exhibits the FE_R and FE_T phases depending on composition. In compositions near the MPB, electric field or stress of sufficient amplitude and orientation can drive phase transformations.

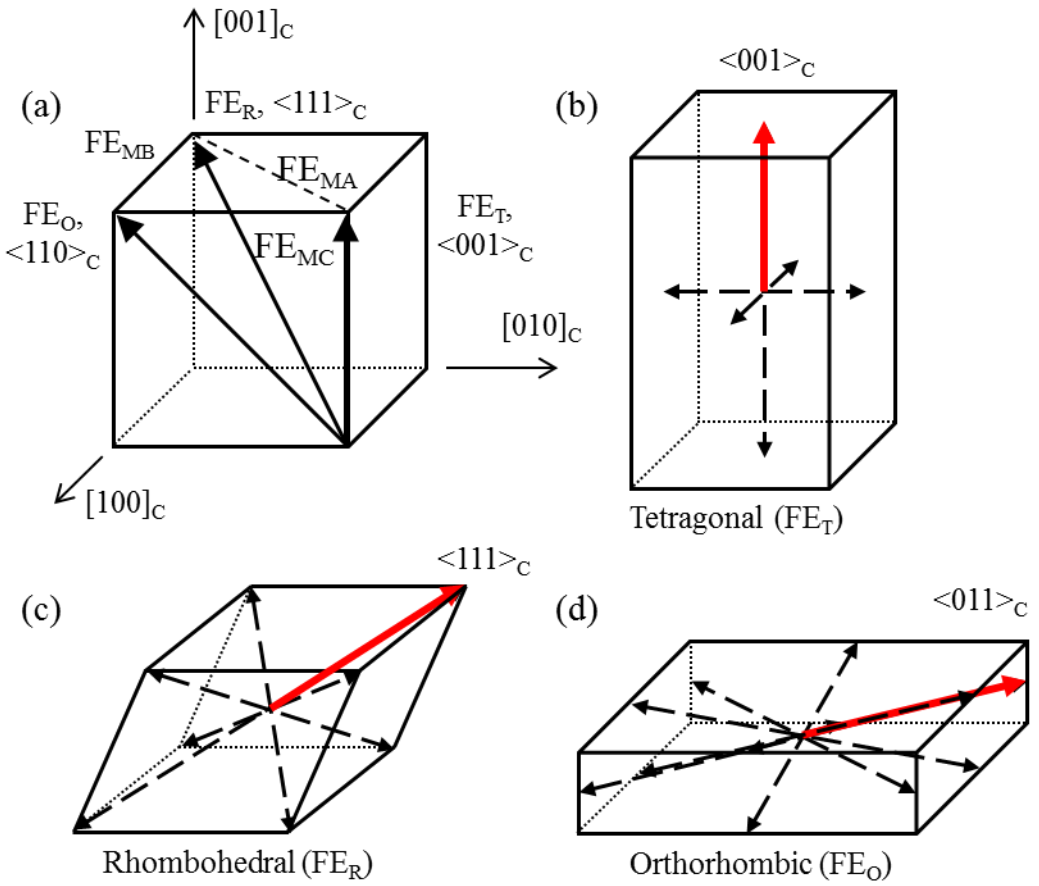

Figure 2-3. Polarization directions in terms of (a) the reference directions for the cubic (no polarization) unit cell, and for (b) FE_R, (c) FE_O, and (d) FE_T phases. The spontaneous strain of the unit cells have been greatly exaggerated for visualization purposes. For (b), (c), and (d) the black dotted arrows show the family of polarization variants for the given phase while the red arrow indicates a possible populated variant for the exaggerated unit cell structure.

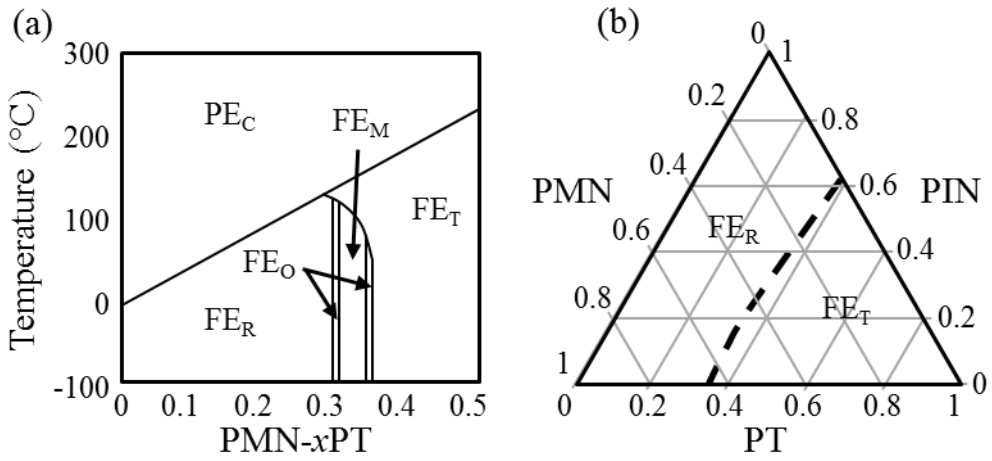

Figure 2-4. Phase transformation diagram for (a) PMN-PT [71] as a function of composition and temperature and (b) PIN-PMN-PT [72] at room temperature.

The $[001]_C$ and $[011]_C$ crystal cuts are of particular interest in relaxor rhombohedral single crystals. The $[001]_C$ and $[011]_C$ cut and poled crystals are referred to as "domain engineered". Domain engineered single crystals that are loaded in certain crystallographic directions exhibit reduced hysteresis due to the near elimination of domain wall motion. This is associated with the crystal symmetry [12] and results in a regime with linear behavior and very low loss. The concept of domain engineering is described using Figure 2-5. The $[001]_C$ cut and poled single crystals are initially poled in the $[001]_C$ direction as shown in Figure 2-5(a). When the crystal is poled, only four of the $<111>_C$ FE_R variants are populated and the volume average remanent polarization is in $[001]_C$. Application of compressive stress (σ_{33}) in the $[001]_C$ direction at amplitudes larger than the coercive stress induces a phase transformation. The polarization is forced into the four $<110>_C$ directions associated with variants of the ferroelectric orthorhombic phase (FE_O), as shown in Figure 2-5(b). Application of electric field (E_3) in the $<001>_C$ direction induces a phase transformation back to FE_R as shown in Figure 2-5(c).

$[011]_C$ cut and poled single crystals depicted in Figure 2-5(d), are made by cutting the single crystal at a 45 degree rotation about $[100]_C$. The crystal is then poled in the $[011]_C$ direction. Two of the $<111>_C$ FE_R variants are populated with the volume average remanent polarization in the $[011]_C$ direction. Compressive stress (σ_{22}) in the $[100]_C$ direction induces a rhombohedral to orthorhombic phase transformation (FE_R-FE_O) where only the $[011]_C$ FE_O variant is populated as shown in Figure 2-5(e). Application of electric field (E_3) in the $[011]_C$ direction induces the same FE_R-FE_O transformation as shown in Figure 2-5(f). In $[001]_C$ cut and poled single crystals, mechanical loading drives the FE_R to FE_O transformation and the electrical loading drives the reverse FE_O to FE_R transformation. These are referred to as antagonistic driving forces to the phase transformations while in $[011]_C$ cut and poled single crystals, mechanical and electric loads work cooperatively to induce the FE_R to FE_O transformation.

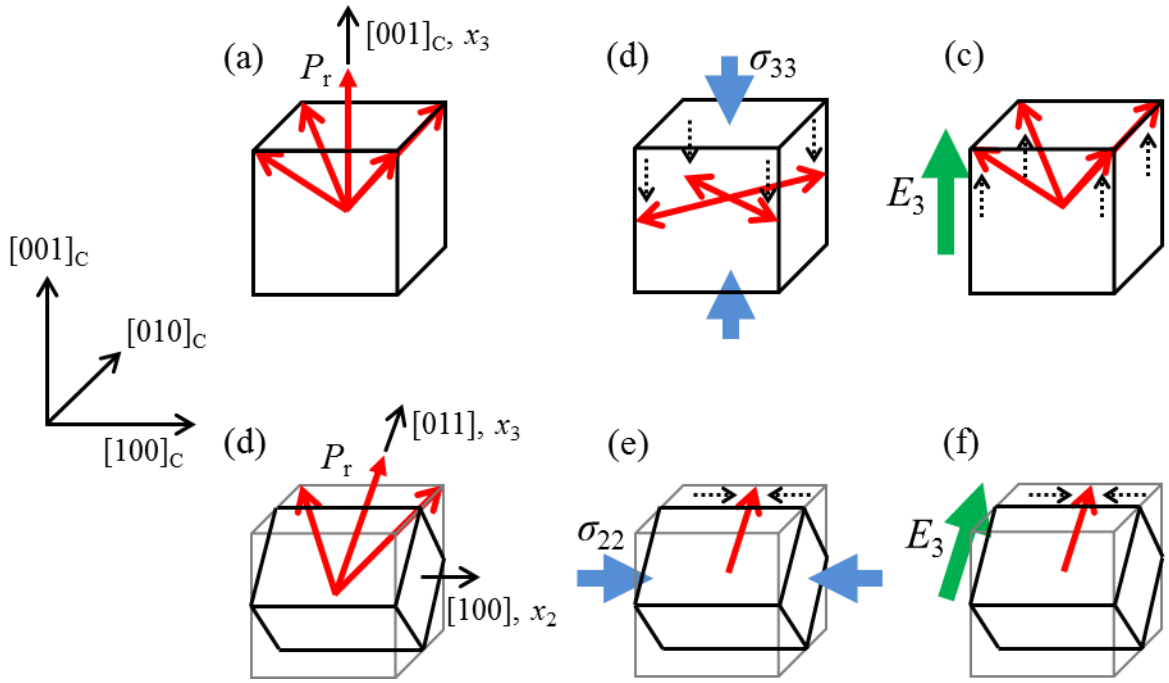

Figure 2-5. Domain states and field driven transformations for $[001]_C$ ((a), (b), and (c)) and $[011]_C$ ((d), (e), and (f)) cut and poled ferroelectric single crystals under mechanical and electrical loading. The schematics shown are of a quasi-cubic lattice for simplification. When polarized in the rhombohedral or orthorhombic variants, the unit cell structures deform and are no longer cubic.

The $[001]_C$ cut and poled single crystal have piezoelectric coefficients designated d_{33}, and the $[011]_C$ cut and poled single crystals have piezoelectric coefficients designated d_{32}. The coordinate axes are indicated in Figure 2-5 for these two cuts. The compositions of PIN-PMN-PT that are studied in this research are in the ferroelectric rhombohedral phase (FE_R) at room temperature under zero electrical or mechanical loads.

Compositions of lead zinc niobate – lead titanate, $(1\text{-}x)Pb(Zn_{1/3}Nb_{2/3})O_3\text{-}xPbTiO_3$ (PZN-PT), with x = 0.045 [73, 74], and xPIN-(1-x-y)PMN-yPT, with x = 0.24 and y = 0.32, single

crystals [75, 76] that are near the ferroelectric rhombohedral – ferroelectric tetragonal (FE_R-FE_T) MPB display discontinuous phase transformations with well-defined forward and reverse coercive fields. In these discontinuous transformations the materials undergoes a sharp jump from one phase to another as the applied load is increased or decreased past the forward or reverse coercive field. Figure 2-6(a) displays a discontinuous phase transformation strain behavior in electrically loaded $[011]_C$ cut and poled PZN-0.045PT [63] with zero stress preload. PMN-0.32PT [16, 69] displays a distributed and nearly continuous phase transformations. As the applied field is increased the phase transition occurs gradually over a range of field values without a well-defined forward or reverse coercive field. Figure 2-6(b) shows the distributed type phase transformation strain behavior of electrically loaded $[011]_C$ cut and poled PMN-0.32PT at a stress preload of -28 MPa in compression [16]. The electric displacement – electric field plots show similar phase transformation profiles. In Figure 2-6 the red hashed lines show the linear rhombohedral phase, the blue dotted lines show the linear orthorhombic phase, and the black solid lines show the phase transformation region.

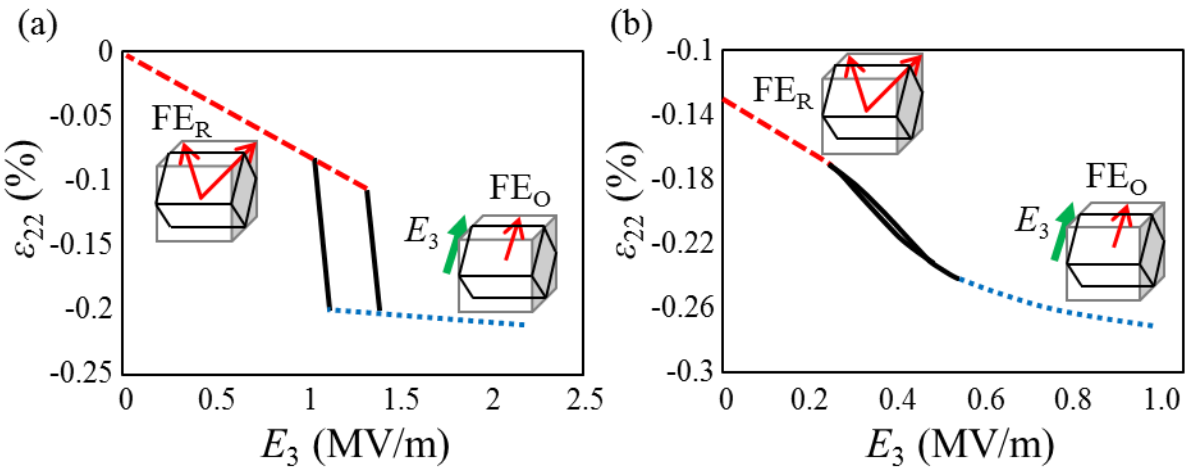

Figure 2-6. Electric field driven phase transformation strain behavior in $[011]_C$ cut and poled (a) PZN-0.045PT [63] at zero mechanical preload displaying a sharp jump type phase transformation and (b) PMN-0.32PT [16] at a mechanical preload of -28 MPa in compression displaying a gradual phase transformation. Note the scaling difference along the electric field and strain axes.

The data plotted in Figure 2-6 are not sufficient for full characterization of the linear response and the phase transformation behavior of the material. Full characterization requires running multiple electric field cycles at different preload stresses and multiple stress cycles at different bias electric fields while measuring the strain and electric displacement. This process is repeated at different temperatures to fully characterize the constitutive behavior in the range of stresses, electric fields, and temperatures used in a particular design. The E_3-σ_{22}-ε_{22} characterization of $[011]_C$ cut and poled PMN-0.32PT at 40°C is shown in Figure 2-7 [16]. The electric displacement characterization profile is similar. The linear regions are associated with the FE_R and FE_O phases. These are connected by a nonlinear phase transformation region.

McLaughlin et al. [16, 20] (for PMN-PT single crystals), and Dong et al. [6] (for PIN-PMN-PT single crystals) showed that there is a linear relationship between the stress and electric field induced transformation thresholds for both forward and reverse loading. When the start coercive fields of the forward FE_R-FE_O and reverse FE_O-FE_R transformations are plotted in the stress – electric field plane, a linear relationship is apparent and the width of the hysteretic region appears constant. This is shown in Figure 2-8 [6]. The red dashed line shows the locus of the forward loading stress and electric field values for the start of the FE_R-FE_O phase transformation to occur while the blue dotted line shows the reverse loading values for the start of the FE_O-FE_R phase transformation to occur. The horizontal arrow, $\Delta\sigma$, and vertical arrow, ΔE, denote the hysteresis between the forward and reverse mechanical and electrical loading paths at constant electric field and stress, respectively.

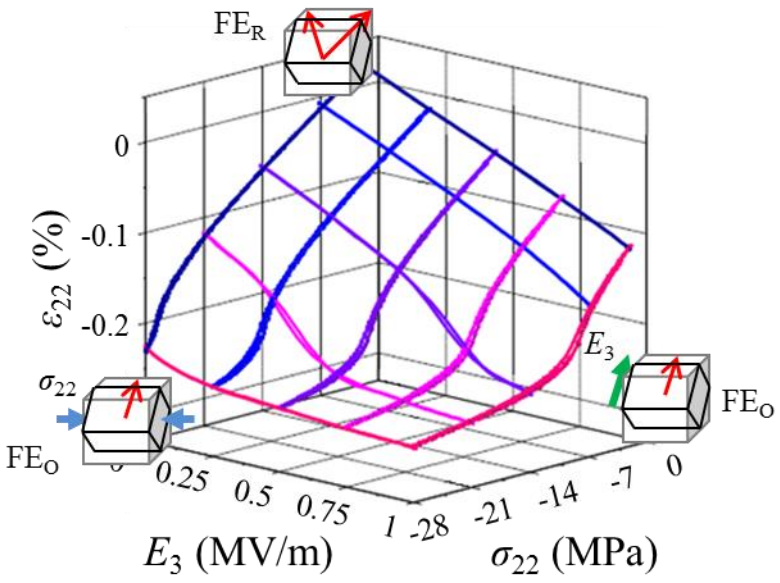

Figure 2-7. E_3-σ_{22}-ε_{22} characterization of $[011]_C$ cut and poled PMN-0.32PT at 40°C [16].

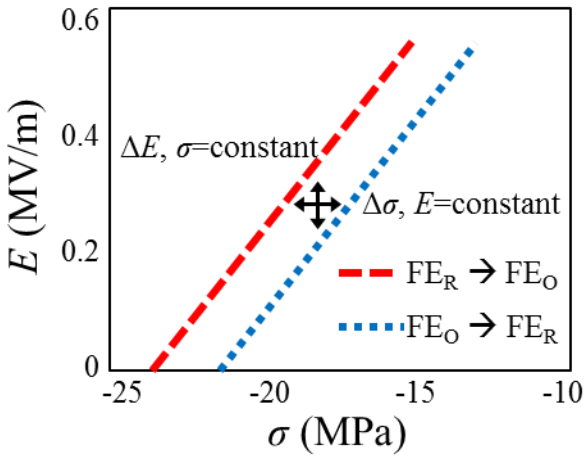

Figure 2-8. Stress and electric field driven phase transformation of PIN-PMN-PT single crystal showing hysteresis [6].

Relaxor ferroelectric behavior is closely related to the domain and phase states, thus making the electromechanical behavior difficult to predict. Hysteresis, fracture, and fatigue decrease their reliability and deteriorate their performance at large fields while the low coercive fields and low Curie temperatures place limits on the mechanical, electrical, and thermal operating range and device fabrication processes. Implementation of relaxor single crystals in applications can be challenging. Relaxor ferroelectric constitutive behavior is rate dependent and sensitive to external loads, while lower coercive fields further limit their operating range. Understanding the nonlinear electromechanical response of relaxor ferroelectrics is important for the implementation of these materials into new applications.

CHAPTER 3

LARGE FIELD DIELECTRIC LOSS IN FERROELECTRIC MATERIALS

A method to determine the large field dielectric loss in ferroelectric materials was used to characterize the effect of field amplitude on the loss of several ferroelectric materials [77]. The dielectric loss was determined by measuring the area within electric displacement vs. electric field hysteresis loops and the measured area was expressed in terms of an effective loss tangent. This approach matches the measured area within the hysteresis loop to an equivalent area ellipse in which the electric displacement lags the electric field by an amount, δ, under sinusoidal loading. This technique was then used to determine the large field dielectric loss in three types of ferroelectric materials under electrical, mechanical and thermal loads: a relaxor ferroelectric single crystal [77], a ferroelectric ceramic [78], and a relaxor ferroelectric composite with a configuration of interdigitated electrodes [79]. The dielectric loss is discussed in terms of field induced domain wall motion within the ferroelectric material.

3.1. Introduction

Ferroelectric materials are used in the design of high performance medical ultrasonic transducers and sonar transducers, vibration control, and active and passive damping, and by industries ranging from aerospace to sporting goods [1-5, 7-9, 80]. During operation these materials undergo electrical, mechanical, and thermal loading. Examples of this are active rotor control on helicopter blades [8] and vibration control and damping on space structures [7]. Changes in temperature, electric field, and stress beyond certain limits lead to variant switching

and field driven phase transitions that dramatically alter the electromechanical properties and contribute to dielectric loss.

Dielectric loss in ferroelectric materials is largely the result of domain wall motion [32, 66]. The mechanical and dielectric energy density that is lost to dissipation in ferroelectric materials under cyclic loading appears as the open area within the strain – stress (ε-σ) and the electric displacement – electric field (D-E) curves. This is a measure of the net external work per unit volume done during the mechanical and electrical loading cycles [77, 81]. Under purely mechanical or purely electrical loading, the open area within a closed mechanical strain – stress (ε-σ) cycle or a closed electric displacement – electric field (D-E) cycle is a direct measure of the amount of external work done in the mechanical or electrical cycles that is converted to heat and dissipated to the surroundings [64, 65]. This energy dissipation is detrimental to sensor and actuator applications but is desirable for vibration suppression and damping applications.

Under small amplitude sinusoidal loading, dielectric and mechanical loss are typically expressed in terms of loss tangents [64]. The dielectric loss tangent is expressed as $\tan \delta$, where δ is the phase lag between an applied electric field, E, and the resulting electric displacement, D [64, 65]. The phase lag model describes the D-E behavior under sinusoidal loading as an ellipse with a slope, and is an excellent approximation at small amplitudes. However, when ferroelectric materials are sinusoidally loaded to large fields, domain wall motion and polarization saturation effects distort the minor hysteresis loops. The area within these loops is also associated with dielectric loss as well as the damping capacity of the material [81, 82].

In this chapter a novel approach to characterizing the large field dielectric loss in ferroelectric materials is presented. The dielectric loss was determined by measuring the area within electric displacement vs. electric field hysteresis loops and the measured area was

expressed in terms of an effective loss tangent. This approach matches the measured area within the hysteresis loop to an equivalent area ellipse in which the electric displacement lags the electric field by an amount, δ, under sinusoidal loading. This technique is used to analyze the dielectric loss in various ferroelectric materials. First, the dielectric behavior of a homogenous relaxor ferroelectric, single crystal lead magnesium niobate – lead titanate, $0.68Pb(Mg_{1/2}Nb_{2/3})O_3$-$0.32PbTiO_3$ (PMN-0.32PT), was experimentally characterized at low frequency under various preload stresses. A discussion of the results in terms of a loss tangent model followed by a discussion of the underlying mechanism contributing to the increased dielectric loss is provided. The results of this study have been published in the *Journal of Applied Physics* [77]. Next, a set of experiments was designed to quantify the effects of compressive bias stress, temperature, and electric field amplitude on large field dielectric loss in ferroelectric ceramic lanthanum doped lead zirconate titanate, $Pb_{0.92}La_{0.08}(Zr_{0.65}Ti_{0.35})_{0.98}O_3$ [83], (PLZT 8/65/35). The results of this study have been published in the peer reviewed journal, *Smart Materials and Structures* [78], and presented at the 2013 SPIE (International Society for Optics and Photonics) Smart Structures/Non-Destructive Evaluation Conference in San Diego, CA USA. This technique was also used to quantify the effect of interdigitated electrodes (IDEs) on ferroelectric materials when compared to a parallel capacitor electrode orientation. A commercial macro fiber composite (MFC) was used in the study. The results are explained using a finite element model to determine the field gradients that develop from the IDE configuration and using this to assess the driving forces for domain wall motion. This work is a result of collaboration with David M. Pisani who developed the simulation model used for finite element analysis. The results of this study have been published in the peer reviewed journal, *Journal of*

Intelligent Material Systems and Structures [79] and presented at the 2013 ASME Conference on Smart Materials Adaptive Structures and Intelligent Systems (SMASIS) in Snowbird, UT USA.

3.2. Large Field Dielectric Loss Model

The studies presented in this chapter are analyzed in terms of a work-energy based model which relates the measured area within the minor hysteresis loops to the energy dissipated per cycle (converted to heat). This relationship is developed from an energy balance.

Equation (3-1) states that the incremental change of internal energy ($\mathrm{d}\phi$) is equal to the incremental amount of mechanical and electrical work done on the specimen plus the increment of thermal energy added to the body,

$$\mathrm{d}\phi = \sigma_{ij}\mathrm{d}\varepsilon_{ij} + E_j\mathrm{d}D_j + \mathrm{d}q\,, \tag{3-1}$$

where dq is the thermal energy added per unit volume by heat flux. Indices vary from 1 to 3. The mechanical work (w^{m}) done along a loading path from state A to state B is given by equation (3-2),

$$\Delta w^{\mathrm{m}} = \int_{\mathrm{A}}^{\mathrm{B}} \sigma_{ij}\mathrm{d}\varepsilon_{ij}\,, \tag{3-2}$$

and the electrical work (w^{e}) along a loading path is expressed by equation (3-3),

$$\Delta w^{\mathrm{e}} = \int_{\mathrm{A}}^{\mathrm{B}} E_j \mathrm{d}D_j \,. \tag{3-3}$$

When the loading is cyclic and the material passes through the same state at each point in the cycle and returns to the initial state at the end of the cycle, the final state is the same as the initial state. Since the integration for this case is performed about a closed cycle, there is no change of energy during the cycle. This results in equation (3-4),

$$\oint \mathrm{d}\, w^{\mathrm{m}} + \oint \mathrm{d}\, w^{\mathrm{e}} + \oint \mathrm{d}q = 0\,, \tag{3-4}$$

where the three terms are the mechanical work done, the electrical work done, and the heat added during one cycle. When measurements are made experimentally, the resulting curves can be integrated numerically using equation (3-4).

In this work, the experiments were performed under isothermal conditions. In this case the third term in equation (3-4) represents the heat removed during the cycle. This is the heat generated by the irreversible mechanical and electrical work, equation (3-5),

$$w^{\mathrm{irr}} = \oint \sigma_{ij}\, \mathrm{d}\varepsilon_{ij} + \oint E_m\, \mathrm{d}D_m \,. \tag{3-5}$$

This irreversible work (w^{irr}) is converted to heat, which was removed through conduction.

Each experiment was run at constant stress. As a result, there was no hysteresis in the stress-strain cycle. Therefore, the irreversible work was solely due to the electrical losses (L_{e}) of the D_3-E_3 cycle, and is equal to the area within the D_3-E_3 hysteresis loop given by equation (3-6),

$$L_e = \oint E_m \mathrm{d}D_m \,. \tag{3-6}$$

This loss was measured for each of the D_3-E_3 curves by numerical integration of the data for each closed cycle. The loss per electric field cycle, as determined using equation (3-6), was calculated through numerical integration of the experimental results.

Loss at small field levels is typically expressed using a phase lag model. In the phase lag model, the applied electric field and resulting electric displacement are described using equations (3-7) and (3-8),

$$E = E_a \cos(\omega t) \tag{3-7}$$

and

$$D = D_a \cos(\omega t - \delta)\,, \tag{3-8}$$

where E_a and D_a are the amplitudes of the electric field and electric displacement, respectively, ω is the angular frequency, and δ is the phase lag. These relations can be expressed in the complex plane[12] and the complex dielectric constant, κ^*, can be used to express the relation between E^* and D^*, equation (3-9),

$$D^* = \kappa^* E^*, \tag{3-9}$$

where $\kappa^* = \kappa' - i\kappa''$. The relation between the real and imaginary coefficients of the complex dielectric constant gives the tangent of the phase delay, δ, equation (3-10),

$$\frac{\kappa''}{\kappa'} = \tan\delta\,, \tag{3-10}$$

where the real and imaginary coefficients are $\kappa' = \frac{D_a}{E_a}\cos\delta$ and $\kappa'' = \frac{D_a}{E_a}\sin\delta$, respectively. Substitution of equations (3-7) and (3-8) into equation (3-6) leads to equation (3-11),

$$w^e = \oint E\mathrm{d}D = \int_0^{2\pi/\omega} E\left(\frac{\mathrm{d}D}{\mathrm{d}t}\right)\mathrm{d}t = \pi E_a D_a \sin\delta\,. \tag{3-11}$$

As shown in Figure 3-1, the phase lag model expresses the dielectric loss as the area of an ellipse. The phase lag based expression for loss given by equation (3-11) is used to describe the experimentally determined loss, L_e, using equation (3-12), an expression that gives the area of an ellipse equivalent to the measured area within the hysteresis loop,

$$\tan\delta = \tan\left[\sin^{-1}\left(\frac{L_e}{\pi E_a D_a}\right)\right]. \tag{3-12}$$

The effective loss tangent was calculated using equation (3-12).

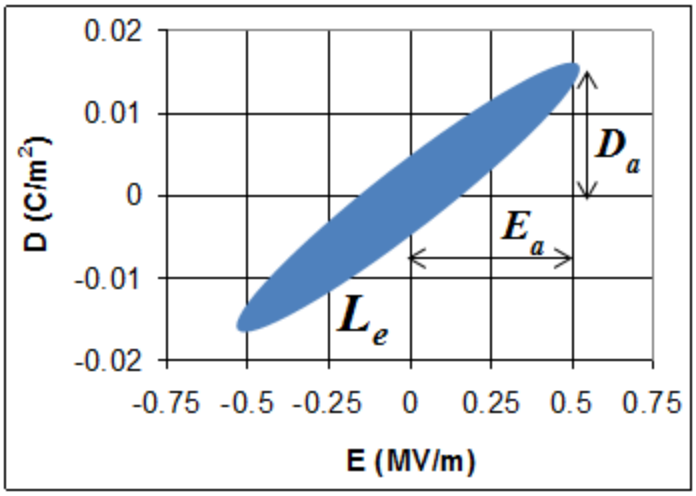

Figure 3-1. The phase lag model expresses the measured dielectric loss in terms of the equivalent area within the ellipse shown.

3.3. Effect of Field Driven Phase Transformation on the Loss Tangent of PMN-0.32PT Single Crystals

Relaxor ferroelectric single crystals are used extensively in high performance medical ultrasonic transducers and sonar transducers [1-5]. During operation these single crystal materials undergo electrical, mechanical, and thermal loading. Changes in temperature, electric field, and stress beyond certain limits lead to variant switching and field driven phase transitions that dramatically alter the electromechanical properties and contribute to dielectric loss in which electrical work on the material is converted to heat. McLaughlin et al. [20] measured the stress - temperature - electric field phase diagram for ferroelectric rhombohedral (FE_R) $[001]_C$ cut and poled lead magnesium niobate – lead titanate, $0.68Pb(Mg_{1/2}Nb_{2/3})O_3$-$0.32PbTiO_3$ (PMN-0.32PT) single crystals showing that as the $[001]_C$ compressive stress is increased, the material is driven into the ferroelectric orthorhombic (FE_O) phase, and as an $[001]_C$ electric field is applied to the

FE_O phase, the material is driven to the FE_R phase. This forward and reverse phase transformation is hysteretic.

Early studies conducted by Härdtl [66] found that losses in ferroelectric ceramics are dominated by domain wall motion. Domain engineered single crystals of $[001]_C$ cut and poled PMN-*x*PT are designed to minimize the driving forces for domain wall motion and reduce or eliminate these losses [12, 63, 67]. When these crystals are driven at low field levels very little hysteresis is observed in the strain-stress (ε-σ) and electric displacement-electric field (*D*-*E*) curves and very small values are measured for the dielectric loss. However, as either the electric field amplitude or bias stress is increased, these crystals can enter a phase transformation region. In this region, non-linearity occurs in the ε-σ and *D*-*E* loops and hysteresis between the loading and unloading curves increases. This behavior is highly dependent on composition of the crystal, with some compositions displaying a sudden jump in polarization when a critical field is reached, and others displaying a gradual phase transition spread over a range of field levels [70]. In piezoelectric devices, heat generation is induced by both mechanical and electrical loss. In transducer applications, heat generation caused by mechanical loss (ε-σ hysteresis) is larger at mechanical resonance whereas dielectric loss (*D*-*E* hysteresis) is larger away from resonance [64, 65]. Larger dielectric loss reduces the quality factor in resonant devices.

In this study the dielectric behavior of PMN-0.32PT relaxor single crystals was experimentally characterized at low frequency under various preload stresses. A discussion of the results in terms of a loss tangent model followed by a discussion of the underlying mechanism contributing to the increased dielectric loss is presented.

3.3.1. *Experimental Approach*

Four stack actuators were produced. $[001]_C$ oriented PMN-0.32PT relaxor single crystals were cut into 7x7x0.5 mm^3 plates and electroded on opposite faces with sputtered gold. Copper shims 0.08 mm thick with pattered holes to reduce their in-plane stiffness were fabricated to make the electrical connections to each layer. Fourteen of these plates separated by the copper shims were epoxy bonded together to form a stack actuator as shown in Figure 3-2. Leads were attached to protruding tabs of alternate shims so that an electric field, E_3, could be applied to each plate and induce axial strain, ε_{33}.

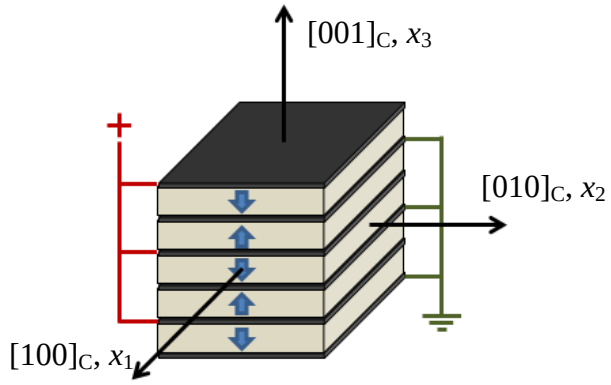

Figure 3-2. Structure of the stack actuators that were characterized. Alternate electrodes were connected to make the plates act in parallel to each other, allowing electric field E_3 to induce axial strain ε_{33}. The arrows indicate the volume average polarization of each plate.

The single crystal stack actuators were placed within the loading system shown schematically in Figure 3-3. A modified Sawyer Tower circuit was used measure the electric displacement. In this circuit, the external capacitor is several orders of magnitude larger than the capacitance of the specimen. This results in a negligible voltage drop across the external

capacitor relative to the applied voltage. The voltage across this capacitor is read using an electrometer to avoid draining any of the charge during the measurement. The electric displacement was calculated by multiplying the output voltage by the capacitance of the external capacitor and dividing by the cross sectional area over which the electric field was applied (the number of plates times the plate electrode area), while electric field was calculated by dividing the applied voltage by the plate thickness. A screw driven load frame was used to apply constant stress during electrical cycling. This was accomplished by placing a compliant layer in series with the ferroelectric specimen. The electric field E_3 was cycled at a frequency of 1 Hz from 0 to 0.5 MV/m; 0 to 0.75 MV/m; 0 to 1.0 MV/m; and 0 to 1.5 MV/m. Zero preload stress was applied for the first set of electric field cycles while for each subsequent set of electric field cycles the bias stress was increased in increments of -7 MPa up to a maximum compressive preload stress of -28 MPa. The stress bias was only increased to -21 MPa for the test in which the electric field was cycled to an amplitude of 1.5 MV/m.

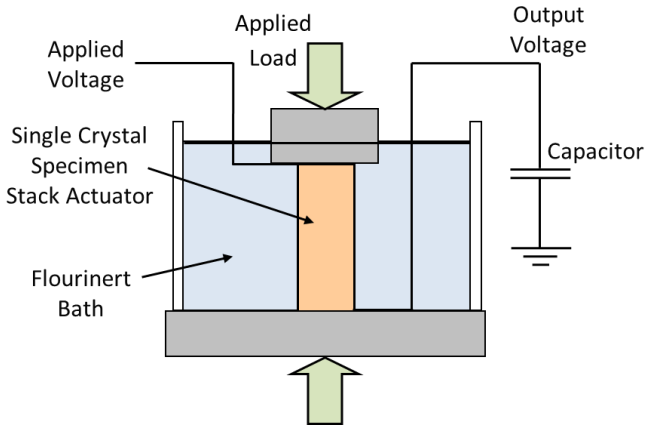

Figure 3-3. Experimental arrangement that enables the application of stress and electric field while monitoring strain and electric displacement.

3.3.2.*Experimental Results*

Figure 3-4 shows the experimental results. At zero stress the D_3-E_3 cycle was closest to linear and displayed the least hysteresis. As the stress preload was increased, the hysteresis increased and the D_3-E_3 response became gradually more non-linear. The minor hysteresis loop is smallest at low preload stresses. As stress preload is increased, hysteresis in the D_3-E_3 cycle increases. These effects became more pronounced as the electric field amplitude was increased.

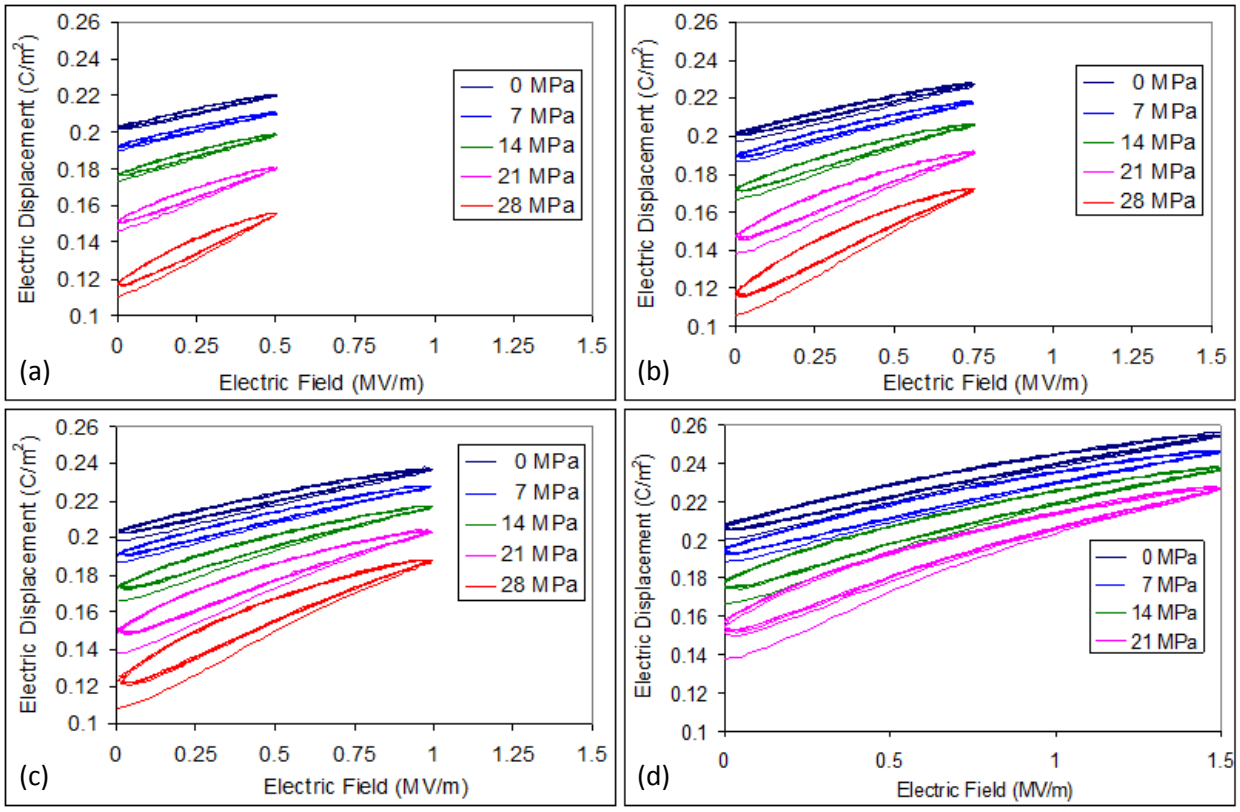

Figure 3-4. Electric displacement versus electric field for each preload stress showing the effect of electric field amplitude and stress amplitude on the minor hysteresis loop. E_3 was cycled from (a) 0 to 0.5 MV/m, (b) 0 to 0.75 MV/m, (c) 0 to 1.0 MV/m, and (d) 0 to 1.5 MV/m. For all plots, the remnant polarization decreases as preload stress is increased.

3.3.3.*Analysis and Discussion*

The loss per electric field cycle (L_e), as determined using equation (3-6), was calculated for each electric field amplitude and stress preload by numerical integration. As shown in Figure 3-5, the loss per cycle was found to increase with increasing stress preload as well as with increasing electric field amplitude.

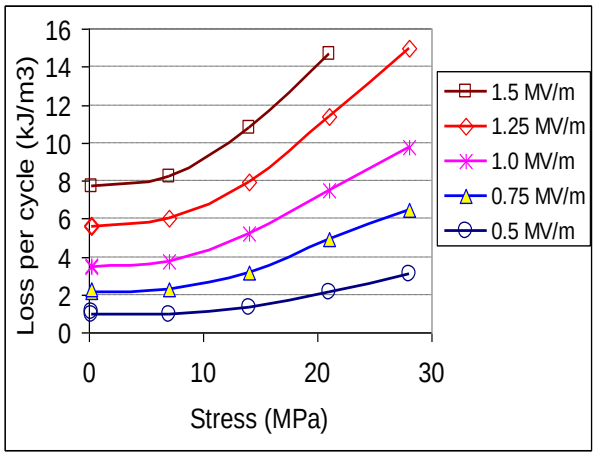

Figure 3-5. Loss per cycle (L_e) is plotted as a function of stress preload for each electric field amplitude. The error in the calculated loss was less than 2%.

The effective loss tangent of the single crystal stack actuator was calculated using equation (3-12) and is plotted for each load combination in Figure 3-6. The effective loss tangent displays a small dependence on the applied electric field amplitude and larger dependence on the applied stress preload. The effective loss tangent was found to have a value of 0.125 for stress preloads smaller than -7 MPa. However, as the preloads were increased to values greater than -7 MPa, tan δ was found to increase up to a value of 0.19 at a preload of -28 MPa.

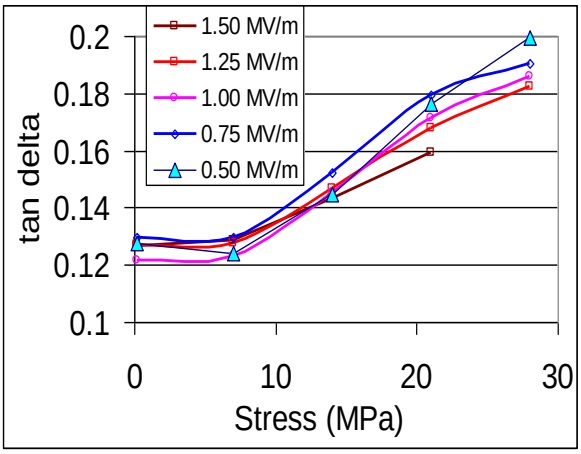

Figure 3-6. Effective loss tangent as a function of stress preload for each electric field cycle amplitude. The error in the computed dielectric loss was based on the resolution of the instrumentation and found to be less than 2% for all values.

The behavior observed in Figure 3-6 is explained in terms of field driven phase transformations. PMN-*x*PT single crystals exhibit the paraelectric cubic (PE_C), ferroelectric tetragonal (FE_T), ferroelectric rhombohedral (FE_R), ferroelectric monoclinic (FE_M) and ferroelectric orthorhombic (FE_O) phases depending on temperature and composition. In compositions near morphotropic phase boundaries, electric field or stress of sufficient amplitude and orientation can drive phase transformations. For example, a transition between the FE_R and FE_T phases occurs with the application of a large enough bias electric field along $[001]_C$. Bias fields of smaller amplitude along this direction decrease the FE_R-FE_T phase transition temperature [84]. Figure 3-7 shows how applied stress and electric field in the $[001]_C$ direction drive field induced phase transformations in PMN-0.32PT single crystals. Polarized PMN-0.32PT under small applied stress and electric field at room temperature is in the FE_R phase with

easy polarization in the $<111>_C$ directions. When polarized by a $[001]_C$ electric field above the coercive field, only four of the eight $<111>_C$ variants are populated as shown in Figure 3-7(a). Remnant polarization, P_r, is the volume average of the polarization of the four variants that are populated after poling. As compressive stress is increased, the crystal transforms to the FE_O phase with four of the $<110>_C$ variants populated as shown in Figure 3-7(b). This results in a large contraction in the $[001]_C$ direction. The compressive stress does positive work during this contraction and thus provides a positive driving force for this transformation. If electric field is subsequently increased in the $[001]_C$ direction while holding the stress constant, the crystal is driven back toward the original FE_R phase, through a monoclinic phase, as shown in Figure 3-7(c). As the electric field is increased, the crystal transforms back to the four variant FE_R phase shown in Figure 3-7(a).

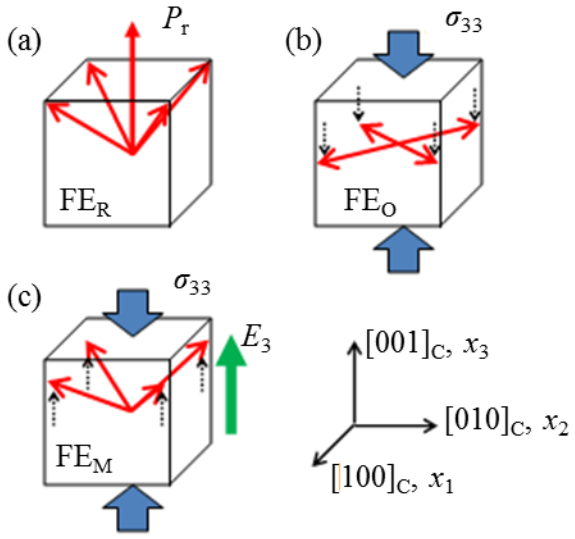

Figure 3-7. Domain states and field driven phase transformations in PMN-0.32PT single crystals under $[001]_C$ stress and electric field and stress loading. (a) Crystal is in the FE_R phase with $[001]_C$ remnant polarization. (b) Increasing compressive stress induces a FE_R-FE_O phase

transformation while a subsequent increase in electric field (c) drives a reverse FE_O-FE_R transformation back to ferroelectric rhombohedral. Stress and electric field work against each other when driving phase transformations.

As the preload stress was increased from 0 to -28 MPa, the D_3-E_3 loop displayed increasing hysteresis between the loading and unloading curves. This is attributed to the preload stress driving the single crystal partially into the orthorhombic phase. When comparing Figures 3-4 (a) through (d), it is observed that preload stress increases this hysteresis. This phase transition is hysteretic and results in losses. Partial transformation of the crystal with a stress bias results in the electric field moving phase boundaries during electrical loading, increasing the effective dielectric loss.

3.3.4. *Concluding Remarks*

Dielectric loss was measured under large field electrical loading at different bias stress levels. The dielectric loss was determined by measurement of the area within D_3-E_3 hysteresis loops produced under unipolar electrical loading. The dielectric loss was expressed in terms of an effective loss tangent, tan δ, through use of a phase lag model by matching the area within the measured minor hysteresis loop to that of an ellipse of equivalent area. The result was that the loss data collapsed nearly to a single curve, independent of electric field amplitude but dependent on bias stress in the range of electric field and stress considered. The observations were explained in terms of stress preload driving the crystal toward the FE_O state and the electric field driving the crystal back toward the FE_R state. The observed trends in dielectric loss are expected

to change under a broader range of stress and electric field magnitudes. The range of stress and electric field explored in this study were close to or within the phase transformation regime.

Loss tangent values for the PMN-0.32PT single crystal stack actuator were found to range from 0.12 to 0.20, depending on the bias stress. These values are considerably larger than the small field loss tangent for $[001]_C$ cut and poled PMN-0.32PT single crystals [84]. The combined bias stress and large electric field loading activate a dissipation mechanism that is not present or has a very small effect at small field. No attempt was made to measure the temperature or frequency dependence of the large field dielectric loss in this work.

3.4. Large Field Dielectric Loss in Relaxor Ferroelectric PLZT

The addition of donor dopants such as lanthanum to lead zirconate titanate ($Pb_{1-x}La_x(Zr_{1-y}Ti_y)_{1-x/4}O_3$ [83], or PLZT) creates "soft" ferroelectric behavior and yields larger dielectric and piezoelectric coefficients and larger dielectric loss factors [85]. The composition $Pb_{0.92}La_{0.08}(Zr_{0.65}Ti_{0.35})_{0.98}O_3$ (PLZT 8/65/35) was chosen for this study because of the proximity to the morphotropic phase boundary (MPB) as shown in Figure 3-8 [86]. This produces very large changes in material behavior over a small range of temperature, stress, and electric field. PLZT 8/65/35 is in the rhombohedral ferroelectric (FE_R) phase with soft ferroelectric behavior at room temperature. The room temperature phase diagram indicates that PLZT can be ferroelectric tetragonal (FE_T), paraelectric cubic (PE_C), antiferroelectric (AFE), or mixed phase. With an increase of temperature, PLZT 8/65/35 transitions to slim-loop ferroelectric behavior [86]. Above the Burns temperature, 350°C, PLZT 8/65/35 is in the paraelectric cubic phase and does not exhibit localized polarization [87]. The Burns temperature is associated with a deviation in

the index of refraction of the material [87]. Upon cooling, polar nanoregions, or polar nanodomains, appear and the domains grow in size as the temperature is decreased [87, 88]. The polar nanoregions develop about fluctuating local dipoles and give rise to kinetically disordered localized polarizations [89]. Through further cooling a temperature is reached where the matrix begins to deform due to the local polarizations [90, 91]. Below the Curie temperature, 110°C [86], the material transitions to ferroelectric rhombohedral.

The small field behavior of PLZT 8/65/35 has been well studied and characterized. Akbas et al. [92], showed that the relative dielectric permittivity increases with temperature to a maximum at the Curie peak, shown in Figure 3-9(a). The relative dielectric permittivity was determined to increase with decreasing frequency. Mohiddon and Yadav [93] characterized the small field tan δ through use of an LCR meter frequency sweep over a range of temperatures. Similar to the relative dielectric permittivity results, tan δ was found to increase with temperature to a maximum at the Curie peak, shown in Figure 3-9(b).

In this work a set of experiments was designed to quantify the effects of compressive bias stress, temperature, and electric field amplitude on large field dielectric loss in PLZT 8/65/35. The measured dielectric loss is expressed in terms of both the large field effective loss factor, tan δ, and the area within the electric displacement – electric field minor hysteresis loop, the loss energy. The results are compared to the published low field results of Mohiddon and Yadav.

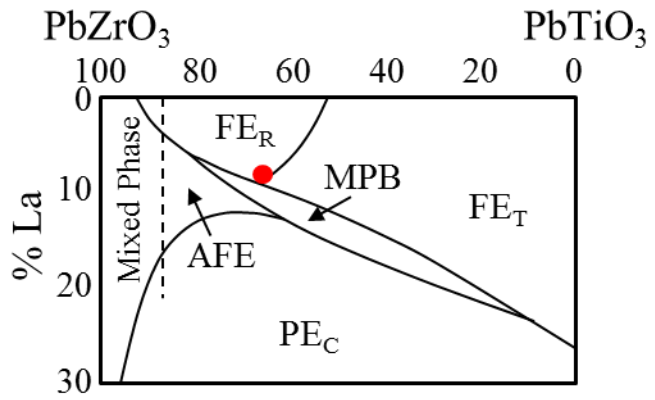

Figure 3-8. Room temperature phase boundary diagram for PLZT [86]. The composition of PLZT 8/65/35 is marked by the large dot.

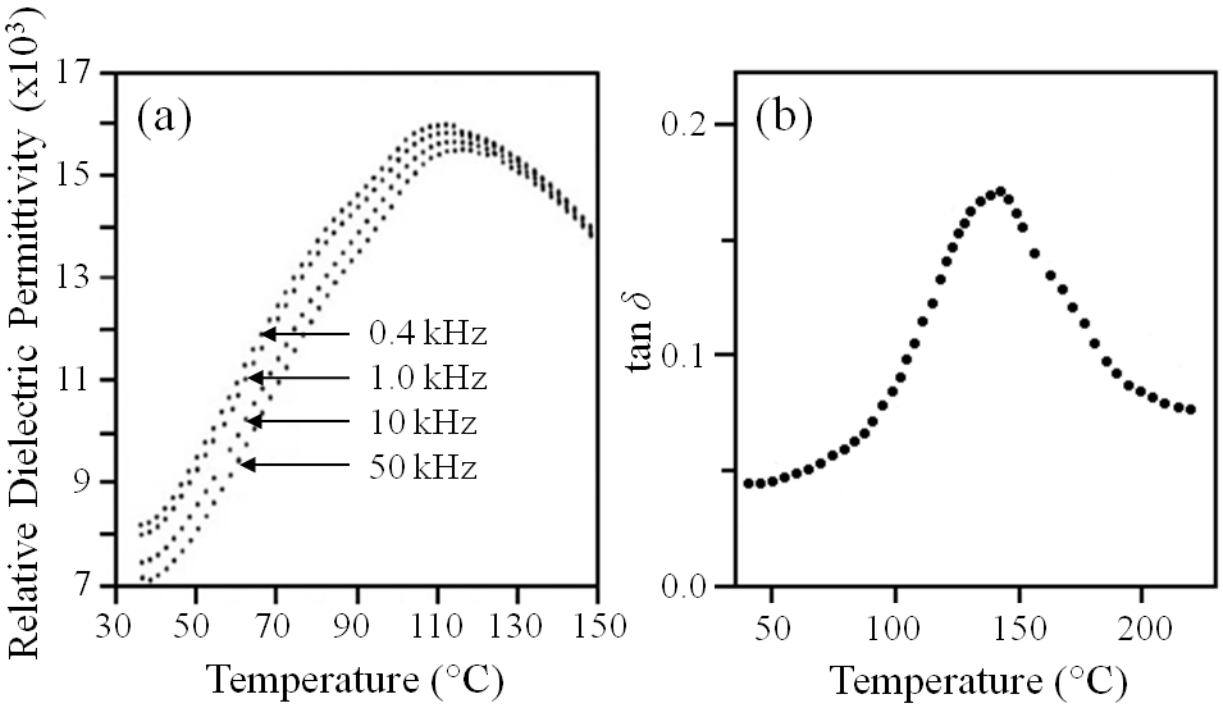

Figure 3-9. (a) Relative dielectric permittivity vs. temperature and frequency [92] and (b) tan δ vs. temperature [93] for PLZT 8/65/35. The small variations in the Curie peak are expected and are due to specimen differences.

3.4.1. *Experimental Approach*

The PLZT ceramic specimens were fabricated using a mixed oxide method from high purity (>99.9%) PbO, La_2O_3, ZrO_2, and TiO_2 powders. Each precursor was weighed with respect to the nominal composition of PLZT 8/65/35 and then made into a suspension with deionized water using Darvan dispersant and a NH_4OH solution. The mixed powder was ball milled using ZrO_2 grinding media for 16 hours before being dried. Lumps were crushed using a mortar and pestle. The resulting crushed powder was again placed into a suspension and re-milled for 16 hours before being deposited into an alumina crucible and calcined at 900°C for 6 hours. A 3% by weight acrylic binder was added to the calcined powder with acetone as the solvent. The resulting powder was passed through a 100-mesh sieve to filter the aggregated powder before it was uniaxially pressed into pellets at -20 MPa. The pellets were placed in an alumina crucible and subjected to a binder burnout cycle followed by a sintering process at 1300°C for 2 hours. The sintering process was carried out in a Pb-rich atmosphere that provided excess PbO and ZrO_2 to prevent the loss of the volatile Pb. This resulted in disc shaped ceramic specimens that were cut and ground to produce specimens each with 11 mm diameter and 2.6 mm thickness. XRD was used to confirm the presence of the ferroelectric rhombohedral phase. The discs were initially poled with the volume average remanent polarization along the cylindrical axis. Three discs were stacked with the initial volume average remanent polarization in alternating directions. 0.05 mm thick copper mesh shims were used to make electrical connections.

The specimens were placed in a mechanical / electrical loading system shown schematically in Figure 3-10. Bias stress was applied by use of a screw-driven load frame and

constant stress was maintained during electric field cycling. A modified Sawyer Tower circuit was used to measure the electric displacement. In this circuit the external capacitor was several orders of magnitude larger than the capacitance of the specimen. When voltage was applied to the specimen in series with the external capacitor, the capacitance difference resulted in a small voltage drop across the external capacitor. An electrometer was used to read the voltage across this capacitor to avoid any draining of charge during the measurement. Electric displacement was calculated by dividing the charge by the electrode area. Electric field was calculated by dividing the applied voltage by the specimen thickness. The specimens were submerged in a flourinert bath to provide electrical insulation. A heating strip and thermocouple were placed within the flourinert bath to control the temperature. Figure 4-3 shows a schematic of the experimental loading arrangement.

Each specimen was subjected to bipolar electric field cycles from -1.5 MV/m to 1.5 MV/m and unipolar electric field cycles to amplitudes of 0.5, 1, 1.5, 2, and 2.5 MV/m. Electric field was cycled at a frequency of 1 Hz. Electric field was cycled eight times at each unipolar amplitude. The results were calculated from the average of cycles three through eight to avoid any effects from the initial loading cycles. The first cycle is not a closed loop and exhibits excess hysteresis. Hysteresis arises from a large irreversible change in polarization due to the logarithmic aging effect in ferroelectric ceramics [94, 95]. Zero axial bias stress was applied for the first set of electric field cycles. For each subsequent set of electric field cycles, bias stress was increased in increments of -5 MPa up to a maximum stress of -20 MPa in compression. The series of tests were run at 25°C, 50°C, 75°C, and 100°C. The loading was such that the compressive stress, σ_{33}, caused D_3 to decrease while the positive electric field, E_3, caused D_3 to increase.

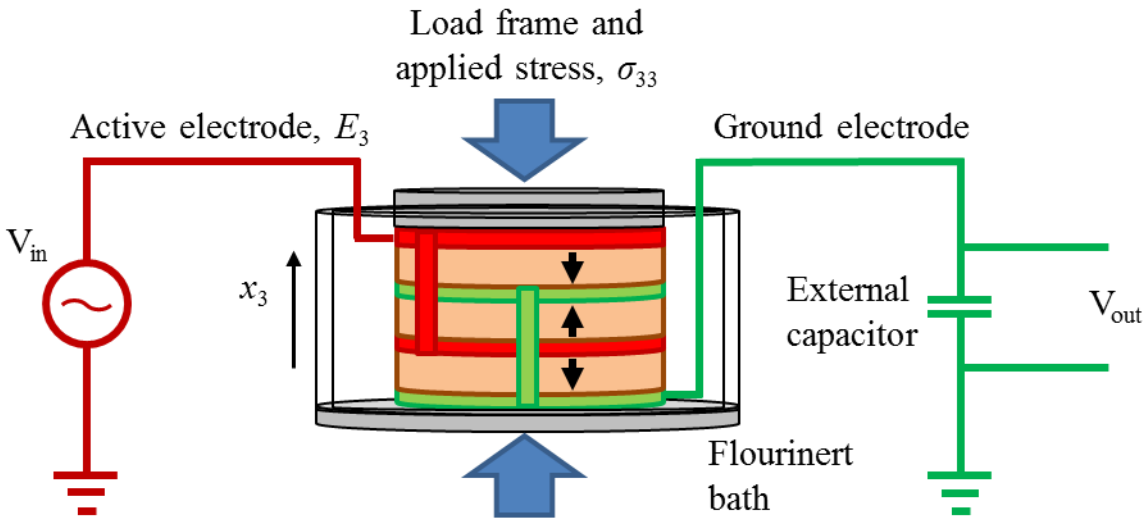

Figure 3-10. Experimental arrangement of the mechanical / electrical loading system. Specimens were characterized in the stack arrangement shown. The arrows indicate the initial volume average remnant polarization direction of each disk.

3.4.2. *Experimental Results*

The zero stress bipolar electric field – electric displacement results are shown in Figure 3-11 and are consistent with previously published data [86]. As temperature is increased the PLZT transitions from ferroelectric rhombohedral *D-E* behavior at 25°C to slim-loop ferroelectric *D-E* behavior at 100°C. Increasing temperature causes a decrease in the remanent polarization and the coercive field. Figures 3-11 (a) through (d) show the effect of stress preload on the *D-E* behavior at 25°C through 100°C, respectively. Increasing the bias stress causes a decrease in remanant polarization while reducing the slope of the *D-E* curve. For all temperatures, at 0 MPa bias stress there is a sharper transition as the *D-E* curve passes through *D*=0. Remanent polarization

decreases as stress is increased at 25°C while at 100°C there is little decrease in remanent polarization with stress. The coercive field is nearly independent of stress preload at each temperature.

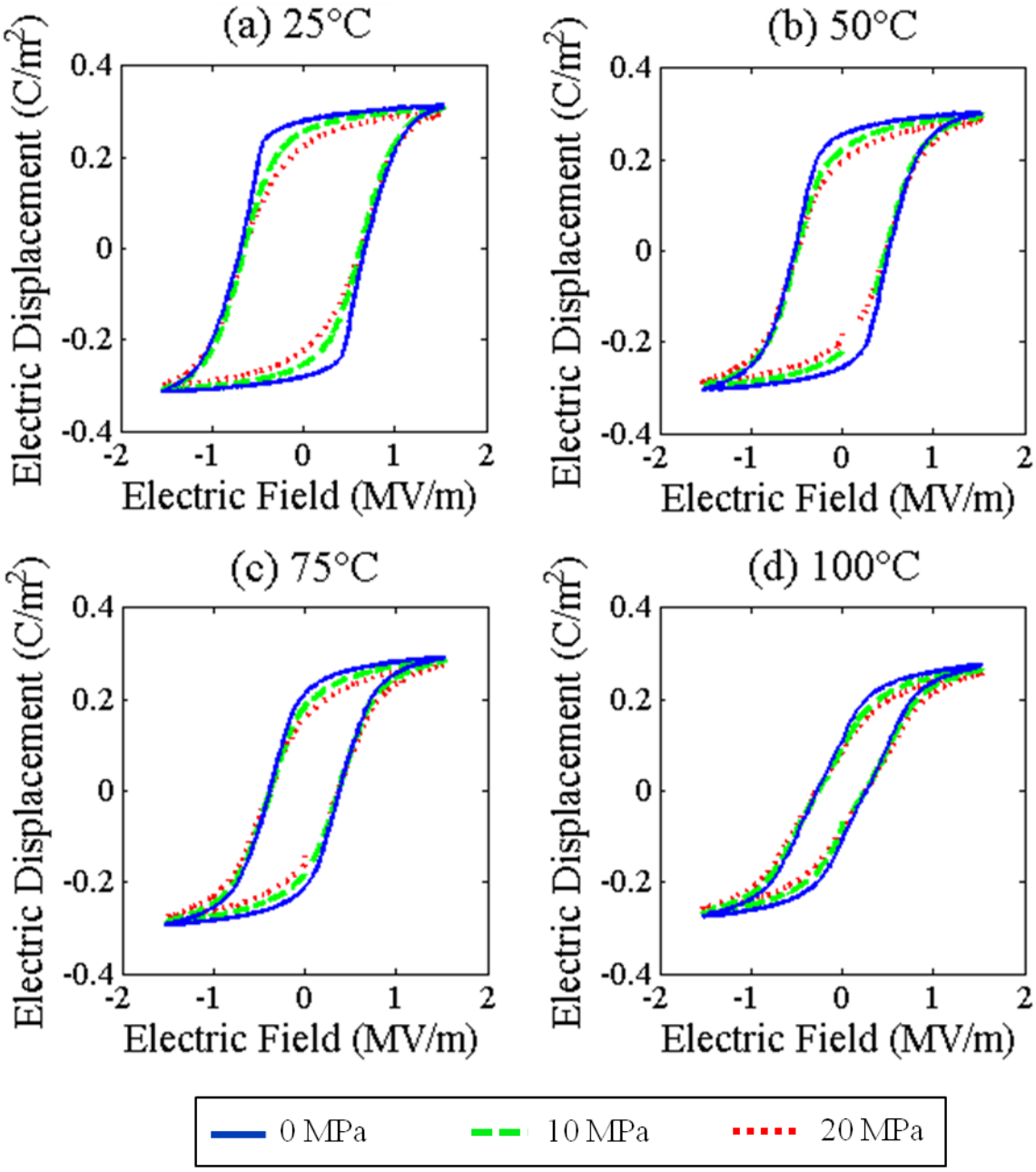

Figure 3-11. Bipolar *D-E* loops for compressive preload stresses of 0 MPa, -10 MPa, and -20 MPa at (a) 25°C, (b) 50°C, (c) 75°C, and (d) 100°C.

Figure 3-12 shows the results of unipolar loading at electric field amplitudes of 0.5 MV/m, 1.5 MV/m, and 2.5 MV/m with compressive preload stresses of 0 MPa, -10 MPa, and -20

MPa, at 25°C and 100°C. Additional curves were omitted to avoid obscuring the plots. At 25°C for small and large amplitude loading (Figures 3-12 (a) and (b)), the zero stress *D-E* cycle displayed the least hysteresis. As the stress preload was increased to -20 MPa the hysteresis increased and the *D-E* response became less linear. At the higher electric field amplitude shown in Figure 3-12(b) the compressive stress increased the non-linear behavior. The electric displacement reached similar saturation levels regardless of the stress induced decrease in remanent polarization. Increasing the temperature to 100°C (Figures 3-12 (c) and (d)) had a negligible impact on remanant polarization but caused the *D-E* response of the PLZT to be nonlinear at all stresses. Although saturation of the *D-E* loop occurred at large electric fields for all stresses at 100°C as shown in Figure 3-12(d), saturation did not occur at the same electric displacement levels.

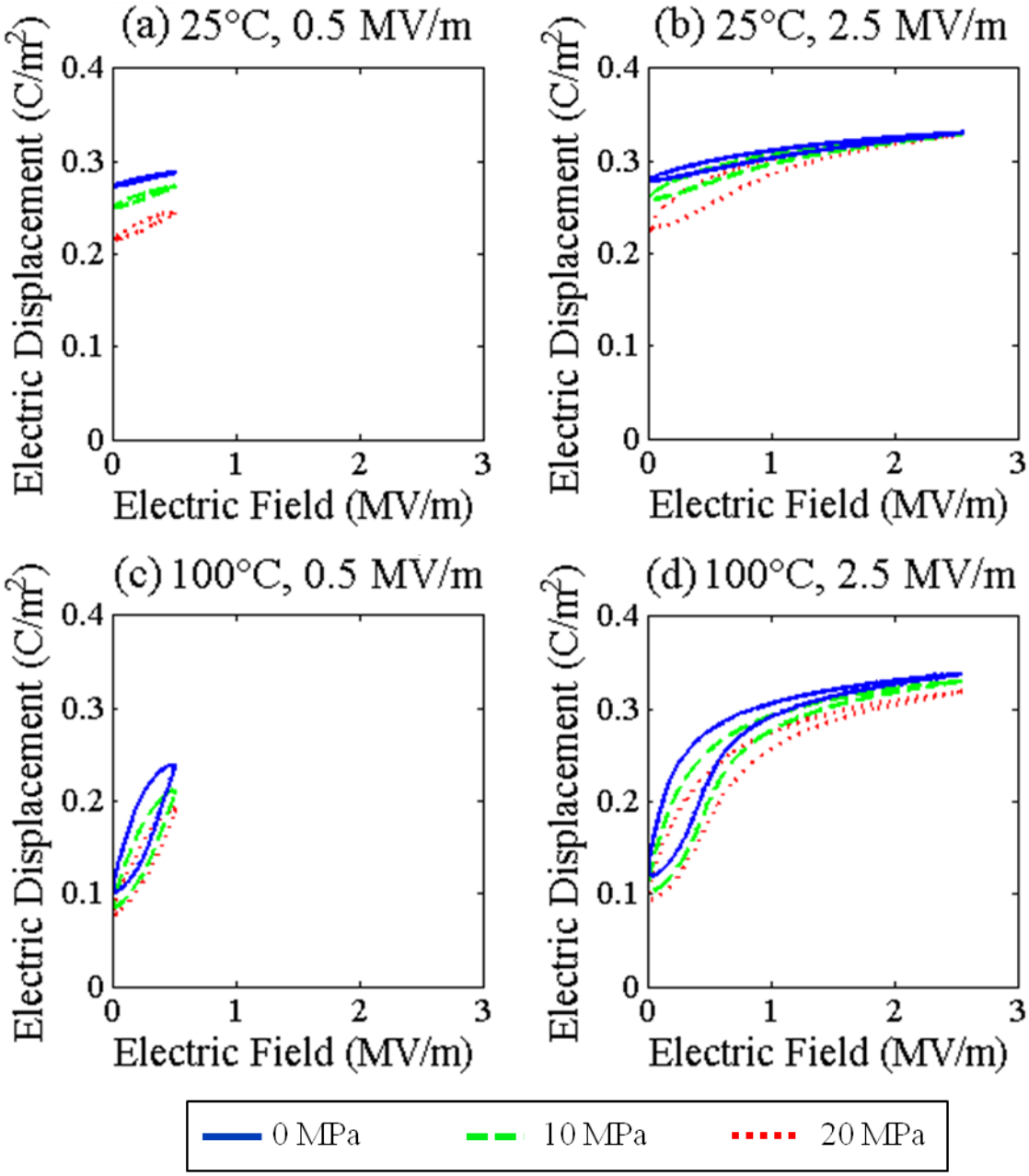

Figure 3-12. Unipolar *D*-*E* hysteresis loops for compressive preload stresses of 0 MPa, -10 MPa, and -20 MPa at (a) 25°C and 0.5 MV/m, (b) 25°C and 2.5 MV/m, (c) 100°C and 0.5 MV/m, and (d) 100°C and 2.5 MV/m.

3.4.3. *Analysis and Discussion*

The results displayed in Figure 3-12 show that as stress and temperature are increased, the hysteresis loops change slope and open up. This is apparent at an electric field amplitude of 0.5 MV/m and the effect is more pronounced at 100°C. At an electric field level of 2.5 MV/m, the effects of polarization saturation become apparent as a flattening of the tops of the hysteresis loops. The data presented in Figure 3-12(a) can be approximated fairly well as an ellipse with a slope. This fits the phase lag model well. As the temperature, bias stress, and electric field amplitude are increased, an ellipse no longer fits the data well. This section discusses measurement of an effective dielectric loss that approximates the area within the minor hysteresis loop as an ellipse of equivalent area.

Figure 3-14 shows the effective dielectric loss tangent calculated for each loading condition using equation (3-12). At all temperatures tan δ is larger at lower electric field amplitudes. Tan δ decreases as electric field amplitude increases. The pronounced difference in the slope and values of tan δ with stress between Figures 3-12 (a) through (d) is related to the transition to slim loop behavior at increased temperature. Tan δ increases with stress preload at room temperature and decreases with stress preload at 100°C. There is a transition in behavior with stress at approximately 50°C, where stress preload has a negligible effect on tan δ and all values lie on the same path.

The large field effective tan δ is much larger than the previously published small field data [93], shown in Figure 3-9(b). At small field, tan δ has been found to increase from approximately 0.05 at 25°C up to 0.1 at 100°C. While this increase with temperature was observed at large field, the effective tan δ at zero preload stress and the relatively low field of 0.5 MV/m increased from approximately 0.20 at 25°C to 0.5 at 100°C. The increase in tan δ between

small and large field was expected as dielectric losses are largely affected by domain wall motion [32]. At larger fields more energy is available to move the domain walls, increasing loss. The results for effective tan δ shown in Figure 3-14 need further discussion. As electric field is increased to 2.5 MV/m, tan δ decreases and converges to approximately 0.12 for all temperatures and preload stresses. Saturation of the *D-E* loops at large electric fields does not cause a proportional increase in the hysteresis loop area L_e. As saturation is approached, the additional contributions to loss become smaller as the electric field amplitude increases. This decreases the $L_e/(E_a D_a)$ ratio resulting in a decrease in effective tan δ with increasing electric field amplitude. The convergence of tan δ at 2.5 MV/m behaves approximately as $1/E_a$ due to saturation of the *D-E* loops.

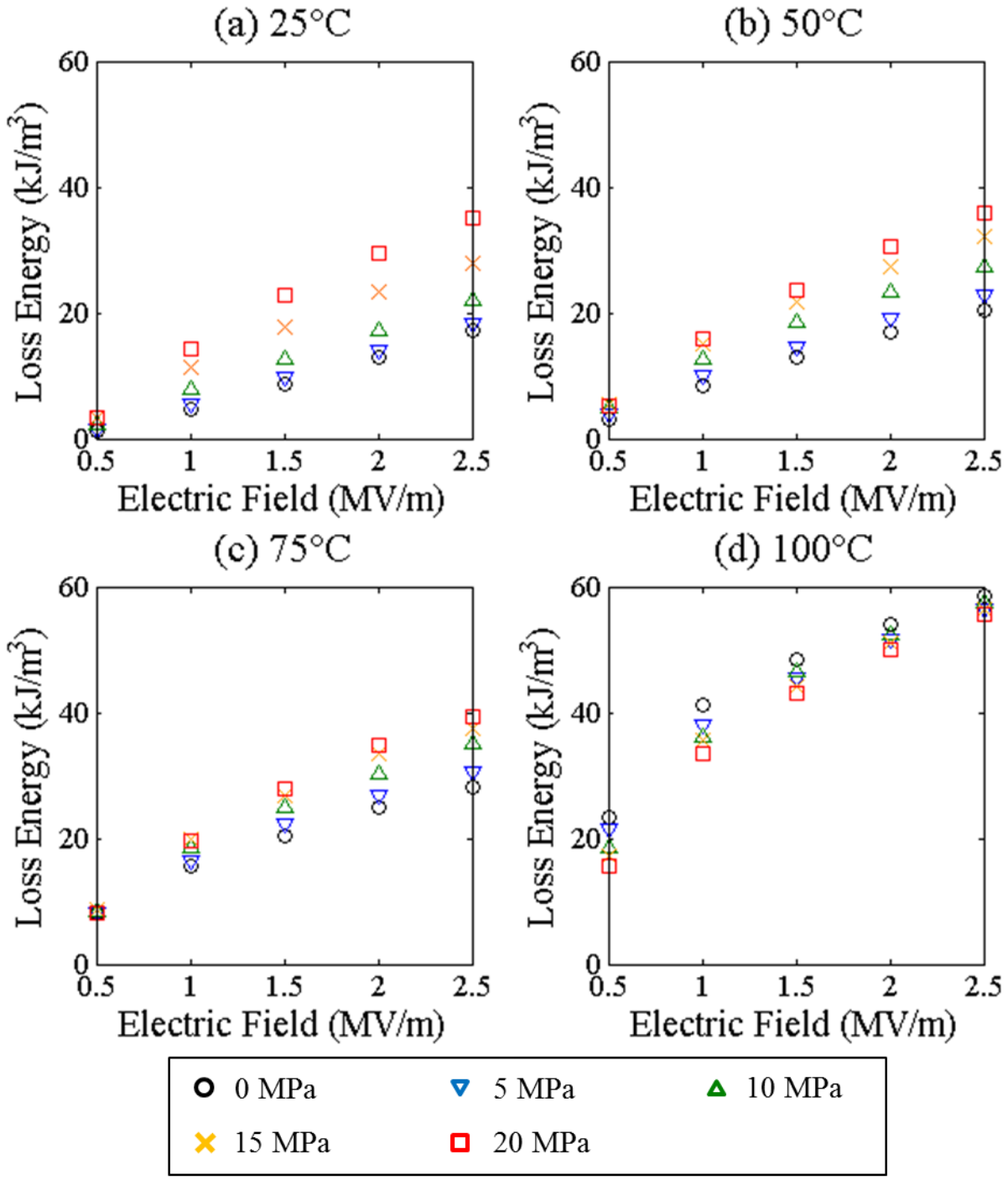

Figure 3-13. Loss energy (L_e) behavior with respect to electric field amplitude for all compressive stress preloads at (a) 25°C, (b) 50°C, (c) 75°C, and (d) 100°C.

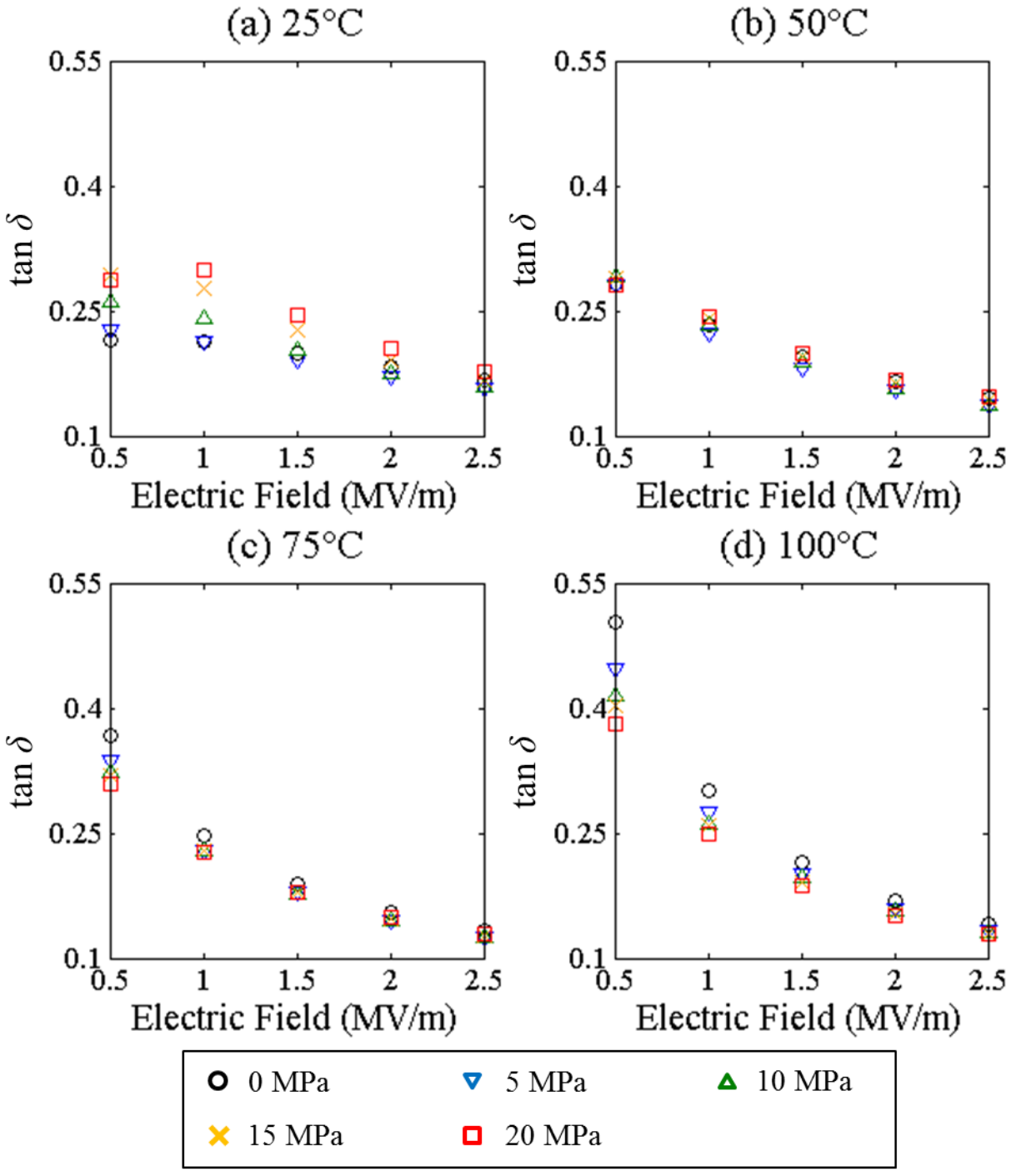

Figure 3-14. Tan δ behavior with respect to electric field amplitude for all compressive stress preloads at (a) 25°C, (b) 50°C, (c) 75°C, and (d) 100°C.

3.4.4. *Concluding Remarks*

The large field effective dielectric loss of PLZT 8/65/35 was experimentally measured using a technique that matches the area within the unipolar electric displacement – electric field hysteresis loop to an equivalent area ellipse-shaped hysteresis loop. The loss behavior of the PLZT was explained through an analysis of the experimental *D-E* loop behavior. At all temperatures, an increase in electric field caused a decrease in tan δ. This was consistent with the material nearing polarization saturation levels with the application of large electric fields. However, the effect of stress on tan δ was found to reverse as temperature was increased. Stress increased tan δ at 25°C and decreased tan δ at 100°C. Tan δ converged to approximately 0.12 at 2.5 MV/m for all loading conditions. This behavior coincided with changes in the *D-E* hysteresis and saturation of the polarization. The decrease in tan δ at larger electric fields did not correspond to a decrease in energy loss per cycle, L_e. The decrease in tan δ quantifies the decrease of the ratio between energy loss (L_e) and total available energy ($4E_aD_a$).

Increasing temperature causes a transition of domain structure in PLZT. At higher temperatures, domains in PLZT begin transitioning into a polar nanodomain structure. Increasing stress at 100°C may promote this transition, acting to pin the domain walls. This process may explain the observed decrease in tan δ when stress preload is increased at 100°C.

3.5. Stress and Electric Field Gradient Contributions to Dielectric Loss with Interdigitated Electrodes

Interdigitated electrodes (IDEs) on piezoelectric materials produce in-plane anisotropy in the piezoelectric and optical properties, with an effective d_{33} between the electrodes and d_{31}

parallel to the electrodes. They are used in MEMs devices [96], energy harvesting [97, 98], piezoelectric vibration sensing [99] and damping [80], as well as in piezoelectric strain rosettes to locate wave sources or damage [100-103]. IDEs were used by Cutchen in 1980 for fast acting flash goggles [104]. In 1993 Hagood et al. investigated IDEs on piezoceramic wafers as a way to improve transverse actuation [105]. In 1995 Bent et al. coupled IDEs to piezoelectric fiber composites [106]. These composites were composed of round extruded piezoelectric fibers embedded in a soft epoxy matrix sandwiched between two layers of IDEs. Although the fiber design in the polymer matrix made the composite more flexible and robust than previous wafer designs, the performance was limited due to insufficient contact between the electrodes and the fibers. Similarly, electric potential in the fibers was limited due to the higher permittivity of the fiber than the matrix [107]. In 2000 Wilkie et al. developed macro fiber composites (MFCs) [108]. In some ways similar to the design of Bent et al., MFCs were constructed using IDEs on rectangular fibers instead of cylindrical fibers. A d_{33}-mode MFC with IDEs is shown schematically in Figure 3-15. It consists of alternating positive and negative electrodes that pole and actuate the piezoelectric material along its length. This IDE pattern utilizes the d_{33} piezoelectric coefficient, providing greater electromechanical coupling and strain output than actuators that utilize the d_{31} piezoelectric coefficient.

The d_{33}-mode IDE pattern results in field gradients within the fibers. Although the field is uniform along the fibers away from the electrodes, a field gradient exists in the vicinity of the electrodes. This field gradient creates a polarization gradient during the poling process [109, 110]. Compatibility requirements result in the development of stress in the material beneath the electrodes. The stress state changes when a voltage is applied to the electrodes. This drives

ferroelastic domain wall motion. Domain wall motion contributes to material losses and damping [32, 66].

This work examines dielectric loss and damping as a function of electric field amplitude in a MFC with IDEs. A range of electric field amplitudes was applied and the resulting dielectric losses were determined from the area within the unipolar *D-E* hysteresis loops. The contribution of the IDE configuration to the dielectric loss was experimentally determined through a comparison to the dielectric loss in a uniformly polarized plate of the same ferroelectric material. The polarization gradient and residual stress within the MFC were examined with a micromechanical computational model.

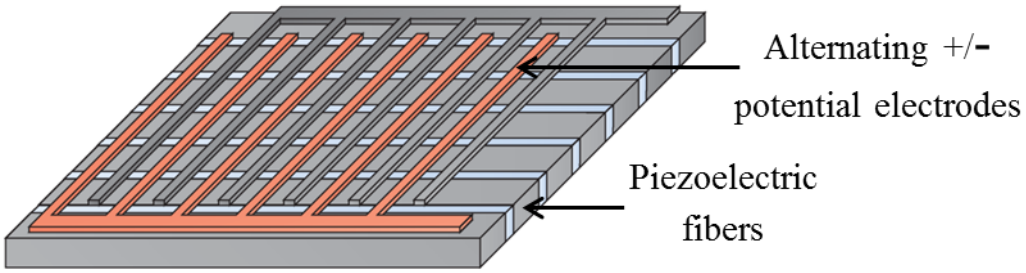

Figure 3-15. Schematic of d_{33}-mode IDEs on a MFC.

3.5.1. *Experimental Approach*

Experiments were performed on commercial M-8528-P1 MFCs from Smart Material Inc. The MFC consisted of longitudinal polycrystalline PZT-5A fibers. The fibers ran between two transverse sets of 170 alternating positive and ground electrodes capable of producing d_{33}-mode strain along the fibers. The overall dimensions for the PZT used in the MFC were 85x28x0.15 mm^3. This volume accounted for the overall volume spanned by the PZT fibers, including the

epoxy filled spaces between adjacent fibers. The electrode spacing was 0.5 mm and the electrode width was 0.125 mm. A polycrystalline PZT-5A plate with dimensions of 80x29x0.27 mm^3 was used as a reference configuration. The opposite large planar faces were electroded and leads were attached.

The small field experiments were run using an Agilent 4284A Precision LCR meter was used to measure tan δ and capacitance of the MFC and plate specimens at a voltage of 1 V. Frequency was swept from 20 Hz to 1 MHz.

For the large field experiments, each specimen was subjected to eight successive unipolar sinusoidal electric field cycles at a frequency of 1 Hz. This was repeated at amplitudes from 0.5 MV/m to 4.5 MV/m in increments of 1 MV/m. A 10 kV voltage amplifier was used to apply the input voltage (V_{in}). Electric field was calculated as the applied voltage divided by the electrode spacing. A modified Sawyer Tower circuit was used to measure the electric displacement. In this circuit the external capacitor was several orders of magnitude larger than the capacitance of the specimen. When voltage was applied to the specimen in series with the external capacitor the capacitance difference resulted in a small voltage drop across the external capacitor. An electrometer was used to read the voltage across this capacitor (V_{out}) to avoid any draining of charge during the measurement. Electric displacement was calculated by dividing the charge by the electrode area. This was done by multiplying the output voltage (read by the electrometer) by the capacitance of the external capacitor and dividing by the electrode area. The experimental arrangement of the MFC is shown in Figure 3-16. A similar experimental arrangement was used for the plate. Three MFCs were tested for verification of the results. The *D-E* hysteresis and resulting tan δ and damping factor had similar behavior for the three MFC specimens.

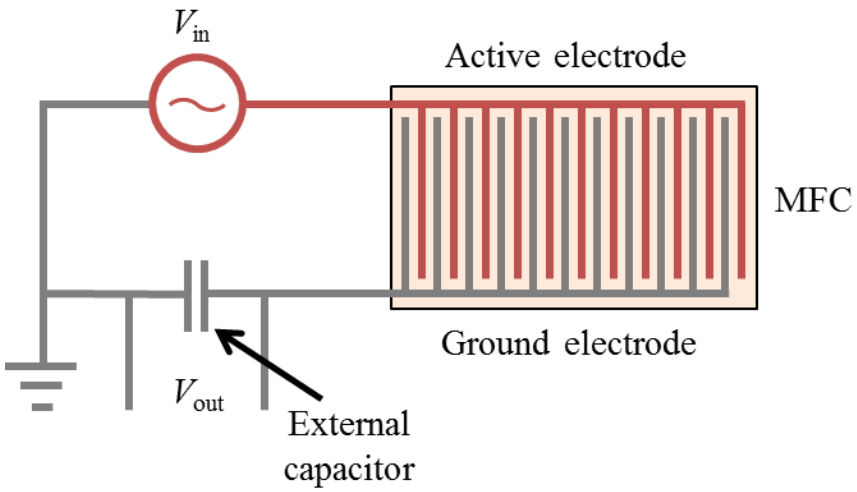

Figure 3-16. Experimental arrangement used to apply electric field and measure electric displacement of the MFCs. A similar arrangement was used for the plate.

3.5.2. *Experimental Results*

The results from the small field LCR tests for tan δ and capacitance are shown in Figures 3-17 and 3-18, respectively. Figures 3-17 and 3-18 show the results up to 220 kHz. A large spike in tan δ and discontinuity in capacitance occurred between 10 and 20 kHz for both the MFC and the plate. Tan δ for the MFC, as shown in Figure 3-17(a), was found to be between 0.02 and 0.04 for frequencies below 10 kHz. A large spike in tan δ to above 0.32 occurred at 20 kHz. Similarly, as shown in Figure 3-17(b), tan δ for the plate was found to be 0.01 below 2 kHz and continuously increased above 2 kHz. A large spike in tan δ to about 0.85 occurred at 20 kHz. The 20 kHz frequency corresponds to the fundamental mode planar resonance of the MFC. Capacitance of the MFC, shown in Figure 3-18(a), was found to decrease linearly from 5.75 nF to 5.25 nF with frequency for frequencies below 10 kHz. The MFC underwent an abrupt discontinuity in capacitance between 10 and 20 kHz, followed by a decrease to about 4.5 nF

above 20 kHz. Capacitance of the plate, shown in Figure 3-18(b), was around 160 nF below 10 Hz. Discontinuity was found between 10 and 20 kHz followed by sporadic behavior at frequencies above 20 kHz. Similar to the MFC, the planar mode resonance of the 80 mm plate was just under 20 kHz.

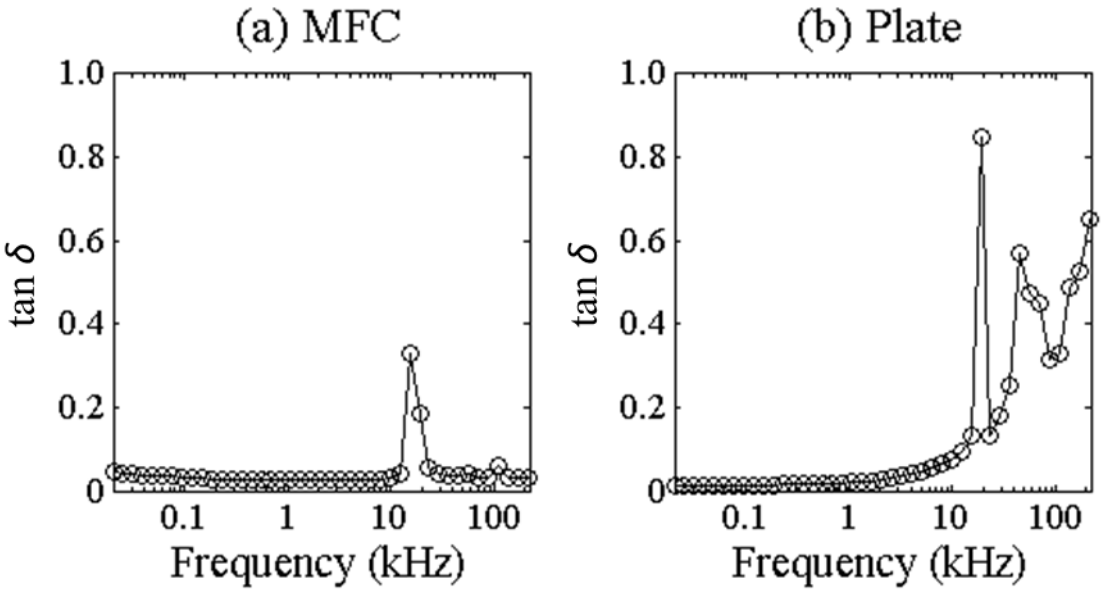

Figure 3-17. Tan δ for the (a) MFC and (b) plate, measured with an LCR meter frequency sweep from 20 Hz to 1 MHz at 1 V. Results from 20 Hz to 220 kHz are shown.

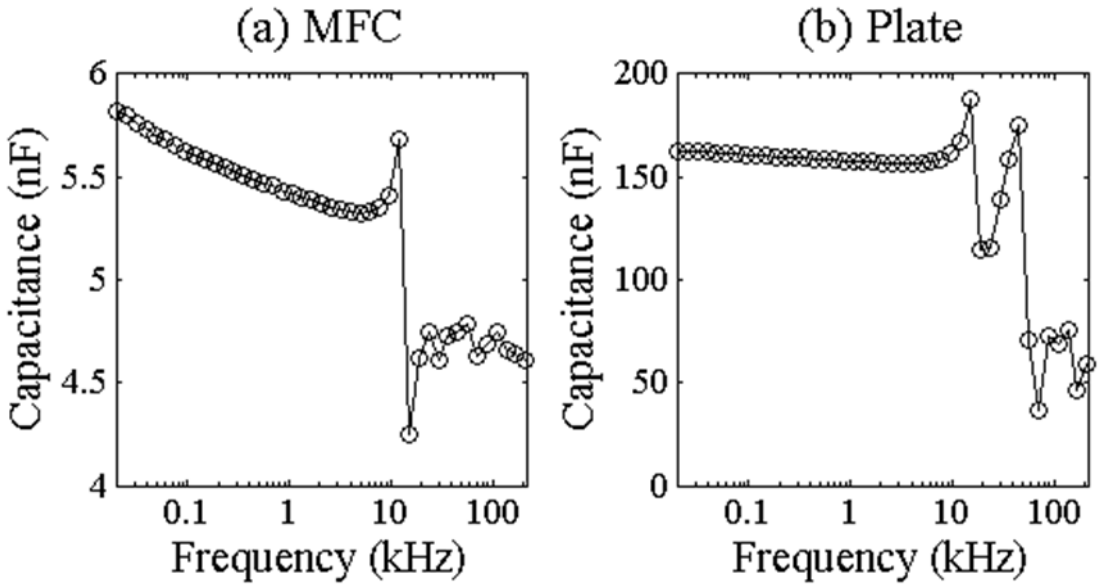

Figure 3-18. Capacitance for the (a) MFC and (b) plate, measured with an LCR meter frequency sweep from 20 Hz to 1 MHz at 1 V. Results from 20 Hz to 220 kHz are shown. Note the difference in the capacitance scale between (a) and (b).

For the large field tests, unipolar electric field cycles were run at amplitudes from 0.5 MV/m to 4.5 MV/m in increments of 1 MV/m while monitoring the electric displacement. The unipolar *D-E* hysteresis loops for the MFC and plate are shown in Figures 3-19 (a) and (b), respectively. The first cycle is not a closed loop and exhibits excess hysteresis. Over time there is some depolarization due to the logarithmic aging effect in ferroelectric materials [95]. The first large field cycle re-poles the material. This effect is not as pronounced in the plate. The MFC experienced significantly greater hysteresis in the *D-E* loops than the plate for all electric field amplitudes. Both the MFC and the plate experienced the least hysteresis at an electric field amplitude of 0.5 MV/m. Similar relative polarization changes occurred in the closed cycles for the MFC and the plate. Saturation in the electric displacement response began to occur at higher

electric field levels. All three MFCs experienced similar hysteresis and relative polarization changes.

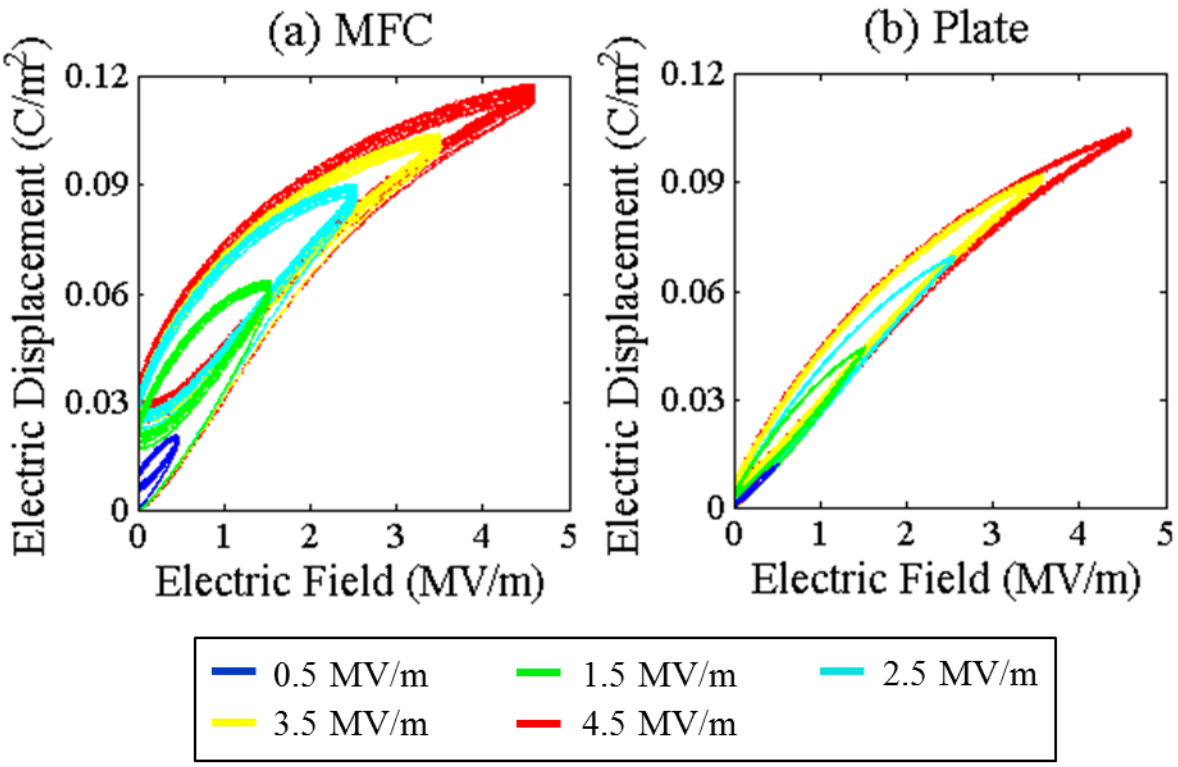

Figure 3-19. Unipolar D-E hysteresis loops for the (a) MFC and (b) plate at electric field amplitudes from 0.5 MV/m to 4.5 MV/m, in increments of 1 MV/m. All eight loading cycles are shown.

3.5.3. *Analysis and Discussion*

The finite element model was developed by David M. Pisani to assist in the analysis of the difference in experimental results between the MFC and plate configurations of PZT-5A. The finite element model was based on an extension to 3D elements of the micromechanical finite element approach developed by Chen and Lynch [111]. From the finite element model, a

material model was developed to use the approach of Hwang et al. [112], modified by Chen and Lynch [111]. The model was used to assess interactions between polarization gradients and residual stress in the ferroelectric material beneath the IDEs. The model was used to determine if the larger *D-E* hysteresis and greater loss in the MFC was a result of ferroelastic polarization reorientation during each electric field cycle.

Figure 3-20 shows the resulting tan δ values for each electric field loading amplitude. Each value is the average determined from cycles three through eight. As seen in Figure 3-20, the dielectric loss is a function of amplitude and the dielectric loss in the MFC with IDEs is substantially larger than the dielectric loss in the plate. Differences in tan δ among the three MFCs were negligible.

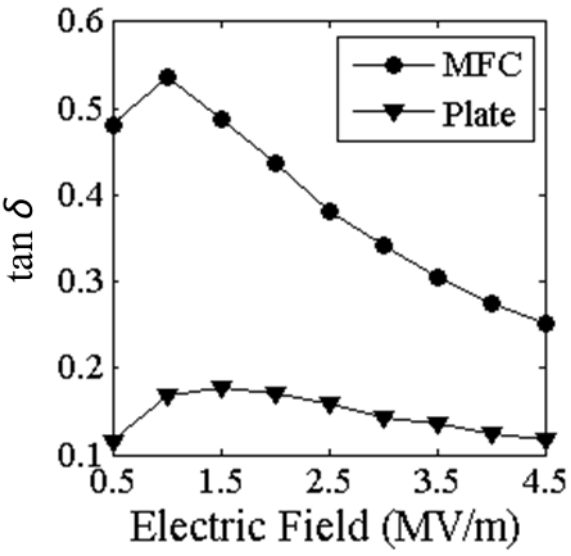

Figure 3-20. Large field effective tan δ versus electric field amplitude. Both the MFC and plate follow a similar profile with a large initial increase in tan δ, followed by a near linear decrease as

electric field amplitude is increased. Tan δ was found to be roughly three times larger for the MFC than the plate.

Ji et al. [82] expressed the damping capacity of a material under cyclic loading as the ratio of the loss energy to the maximum available energy. This method equates the maximum available energy to the rectangular area formed by the start of the cycle and the point corresponding to the maximum loading amplitude. This relation is expressed in equation (3-13) for electrical work,

$$f_D^{\mathrm{e}} = \frac{\int_0^{D_{\max}} E_{\mathrm{loading}}\,\mathrm{d}D - \int_0^{D_{\max}} E_{\mathrm{unloading}}\,\mathrm{d}D}{U_{\max}} = \frac{\oint E\mathrm{d}D}{E_{\max}D_{\max}} = \frac{L_{\mathrm{e}}}{E_{\max}D_{\max}}, \tag{3-13}$$

and shown in Figure 3-21. f_D^{e} is the dielectric damping factor and L_{e} is the loss energy per cycle. $U_{\max}$ is the maximum possible energy and is equal to the product of the electric field amplitude, $E_{\max}$, and the maximum change in electric displacement, $D_{\max}$.

Figure 3-22 shows the damping factor for each electric field loading amplitude as calculated with equation (3-13). Each value is the average determined from cycles three through eight. The behavior of the damping factor correlates with the behavior of tan δ. The damping factor is a function of amplitude. The MFC with IDEs has a substantially greater damping capacity than the plate. Differences in the damping factor among the three MFCs were negligible.

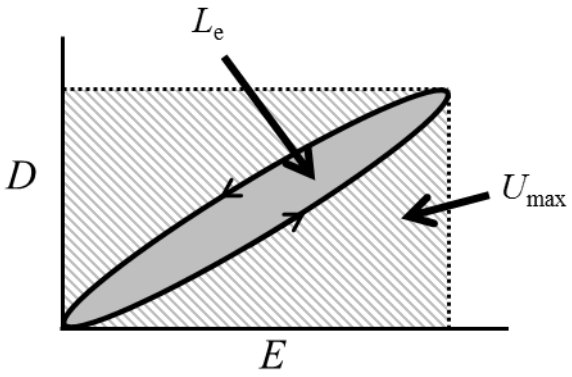

Figure 3-21. Dielectric damping coefficient was calculated as the ratio between the energy lost in a loading cycle (L_e) to the maximum available energy (U_{max}).

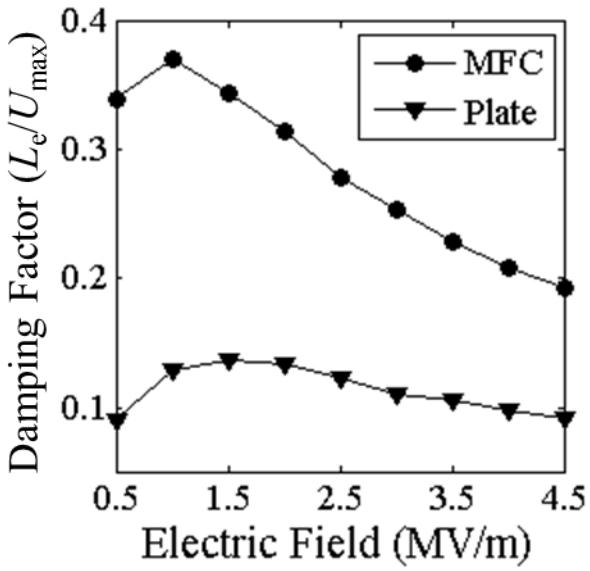

Figure 3-22. Large field damping factor versus electric field amplitude. The damping capacity of the MFC was found to roughly three times larger for the than the damping capacity of the plate.

Interactions between the ferroelectric portions of the fibers directly underneath the electrodes and the bare ferroelectric portions of the fiber was investigated. The MFC was

initially poled along the fiber length whereas the plate was initially poled through the thickness. The MFC experienced more hysteresis in the electric displacement response than the plate; therefore there were greater dielectric losses and increased damping for the MFC. The finite element model was used to determine the multiaxial polarization reorientation behavior of the ferroelectric fiber in the MFC. The results indicate that polarization gradients drive ferroelastic domain wall motion within the fibers of the MFC during loading.

Figures 3-23, 3-24, and 3-25 show the finite element results. The electrode is on the top left surface. In Figure 3-23 the longitudinal (horizontal) electric field away from the electrodes results in uniform polarization along the fiber axis. In this region the fiber extends along its length and shrinks in the vertical direction. The horizontal uniform field between alternating electrodes causes lateral extension along the fiber axis corresponding to d_{33} and transverse contraction corresponding to d_{31}. The longitudinal component of electric field is zero beneath the electrodes and the material in this region does not change shape. This shape mismatch results in stress. Larger stress occurs where the transition in polarization is more abrupt. The field concentration at the edges of the electrodes corresponds to a very large strain mismatch while diffuse regions have a lower strain mismatch. The strain mismatch-induced stress distribution in the material after poling is shown in Figure 3-24. The largest stress occurs where the field gradient is greatest (beneath the electrode). The uniform field region away from the electrode experiences no polarization induced stress. The stress state changes under application of electric field. When a large field is applied, the strain mismatch between the region under the electrode and the region away from the electrode increases. This results in ferroelastic assisted polarization changes in the regions near the electrode. When the field is removed, the shape mismatch is reduced. This induces reverse ferroelastic polarization changes.

The ferroelastic induced polarization changes can be seen in Figure 3-25. Figure 3-25 shows the difference in remanant polarization states between the fully applied voltage and when the voltage is removed. When the voltage is applied the ferroelastic switching causes more remanant polarization to be pulled upwards towards the electrode. Upon release, the remanant polarization states return as reflected in Figure 3-25. The result is the experimentally observed increased hysteresis in the MFC over that of the uniformly poled plate of the same material.

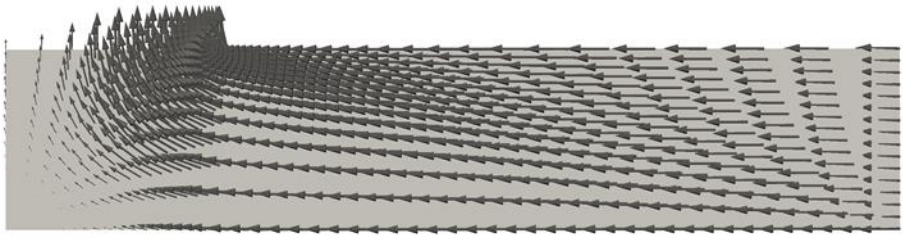

Figure 3-23. Polarization state at maximum applied voltage. The arrows are scaled with the polarization magnitude, where the maximum polarization was 0.31 C/m^2. The electrode edge is on the top left face.

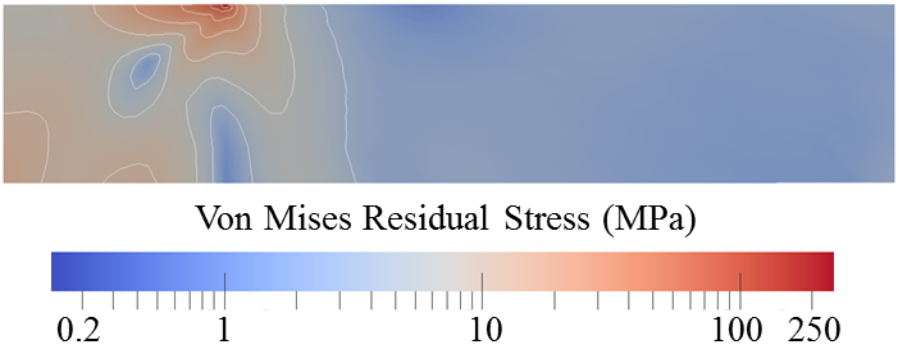

Figure 3-24. Model of the residual stress state when the voltage is removed from the fiber after poling. The electrode is located on the top left face.

Figure 3-25. Difference in the remanant polarization when the voltage is removed from the fiber and the remanant polarization of maximum applied voltage. The arrows are scaled with remanant polarization magnitude such that the maximum scale is 0.03 C/m^2. The electrode edge is on the top left face.

3.5.4. *Concluding Remarks*

This study experimentally characterized the dielectric loss and damping behavior of ferroelectrics with interdigitated electrodes. Differences in dielectric loss and damping between a commercial d_{33}-mode MFC and an electroded plate, both PZT-5A, were analyzed. The large field effective dielectric loss was experimentally measured using a technique that matches the area within the unipolar electric displacement – electric field hysteresis loop to an equivalent area ellipse-shaped hysteresis loop. Tan δ for the MFC was found to be approximately three times larger than that of the plate. Similarly, the MFC had two to three times the damping capacity of the plate. PZT-5A has approximately a 2 to 1 ratio of d_{33} to d_{31}. This means that the d_{33} MFC design has increased energy absorption capabilities without a compromise in actuation capabilities. The MFC geometry was analyzed using a non-linear and hysteretic finite element model that captures the full poling behavior of ferroelectric ceramics. Polarization and strain mismatches between the region around the electrodes and the region away from the electrodes were found to drive domain wall motion during electrical loading of the MFC.

CHAPTER 4

COMPOSITIONAL DEPENDENCE OF FIELD INDUCED PHASE TRANSFORMATIONS IN $[011]_C$ PIN-PMN-PT RELAXOR FERROELECTRIC SINGLE CRYSTALS WITH d_{32} PIEZOELECTRIC MODE

Relaxor ferroelectric single crystals are used in sonar, medical ultrasound, accelerometers, and energy harvesting applications due to their large electro-mechanical coupling. In this work, the compositional dependence of the electro-mechanical properties of $[011]_C$ cut relaxor ferroelectric lead indium niobate – lead magnesium niobate – lead titanate single crystals, $x\text{Pb}(\text{In}_{1/2}\text{Nb}_{1/2})\text{O}_3\text{-}(1\text{-}x\text{-}y)\text{Pb}(\text{Mg}_{1/3}\text{Nb}_{2/3})\text{O}_3\text{-}y\text{PbTiO}_3$ (PIN-PMN-PT) was determined. The effect of increasing the concentration of lead indium niobate (xPIN) and increasing the concentration of lead titanate (yPT) on compositions near the morphotropic phase boundary was explored. Specimens were subjected to combined electrical, mechanical, and thermal loading. The electric field induced changes of polarization and strain were measured at a series of preload stresses and the stress induced polarization and strain changes were measured at a series of bias electric fields. This was repeated at several temperatures. Evidence of a phase transformation from ferroelectric rhombohedral to ferroelectric orthorhombic was observed in the form of jumps in strain and electric displacement at critical field levels. The linear piezoelectric constant, dielectric permittivity, elastic compliance, thermal expansion, pyroelectric coefficient, and rate of change of the material properties with temperature were determined including a scalar measure of electro-mechanical work indicating the start of the field induced phase transformation.

The results of this study have been accepted for publication in *Acta Materialia* [113] and submitted for publication in *Applied Physics Letters* [114].

4.1. Introduction

Relaxor ferroelectric single crystals are used in advanced sonar transducers and medical ultrasound transducers [1-5] due to their enhanced electro-mechanical properties [12, 60, 61]. The anisotropic in-plane strain of the $[011]_C$ cut has been used as a test bed to study the behavior of magnetoelectric heterostructures under biaxial strain loading [10, 11]. Single crystals display reduced hysteresis when loaded in certain crystallographic directions [12]. They also display a diffuse phase transition about the Curie temperature [62].

The properties of relaxor ferroelectric single crystals depend on composition and crystal cut. The binary crystal of lead magnesium niobate – lead titanate, $(1\text{-}x)Pb(Mg_{1/3}Nb_{2/3})O_3\text{-}xPbTiO_3$ (PMN-PT), with compositions near the morphotropic phase boundary (MPB) on the rhombohedral side (x = 0.28 to 0.33) has a coercive field E_C ~ 0.25 MV/m, a rhombohedral to tetragonal transformation temperature $T_{R/T}$ < 100°C, and a Curie temperature T_C ~ 150°C [33-36]. The elastic, piezoelectric, and dielectric coefficients have strong temperature dependence and the range of operating electric field is reduced to zero as $T_{R/T}$ is approached. This has led to the development of ternary crystals with a higher $T_{R/T}$. The addition of lead indium niobate (PIN) to PMN-PT has increased $T_{R/T}$ to 137°C and T_C to approximately 200°C [35, 36, 38-40] with minimal degradation of the piezoelectric or electromechanical properties. Ternary lead indium niobate – lead magnesium niobate – lead titanate, $x Pb(In_{1/2}Nb_{1/2})O_3\text{-}(1\text{-}x\text{-}y)Pb(Mg_{1/3}Nb_{2/3})O_3\text{-}yPbTiO_3$ (PIN-PMN-PT) [41-44] can be grown in large boules with high quality [35, 40, 41].

Ternary PIN-PMN-PT single crystals have higher phase transition thresholds, higher Curie temperatures, and a higher coercive field (E_C up to 0.7 MV/m) [35, 38-40, 45] than binary PMN-PT. This expands the thermal and electrical operating ranges and reduces the temperature dependence of the material constants [35, 46].

PIN-PMN-PT at room temperature with zero externally applied loads can be in either the ferroelectric rhombohedral (FE_R) phase (at low PT compositions) or the ferroelectric tetragonal (FE_T) phase (at high PT compositions) [72]. These two phases are separated by a MPB. The material properties are a function of electrical and mechanical load, temperature, composition, and orientation. Figure 4-1 shows the room temperature and zero load phase diagram of PIN-PMN-PT. The rhombohedral phase is to the left of the MPB and the tetragonal phase is to the lower right. The dotted curve separating the two phases represents the MPB. The six dots represent the compositions characterized in this study.

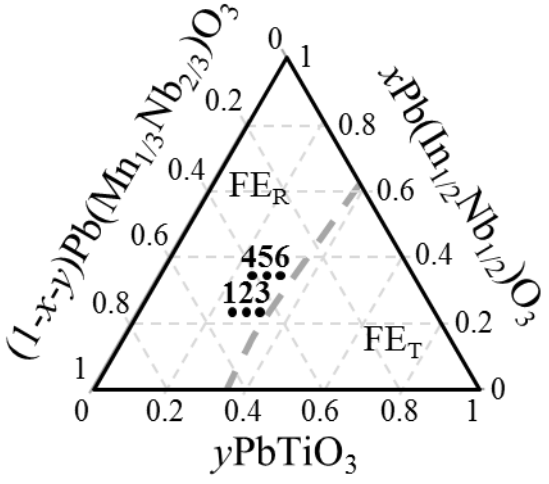

Figure 4-1. PIN-PMN-PT phase diagram at room temperature with zero mechanical or electrical loading. The points represent the compositions characterized in this study.

Domain wall motion is the dominant loss mechanism in ferroelectrics. In certain crystal cuts the crystals can be loaded both electrically and mechanically without producing a driving force for domain wall motion. This is often referred to as domain engineering. The $[011]_C$ cut and poled crystals are in a domain engineered two variant state that results in a negative d_{32} piezoelectric coefficient, a positive d_{31} piezoelectric coefficient, low hysteresis and dielectric loss, and high electro-mechanical coupling efficiency [17, 84, 115]. As the electric field and the stress are increased, the material undergoes a field induced phase transformation. This results in hysteresis, a significant increase in dielectric loss, and the introduction of non-linear material behavior. The field induced phase transformation is from FE_R to ferroelectric orthorhombic (FE_O) under mechanical and electrical loading of the $[011]_C$ cut [68, 116, 117]. The effect of the FE_R-FE_O transformation is observed as a jump in strain and electric displacement as well as an order of magnitude decrease in the piezoelectric, compliance, and dielectric constants [16, 63].

Figures 4-2(a) and (b) depict the cubic referenced coordinate system and the $[011]_C$ crystal cut, a 45 degree rotation about the $[100]_C$ axis. When the crystal is poled along the $[011]_C$ direction, the FE_R crystals forms a macroscopic *mm*2 symmetry [17, 36, 118] with the two $[111]_C$ FE_R variants closest to the poling direction being populated. The volume average remanent polarization (P_r) is in the $[011]_C$ direction. The $[011]_C$ direction is denoted the x_3 axis, the $[0\bar{1}1]_C$ direction the x_1 axis, and the $[100]_C$ direction the x_2 axis. The cubes shown in Figure 4-2 are oriented with the quasi-cubic lattice.

In applications the crystals are often mechanically pre-loaded in the $[100]_C$ direction and unipolar electric field is applied in the $[011]_C$ direction. This stress and this electric field each produce a driving force for the FE_R to FE_O phase transformation. Under small applied stress and

electric field at room temperature the crystal is in the two-variant $[111]_C$ rhombohedral state with the volume average P_r in the $[011]_C$ direction as shown in Figure 4-2(b). As the compressive stress (σ_{22}) increases beyond a certain threshold in the $[100]_C$ direction, the FE_R-FE_O phase transformation occurs as shown in Figure 4-2(c). As electric field (E_3) increases in the $[011]_C$ direction beyond a certain threshold the same FE_R-FE_O phase transformation occurs, as shown in Figure 4-2(d). Concurrent $[100]_C$ mechanical loading and $[011]_C$ electrical loading drive the FE_R-FE_O phase transformation at lower threshold levels than either load alone. When the $[011]_C$ poled crystal passes through the field induced phase transformation, a single $[011]_C$ FE_O variant becomes populated. There is a jump in polarization in the $[011]_C$ direction, a jump in elongation in the $[011]_C$ direction, and contraction in the $[100]_C$ direction. In this work the combined effects of composition, electric field, stress, and temperature on the piezoelectric, dielectric, and elastic properties and on field induced phase transformations in PIN-PMN-PT single crystals are experimentally characterized. An analysis of the mechanical and electrical works required for the onset of the FE_R-FE_O phase transformation is presented.

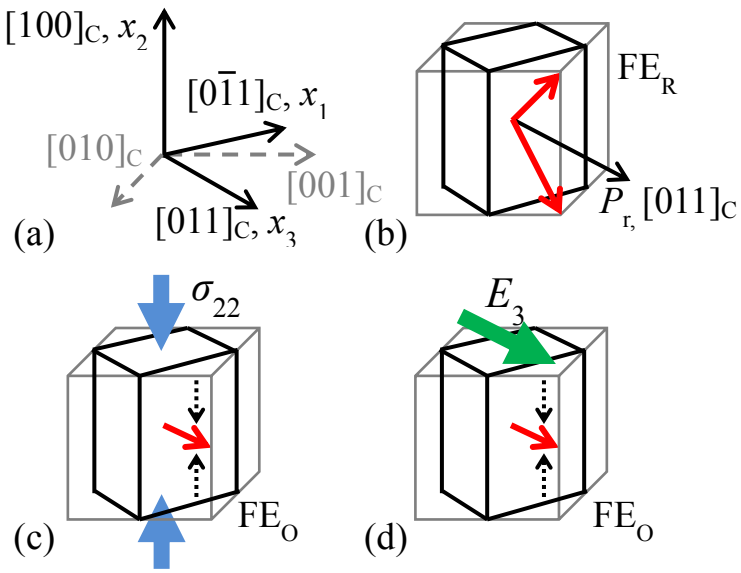

Figure 4-2. Domain states and field driven transformations for $[011]_C$ cut and poled ferroelectric PIN-PMN-PT single crystals. (a) The 45 degree axes rotation associated with the $[011]_C$ cut. (b) At room temperature with no external loads FE_R PIN-PMN-PT is in a two variant rhombohedral domain state with polarization in $[111]_C$ and volume average remanent polarization (P_r) in $[011]_C$. (c) Application of mechanical loads in $[100]_C$ and (d) electrical loads in $[011]_C$ induce a FE_R-FE_O phase transformation with polarization in $[011]_C$.

4.2. Experimental Approach

4.2.1. *Specimen Preparation*

$[011]_C$ oriented PIN-PMN-PT relaxor single crystal specimens were provided by H. C. Materials Corporation. The compositions studied are highlighted in the phase diagram shown in Figure 4-1. These compositions were approximately: 1) 0.24PIN-0.48PMN-0.28PT, 2) 0.24PIN-0.46PMN-0.30PT, 3) 0.24PIN-0.44PMN-0.32PT, 4) 0.32PIN-0.40PMN-0.28PT, 5) 0.32PIN-

0.38PMN-0.30PT, and 6) 0.32PIN-0.36PMN-0.32PT. All compositions are in the FE_R phase near the MPB. Specimens were cut to 4x4x12 mm^3. Sputtered gold electrodes were placed on the (011) and $(0\bar{1}\bar{1})$ faces. Wires were attached to the electrodes so that E_3 could be applied in the $[011]_C$ direction inducing axial strain (ε_{22}) and electric displacement (D_3). Strain gauges were attached to the centers of the $(0\bar{1}1)$ and $(01\bar{1})$ faces to measure ε_{22} and avoid any potential end effects from mechanical loading. Compressive σ_{22} was applied along the 12 mm $[100]_C$ axis.

4.2.2. *Experimental Arrangement*

The specimens were placed in a mechanical / electrical / thermal loading system. Stress was applied with a screw-driven load frame. Input voltage was applied with a 10 kV high voltage amplifier and voltage cycling was controlled with a function generator. Strain was measured using a Wheatstone bridge strain gauge amplifier and electric displacement was measured using a modified Sawyer Tower circuit. In this circuit the external capacitor was several orders of magnitude larger than the capacitance of the specimen. An electrometer was used to read the voltage across this capacitor. Electric displacement was calculated by dividing the charge by the electrode area. Electric field was calculated by dividing the applied voltage by the specimen thickness. The specimens were submerged in a flourinert bath to provide electrical insulation. A heating strip and thermocouple were placed within the flourinert bath to control the temperature. All voltages were filtered through 72 Hz low pass filters and recorded using a digital data acquisition system. The experimental loading arrangement is shown schematically in Figure 4-3.

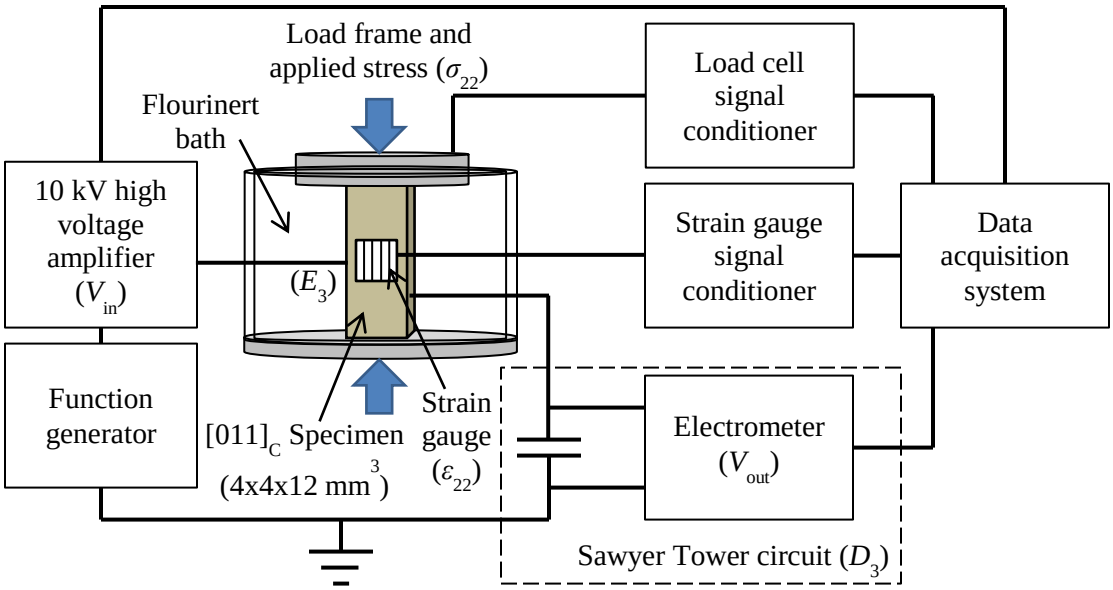

Figure 4-3. Experimental arrangement of the mechanical / electrical / thermal loading system for $[011]_C$ specimens.

The loading sequence was as follows: Electric field was linearly cycled at 0.2 Hz while stress was cycled at 0.625 MPa/s. The electric field was first cycled to the peak amplitude with zero preload stress. The preload stress was then increased and held constant while electric field was again cycled to the peak amplitude. This was repeated for five different preload stress increments. An additional electric field cycle was run after the peak preload stress. Stress was cycled to the peak amplitude with zero bias electric field. The bias electric field was then increased and held constant while stress was again cycled to the peak amplitude. This was repeated for five different bias electric field values. The electrical and mechanical loading sequences were repeated at temperatures of 25°C, 35°C, 45°C, 55°C, and 65°C. Table 4-1 describes the loading matrix. The maximum mechanical and electrical loading amplitudes were varied based on composition to ensure that each composition was driven completely through the

FE_R-FE_O phase transformation at each temperature. The loading sequence is shown schematically in Figure 4-4.

Once the electrical and mechanical loading sequences were completed, the specimens were thermally cycled from 25°C to 65°C. The electric displacement and strain changes were recorded in increments of 10°C. The pyroelectric coefficient and thermal expansion coefficient were calculated from a linear fit of the data.

Table 4-1. Experimental test matrix for $[011]_C$ specimens. Loading was repeated at temperatures of 25°C, 35°C, 45°C, 55°C, and 65°C.

Composition (PIN/PMN/PT)	σ_{22} (MPa)		E_3 (MV/m)		Temperature (°C)
	Preload	Peak	Bias	Peak	
0.24/0.44/0.32	0, -5, -10, -15, -20	-20	0, 0.31, 0.63, 0.94, 1.25	1.25	25, 35, 45, 55, 65
0.24/0.46/0.30	0, -9, -18, -27, -36	-36	0, 0.5, 1, 1.5, 2	2	25, 35, 45, 55, 65
0.24/0.48/0.28	0, -9, -18, -27, -36	-36	0, 0.5, 1, 1.5, 2	2	25, 35, 45, 55, 65
0.32/0.36/0.32	0, -7.5, -15, -22.5, -30	-30	0, 0.44, 0.88, 1.31, 1.75	1.75	25, 35, 45, 55, 65
0.32/0.38/0.30	0, -9, -18, -27, -36	-36	0, 0.5, 1, 1.5, 2	2	25, 35, 45, 55, 65
0.32/0.40/0.28	0, -9, -18, -27, -36	-36	0, 0.5, 1, 1.5, 2	2	25, 35, 45, 55, 65

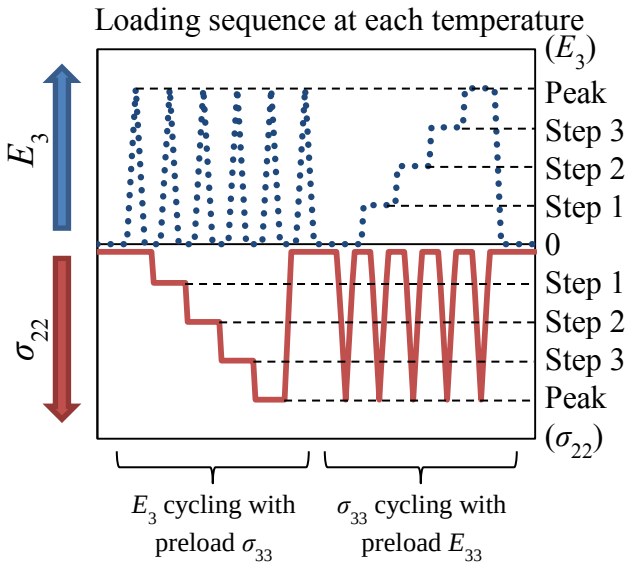

Figure 4-4. This loading sequence was repeated at temperatures of 25°C, 35°C, 45°C, 55°C, and 65°C.

4.3. Results

Figures 4-5, 4-6, and 4-7 show the 25°C D_3-E_3, ε_{22}-E_3, and ε_{22}-σ_{22} behavior of all six compositions. The piezoelectric (d_{32}), dielectric (κ_{33}^{σ}), and compliance (s_{22}^{E}) coefficients of each specimen were calculated along with the change in each coefficient with temperature ($\Delta d_{32}/\Delta T$, $\Delta \kappa_{33}^{\sigma}/\Delta T$, and $\Delta s_{22}^{E}/\Delta T$). For most compositions the rate of change of the material properties with temperature followed nearly linear behavior and was determined by a linear fit to the data. The thermal expansion (α_{22}) and pyroelectric coefficients (p_3) of each specimen were calculated from a zero load thermal cycle. The results for the zero preload stress and zero bias electric field at temperatures of 25°C, 45°C, and 65°C are listed in Table 4-2 for compositions with 0.24 PIN concentration and Table 4-3 for compositions with 0.32 PIN concentration. As the mechanical or electrical load is increased past a certain threshold level, the specimens undergo a field induced

phase transformation from FE_R to FE_O. Increasing stress preload as shown in Figures 4-5 and 4-6 increases the remanent polarization and remanent strain (the D_3-E_3 curves are shifted upward with the phase transformation shifted to the left, and the ε_{22}-E_3 curves are shifted downward with the phase transformation shifted to the left), and increasing the electric field bias as shown in Figure 4-7 increases the remanent strain prior to electric field or mechanical cycling (the ε_{22}-σ_{22} curves are shifted downward and the phase transformation is shifted to the right). The shifts within the rhombohedral phase are due to the piezoelectric effect. The shifts of the phase transformation to lower levels when a bias is applied is due to the combined driving force of the electrical and mechanical loads. There is no significant change in the FE_R or FE_O material coefficients as the preload stress or bias electric field is increased. Similarly there is not much change in the hysteresis between the forward and reverse phase transformations associated with the bias electrical or mechanical loads. Increasing the PIN concentration caused the transformation threshold to increase while decreasing the compliance, dielectric, and piezoelectric coefficients. Increasing the PT composition had the opposite effect. Increasing the PT concentration decreased the threshold field of transformation while increasing the material coefficients. Changing the PT concentration also resulted in changes to the phase transformation behavior of PIN-PMN-PT.

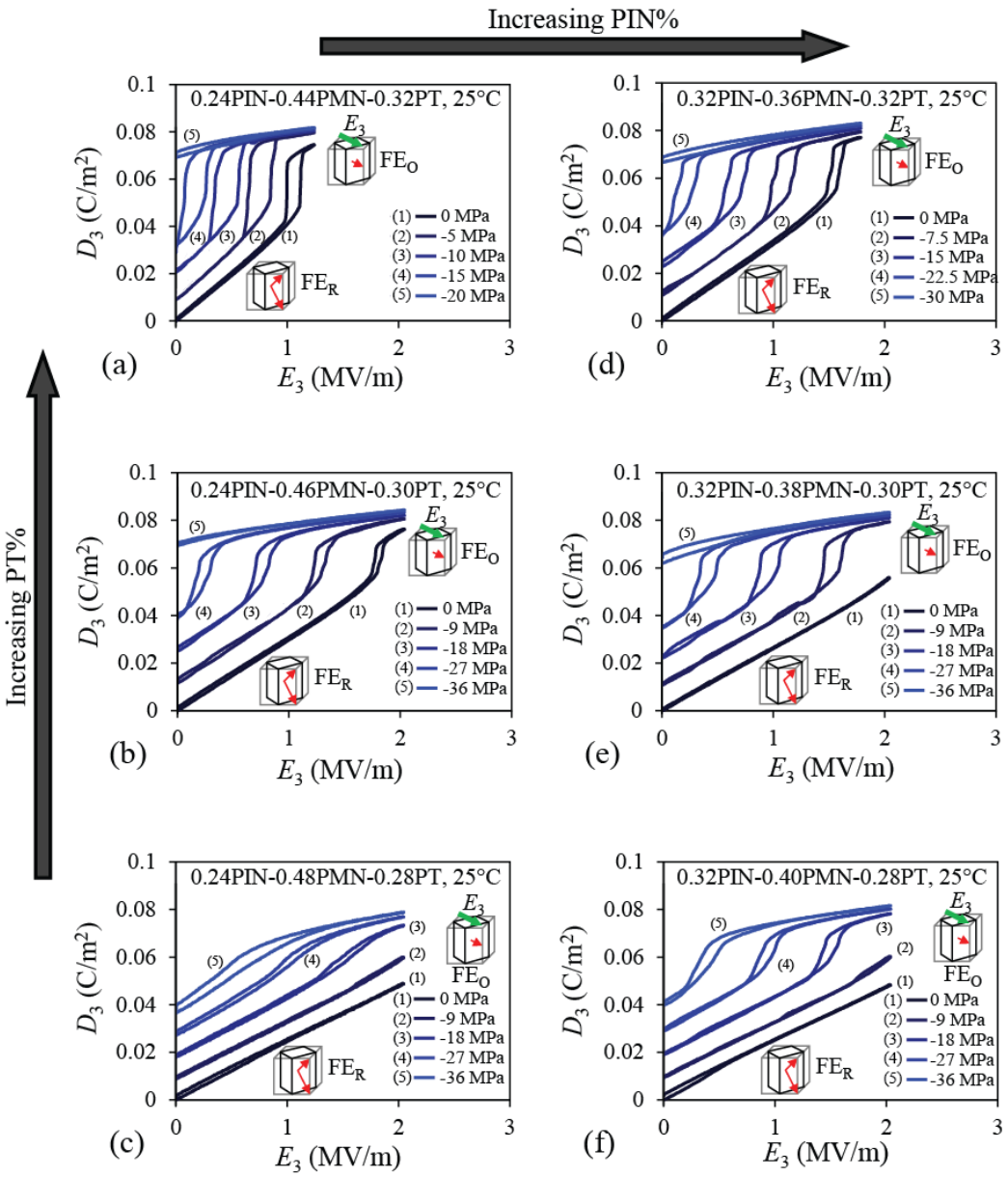

Figure 4-5. κ_{33}^{σ} dielectric behavior of D_3-E_3 with constant preload σ_{22} at 25°C for (a) 0.24PIN-0.44PMN-0.32PT, (b) 0.24PIN-0.46PMN-0.30PT, (c) 0.24PIN-0.48PMN-0.28PT, (d) 0.32PIN-0.36PMN-0.32PT, (e) 0.32PIN-0.38PMN-0.30PT, and (f) 0.32PIN-0.40PMN-0.28PT. Note the difference in preload stress and electric field loading amplitude for each composition according to Table 4-1. Error bars are not shown as they are roughly the width of the data lines. Experimental error: $D_3 \sim \pm 0.001$ C/m^2, and $E_3 \sim \pm 0.01$ MV/m.

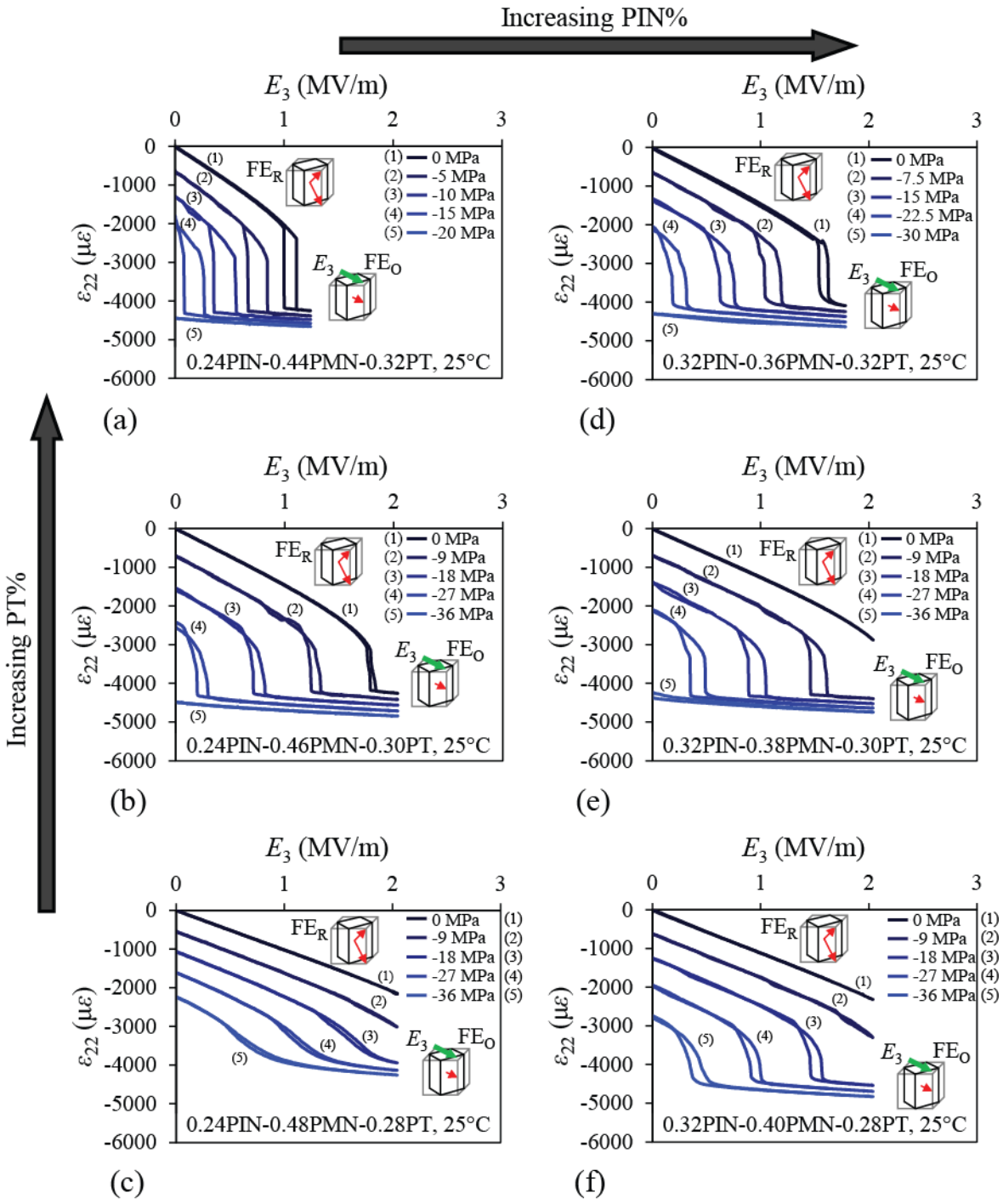

Figure 4-6. ε_{22}-E_3 with constant preload σ_{22} at 25°C for (a) 0.24PIN-0.44PMN-0.32PT, (b) 0.24PIN-0.46PMN-0.30PT, (c) 0.24PIN-0.48PMN-0.28PT, (d) 0.32PIN-0.36PMN-0.32PT, (e) 0.32PIN-0.38PMN-0.30PT, and (f) 0.32PIN-0.40PMN-0.28PT. Error bars are not shown as they are roughly the width of the data lines. Experimental error: $\varepsilon_{22} \sim \pm 20$ με, and $E_3 \sim \pm 0.01$ MV/m.

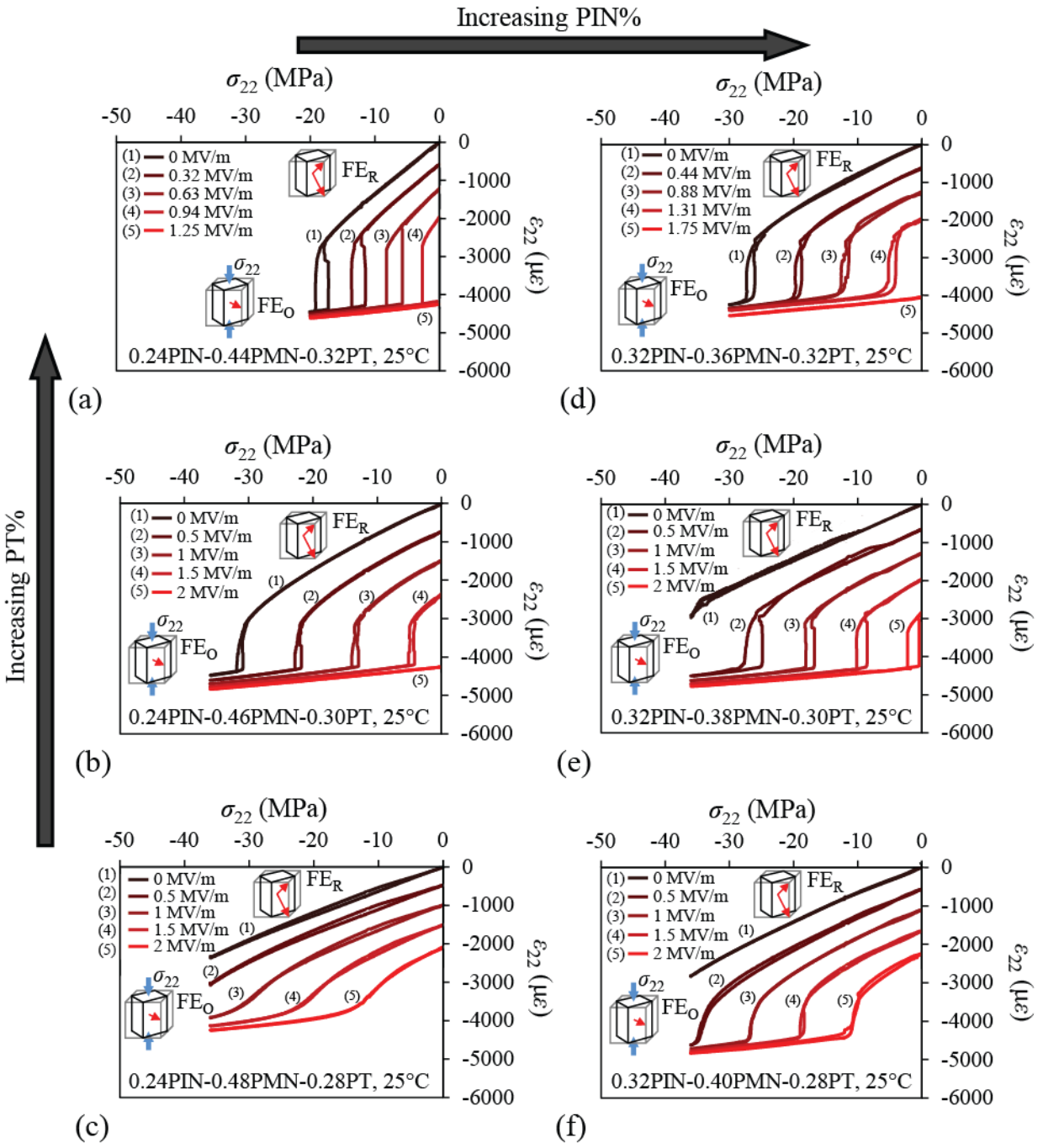

Figure 4-7. ε_{22}-σ_{22} at constant bias E_3 at 25°C for (a) 0.24PIN-0.44PMN-0.32PT, (b) 0.24PIN-0.46PMN-0.30PT, (c) 0.24PIN-0.48PMN-0.28PT, (d) 0.32PIN-0.36PMN-0.32PT, (e) 0.32PIN-0.38PMN-0.30PT, and (f) 0.32PIN-0.40PMN-0.28PT. Error bars are not shown as they are roughly the width of the data lines. Experimental error: $\varepsilon_{22} \sim \pm 20$ με, and $\sigma_{22} \sim \pm 0.1$ MPa.

The effects of changing the PT concentration, the PIN concentration, the applied stress, and the temperature on the material behavior of D_3-E_3 are shown in Figure 4-8 and of ε_{22}-E_3 in Figure 4-9. The cubic elements shown in Figures 4-8 and 4-9 indicate the variants of each phase that are present, where FE_R is in the two $<111>_C$ variant state and FE_O is in the one $[011]_C$ variant state.

The D_3-σ_{22} and the ε_{22}-σ_{22} behavior are similar. When the dielectric constant increased, the piezoelectric constant and compliance constant also increased.

The effect of increasing the PT concentration to move the composition toward the MPB is shown in panes (a) (compositions 1, 2, and 3 as labeled Figure 4-1). Compositions closer to the MPB have larger dielectric, piezoelectric, and compliance constants (slopes of the curves); and the phase transformation threshold is decreased.

The effect of increasing the PIN concentration on the compositions closest to the MPB is displayed in panes (b) for 0.32 PT at room temperature under no applied preload. This represents moving parallel to the MPB (composition 3 to composition 6 in Figure 4-1). Increasing the PIN at fixed concentration of PT results in a decrease of the dielectric, piezoelectric, and compliance coefficients and an increase in the threshold field for the phase transformation.

The effect of temperature at zero stress preload is shown in panes (c) for 0.24PIN-0.44PMN-0.32PT. Increasing temperature had little effect on the phase transformation hysteresis width or the jumps in strain and polarization associated with the transformation. However, increasing temperature decreased the transformation threshold field while increasing the compliance, piezoelectric, and dielectric coefficients.

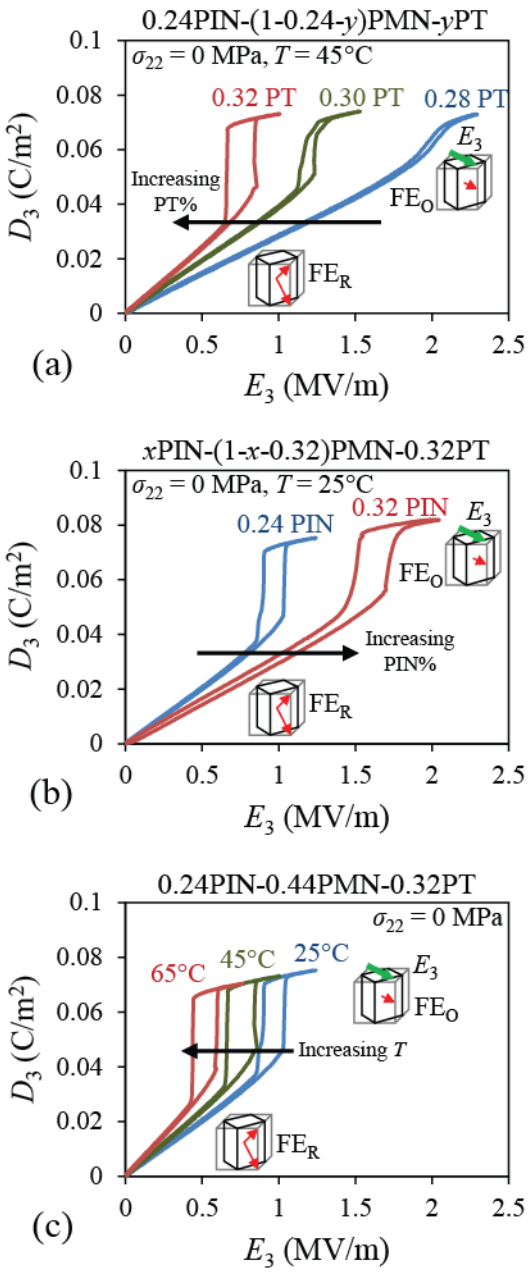

Figure 4-8. The effect on the D_3-E_3 behavior of (a) PT concentration at 25°C with zero σ_{22} preload, (b) PIN concentration at 25°C with zero σ_{22} preload, and (c) temperature. Error bars are not shown as they are roughly the width of the data lines. Experimental error: $D_3 \sim \pm 0.001$ C/m^2, and $E_3 \sim \pm 0.01$ MV/m.

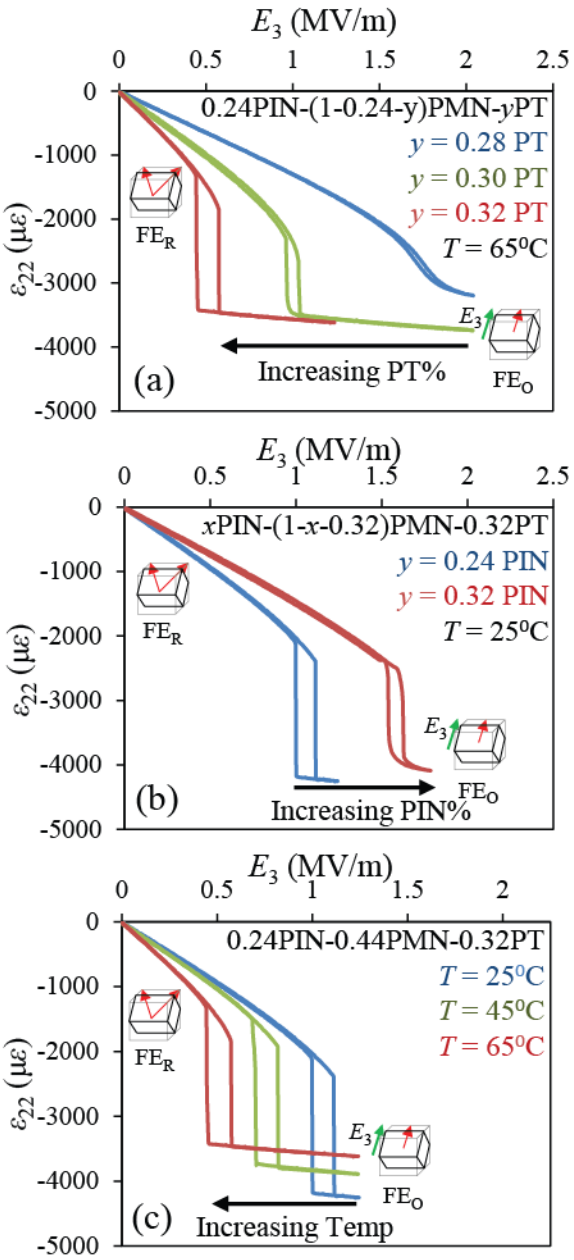

Figure 4-9. The effect on the ε_{22}-E_3 behavior for (a) PT composition of 0.24PIN-(1-0.24-*y*)PMN-*y*PT at 65°C, (b) PIN composition of *x*PIN-(1-*x*-0.32)PMN-0.32PT at 25°C, and (c) 0.24PIN-0.44PMN-0.32PT at different temperatures.

Table 4-2. Experimentally measured FE_R and FE_O material coefficients for each composition with 0.24 PIN concentration at 25°C, 45°C, and 65°C.

Composition	Material Property	T (°C)	0.28 PT		0.30 PT		0.32 PT	
			FE_R	FE_O	FE_R	FE_O	FE_R	FE_O
0.24 PIN	Piezoelectric d_{32} (ε_{22}/E_3, pCN^{-1})	25	-1020	--	-1490	-266	-1770	-214
		45	-1190	--	-1620	-257	-2020	-283
		65	-1340	-358	-2020	-259	-2710	-277
		$\Delta d_{32}/\Delta T$	-7.4	--	-13.3	--	-25.2	--
	Dielectric $\kappa_{33}^{\sigma}/\kappa_0$ (κ_0=8.855e^{-12} Fm^{-1})	25	2650	--	3330	--	4040	--
		45	3240	--	4290	1215	5470	1430
		65	3690	--	4570	960	6380	883
		$\Delta\kappa_{33}^{\sigma}/\Delta T$	29.9	--	31.1	--	58.0	--
	Compliance s_{22}^{E} (10^{-12} Pa^{-1})	25	62	--	81	20	147	23
		45	65	--	81	25	115	20
		65	70	--	94	26	183	18
		$\Delta s_{22}^{E}/\Delta T$	0.2	--	0.4	--	1.3	--
	Thermal expansion α_{22} ($\mu\varepsilon K^{-1}$)	--	-8.3	--	-6.4	--	-8.6	--
	Pyroelectric p_3 ($\mu Cm^{-2}K^{-1}$)	--	-550	--	-590	--	-650	--

Table 4-3. Experimentally measured FE_R and FE_O material coefficients for each composition with 0.32 PIN concentration at 25°C, 45°C, and 65°C.

Composition	Material Property	T (°C)	0.28 PT		0.30 PT		0.32 PT	
			FE_R	FE_O	FE_R	FE_O	FE_R	FE_O
0.32 PIN	Piezoelectric d_{32} (ε_{22}/E_3, pCN^{-1})	25	-710	--	-1180	--	-1440	-428
		45	-520	-200	-1570	-272	-1630	-242
		65	-640	-115	-1660	-187	-1990	-296
		$\Delta d_{32}/\Delta T$	-5.6	--	-10.6	--	-18.5	--
	Dielectric $\kappa_{33}^{\sigma}/\kappa_0$ (κ_0=8.855e^{-12} Fm^{-1})	25	2730	--	3150	--	3730	--
		45	3700	--	3370	--	4120	1264
		65	4280	975	3820	932	5850	1049
		$\Delta\kappa_{33}^{\sigma}/\Delta T$	38.6	--	19.0	--	53.8	--
	Compliance s_{22}^{E} (10^{-12} Pa^{-1})	25	53	--	77	--	77	27
		45	40	19	87	24	96	24
		65	51	8	91	16	106	27
		$\Delta s_{22}^{E}/\Delta T$	0.0	--	0.3	--	0.7	--
	Thermal expansion α_{22} ($\mu\varepsilon K^{-1}$)	--	-6.6	--	-4.5	--	-4.4	--
	Pyroelectric p_3 ($\mu Cm^{-2}K^{-1}$)	--	-500	--	-550	--	-620	--

The two dimensional D_3-E_3, ε_{22}-E_3, and ε_{22}-σ_{22} plots are part of a multiaxial surface. Figure 4-10 shows the D_3-σ_{22}-E_3 behavior and Figure 4-11 shows the ε_{22}-σ_{22}-E_3 behavior for 0.32PIN-(1-0.32-*y*)PMN-*y*PT. Two temperatures are shown to illustrate the effect of thermal loading on the phase transformation behavior. The initial planar region is associated with the rhombohedral phase while the secondary planar region at increased fields is associated with the orthorhombic phase. The nonlinear region between the two planar regions is associated with the

field induced FE_R-FE_O phase transformation. The FE_R planar region has a much steeper slope than the FE_O planar region.

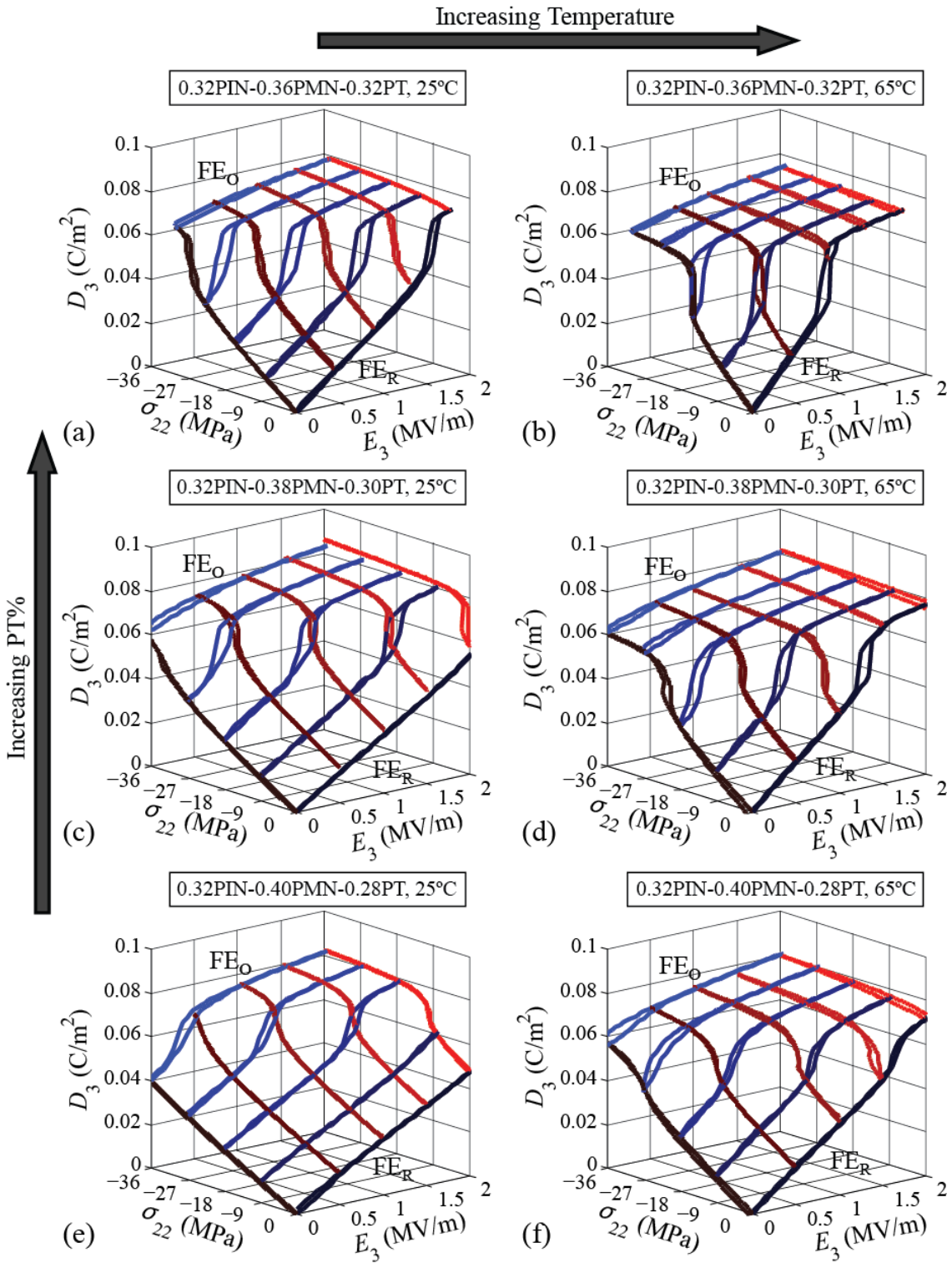

Figure 4-10. D_3-σ_{22}-E_3 phase transformation profile for 0.32PIN-(1-0.32-*y*)PMN-*y*PT for (a) and (b) y = 0.32, (c) and (d) y = 0.30, and (e) and (f) y = 0.28, at (a), (c), and (e) 25°C and (b), (d),

and (f) 65°C. Error bars are not shown as they are roughly the width of the data lines. Experimental error: $D_3 \sim \pm 0.001$ C/m^2, $E_3 \sim \pm 0.01$ MV/m, and $\sigma_{22} \sim \pm 0.1$ MPa.

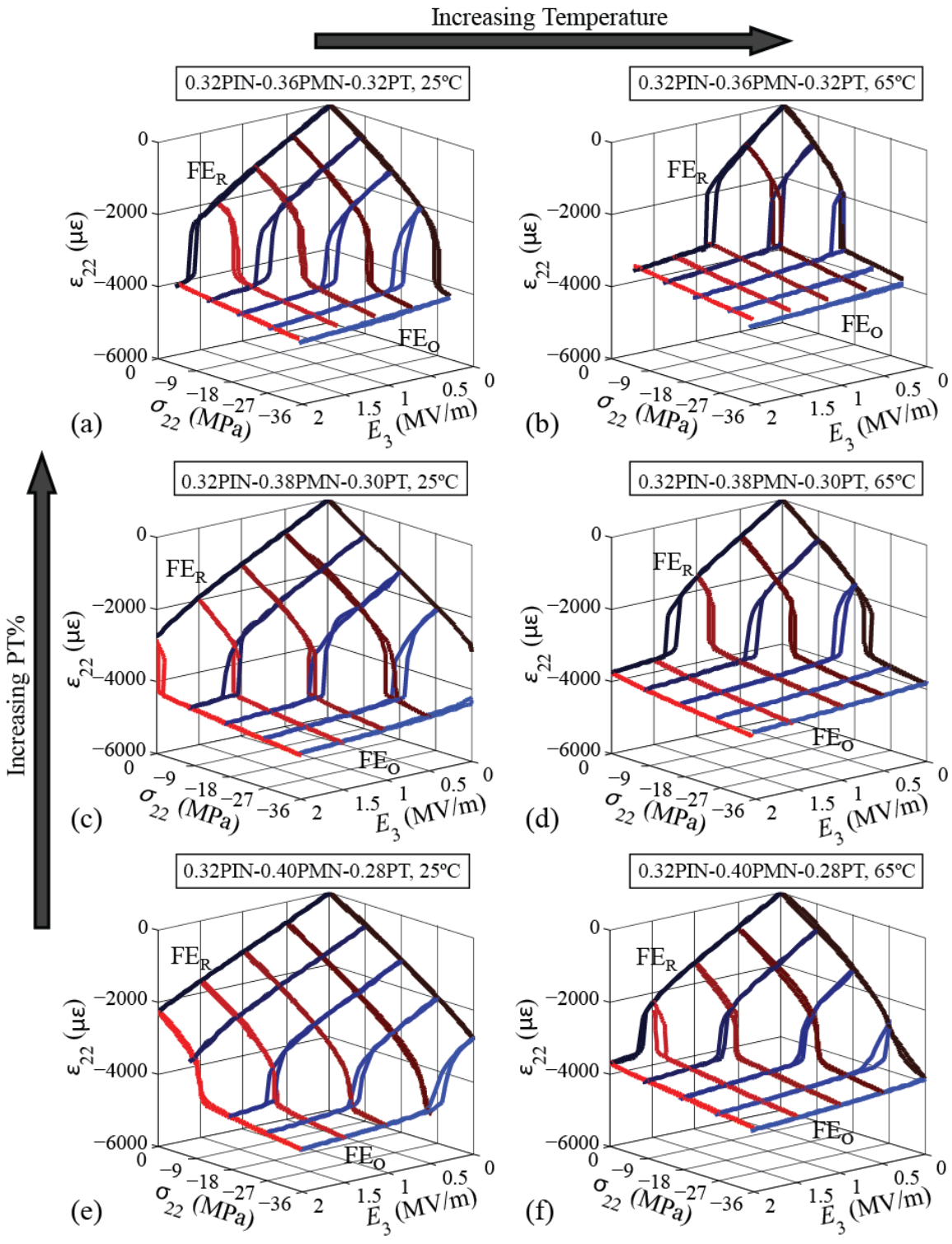

Figure 4-11. ε_{22}-σ_{22}-E_3 phase transformation profile for 0.32PIN-(1-0.32-*y*)PMN-*y*PT for (a) and (b) y = 0.32, (c) and (d) y = 0.30, and (e) and (f) y = 0.28, at (a), (c), and (e) 25°C and (b), (d),

and (f) 65°C. Error bars are not shown as they are roughly the width of the data lines. Experimental error: $\varepsilon_{22} \sim \pm 20$ με, $E_3 \sim \pm 0.01$ MV/m, and $\sigma_{22} \sim \pm 0.1$ MPa.

4.4. Analysis and Discussion

In PIN-PMN-PT single crystals the applied mechanical and electrical loads combine linearly to drive the FE_R-FE_O phase transformation [6]. In the case of $[011]_C$ crystals the applied mechanical and electrical loads each result in a positive driving force for the FE_R to FE_O phase transformation and increasing the temperature reduces the energy barrier to the phase transformation. As the electrical and mechanical loads are increased at a given temperature, the potential energy of the crystal is increased until it reaches a threshold level where the transformation occurs. Since the transformation field is a linear function of the applied mechanical and electrical loads, the total work required for transformation at a constant temperature is constant. This means there is a scalar energy barrier to the transformation.

When a mechanical or electrical bias is applied, the preload drives the specimen toward the transformation resulting in a reduced threshold amplitude required to induce the phase transformation during cycling. The energy barrier to the forward transformation is reduced as the PT concentration is increased to bring the composition closer to the MPB. Increasing the PIN stabilized the FE_R phase and increased the energy barrier to the forward transformation. In Figure 4-12 the electrical and mechanical transformation threshold of each composition are plotted as a function of temperature. The data for each composition falls onto parallel curves.

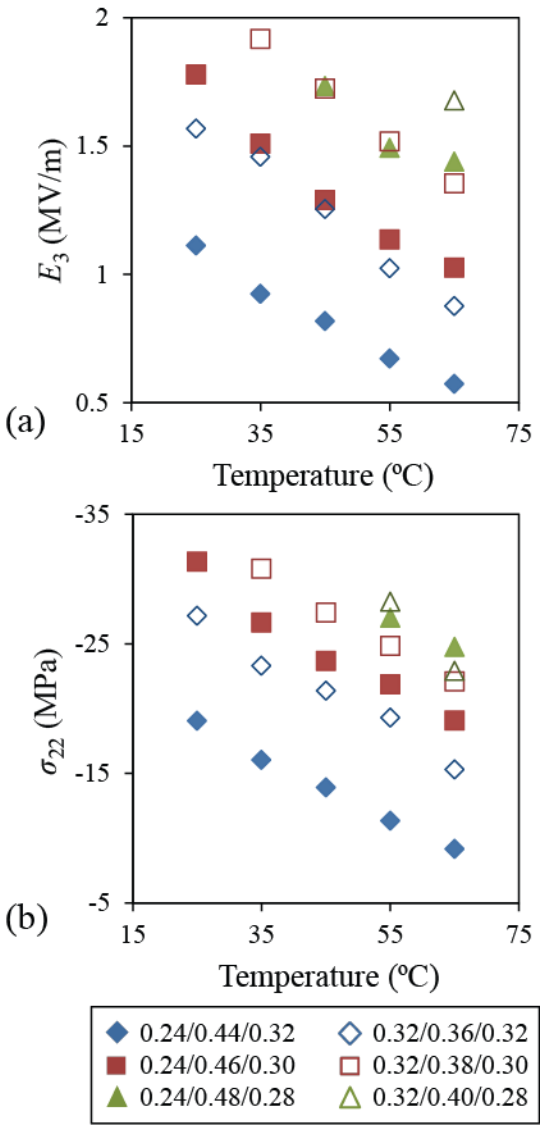

Figure 4-12. (a) PIN-PMN-PT E_3-T phase diagram. (b) PIN-PMN-PT σ_{22}-T phase diagram. Compositions are shown as PIN/PMN/PT.

The transformation threshold under combined stress and electric field loading was determined for each composition at each temperature. The thresholds for the onsets of the forward FE_R-FE_O and reverse FE_O-FE_R transformations are plotted in Figure 4-13 for the three PT compositions with 0.24 PIN. (a), (b) and (c) show the σ_{22}-E_3-T threshold for transformation

while (d), (e), and (f) are edge views of the two nearly parallel planes associated with the FE_R-FE_O and FE_O-FE_R transformations. At fields below the forward FE_R-FE_O transformation plane, PIN-PMN-PT follows nearly linear FE_R behavior. At fields above the reverse FE_O-FE_R transformation plane PIN-PMN-PT follows nearly linear FE_O behavior. Because the FE_R phase has a higher compliance and permittivity than the FE_O phase, the strain and electric displacement changes during the forward FE_R to FE_O transformation are smaller than the strain and electric displacement changes during the reverse FE_O to FE_R transformation. In Figure 4-13 (a) and (d), for 0.24PIN-0.48PMN-0.28PT, the start of the reverse FE_O-FE_R transformation occurs at higher fields than the start of the forward FE_R-FE_O transformation. However, in Figure 4-13 (c) and (f), for 0.24PIN-0.44PMN-0.32PT, the start of the reverse FE_O-FE_R transformation occurs at lower fields than the start of the forward FE_R-FE_O transformation. This is directly related to whether the phase transformation is distributed over a range of fields or is a discontinuous jump at a single transformation field. Equations for the forward and reverse transformation as a function of stress, electric field, and temperature for each composition were determined by least square fitting the data and are listed in Table 4-4 along with an extrapolated zero stress and zero electric field transformation temperature. Decreasing the PT concentration or increasing the PIN concentration reduced the temperature dependence of the transformation planes. This appears as a reduction of slope with respect to temperature.

The σ_{22}-E_3-T phase transformation thresholds for the onset of the FE_R to FE_O phase transformation were used to evaluate the total work required to induce the FE_R-FE_O transformation. This threshold can be used to identify the limit of the linear FE_R behavior. In the $[011]_C$ cut and poled single crystals, the $[011]_C$ electric field and the $[001]_C$ compressive stress

each do positive work on the crystal as it approaches through the transformation. The total work, equation (4-1),

$$w^{\text{total}} = w^{\text{m}} + w^{\text{e}} = \int \sigma_{ij} \mathrm{d}\varepsilon_{ij} + \int E_m \mathrm{d}D_m \,, \tag{4-1}$$

is the sum of the mechanical (w^{m}) and electrical (w^{e}) work and is calculated through numerical integration of the ε-σ and D-E curves. Indices i, j, and m vary from 1 to 3. The total work required for the onset of the transformation is constant for a specific composition at a specific temperature. The work constant (w^{C}) can be calculated through numerical integration from the start of the curve to the transformation threshold ($\sigma^{\text{threshold}}$ for mechanical loads and $E^{\text{threshold}}$ for electrical loads) by following any loading path, equation (4-2),

$$w^{\text{C}} = \int_0^{\sigma^{\text{threshold}}} \sigma_{22} \mathrm{d}\varepsilon_{22} + \int_0^{E^{\text{threshold}}} E_3 \mathrm{d}D_3 \,. \tag{4-2}$$

This work constant results in a single data point for any combination of electrical and mechanical loads at the onset of the FE_R-FE_O transformation and is equated to the change of Helmholtz energy of the crystal. The Helmholtz energy density (work / volume) is plotted as a function of temperature for each composition as shown in Figure 4-14. This energy density at the onset of the transformation is taken to be the energy barrier to the start of the phase transformation. The energy barrier as a function of temperature has some non-linearity with temperature as seen in Figure 4-14. The energy barriers plotted as a function of temperature for the different

compositions have the same shape but with a constant offset. Increasing temperature, increasing the PT concentration, and decreasing the PIN concentration each reduces the energy barrier.

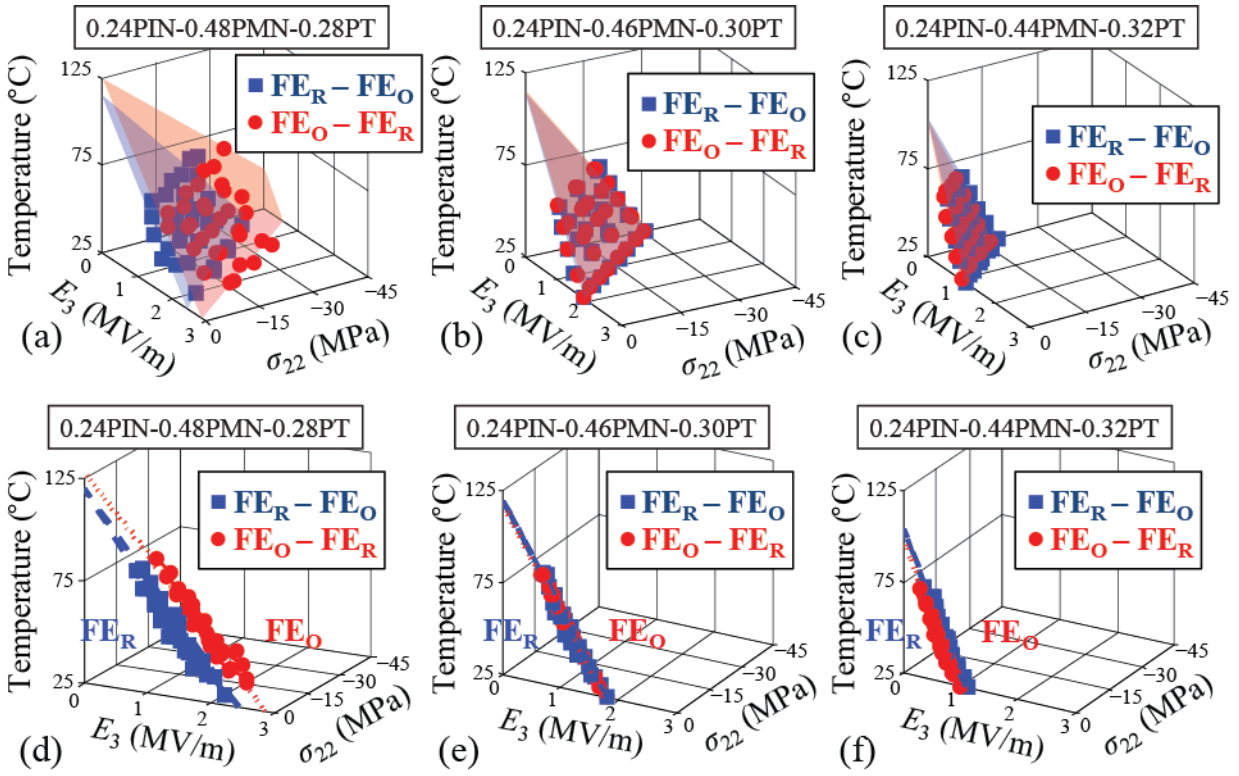

Figure 4-13. σ_{22}-E_3-T phase transformation thresholds corresponding to the FE_R-FE_O phase transformation under combined electrical, mechanical, and thermal loads for (a) and (d) 0.24PIN-0.48PMN-0.28PT, (b) and (e) 0.24PIN-0.46PMN-0.30PT, and (c) and (f) 0.24PIN-0.44PMN-0.32PT. The axes in (d), (e), and (f) have been rotated to show edge view of the planes. Experimental error of the data points corresponding to the start of transformation was σ_{22} ~ ± 0.1 MPa, E_3 ~ ± 0.01 MV/m, and T ~ ± 0.5°C. Error bars are not shown for visualization of the data purposes.

Table 4-4. σ_{22}-E_3-T phase transformation plane equations and thermal FE_R-FE_O transformation ranges.

Composition (PIN/PMN/PT)	FE_R-FE_O Plane	FE_O-FE_R Plane	Thermal (°C) FE_R-FE_O	Thermal (°C) FE_O-FE_R
0.24/0.44/0.32	$T = 4.05\sigma_{22} - 72.4E_3 + 104$	$T = 4.43\sigma_{22} - 76.9E_3 + 98.9$	104	98.9
0.24/0.46/0.30	$T = 3.04\sigma_{22} - 53.4E_3 + 120$	$T = 3.03\sigma_{22} - 53.4E_3 + 118$	120	118
0.24/0.48/0.28	$T = 2.29\sigma_{22} - 38.9E_3 + 120$	$T = 1.89\sigma_{22} - 36.2E_3 + 128$	120	128
0.32/0.36/0.32	$T = 3.42\sigma_{22} - 58.0E_3 + 116$	$T = 3.43\sigma_{22} - 57.7E_3 + 115$	116	115
0.32/0.38/0.30	$T = 3.31\sigma_{22} - 52.8E_3 + 138$	$T = 3.11\sigma_{22} - 52.2E_3 + 130$	138	130
0.32/0.40/0.28	$T = 2.91\sigma_{22} - 41.8E_3 + 135$	$T = 2.37\sigma_{22} - 37.6E_3 + 136$	135	136

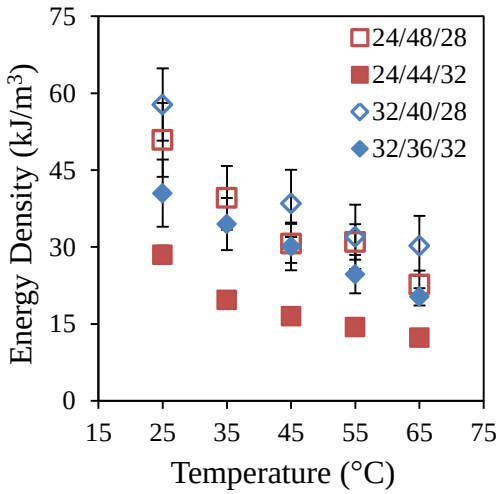

Figure 4-14: Energy barrier to the FE_R-FE_O transformation start (compositions are listed as PIN/PMN/PT). Error bars show 1 standard deviation of the data used to calculate the energy density. Error in the temperature was less than ± 0.5°C. The energy density for 0.24PIN-0.46PMN-0.30PT and 0.32PIN-0.38PMN-0.30PT fell between the respective other compositions and has been removed for clarity of the data. Error bars for 0.24PIN-0.44PMN-0.32PT are the size of the data points and are therefore not visible.

4.5. Concluding Remarks

The large field strain (ε_{22}) and electric displacement (D_3) behavior of piezoelectric mode d_{32} $[011]_C$ cut FE_R PIN-PMN-PT was experimentally characterized under combined mechanical, electrical, and thermal loads. Increasing temperature caused an increase in the linear FE_R material properties and a decrease in the coercive field of FE_R-FE_O transformation. Increasing the preload stress or bias electric field was found to have a negligible effect on the material properties and only acted to reduce the coercive field of transformation. The effect of composition on the FE_R-FE_O phase transformation behavior was characterized by examining the transformation behavior of 0.24 PIN and 0.32 PIN with 0.28, 0.30, and 0.32 PT compositions near the MPB. Small changes in composition were found to result in large changes in the FE_R-FE_O transformation behavior. 0.32 PT compositions near the MPB had the largest linear material constants and experienced a discontinuous transformation with large changes in strain and polarization at low coercive fields. 0.28 PT compositions further from the MPB experienced a transformation distributed across a range of fields at substantially larger applied fields. The material constants for 0.28 PT were found to be approximately half those of 0.32 PT.

The energy barrier to the onset of the field induced phase transformation was determined by measuring the mechanical work required to start the transformation and this energy barrier was compared for the different compositions. Although this represents a good measure of the onset of non-linearity and hysteresis associated with the transformation, the energy barrier to driving the material 50% of the way through the transformation and the energy barrier to the reverse transformation could also be defined. The energy barrier to the start of the transformation and the energy barrier to the completion of the transformation in both the forward and reverse directions will provide a more detailed understanding of the phase transformation behavior.

Increasing the PIN composition was found to increase the energy barrier to the field induced phase transformation.

Phase transformations are currently being studied for energy harvesting applications [6] but need to be avoided for transducer applications. It is apparent from the presented results that small changes in PIN-PMN-PT composition may have large effects on device designs that are sensitive to material constants and material loss, and that the effect of mechanical preload stress and temperature changes may affect the relative benefits of a specific composition. From the results, compositions away from the MPB with large PIN and small PT compositions may be beneficial for transducer applications that require extended linear response regions; however these compositions will require a larger drive field to obtain the same strain output. Compositions near the MPB with small PIN and large PT compositions may be beneficial for energy harvesting applications that utilize the large discontinuous jump in strain and polarization associated with the FE_R-FE_O phase transformation at low coercive fields.

CHAPTER 5

COMPOSITIONAL DEPENDENCE OF ELECTRO-MECHANICAL PROPERTIES AND FIELD INDUCED PHASE TRANSFORMATIONS IN $[001]_C$ PIN-PMN-PT SINGLE CRYSTALS

The compositional dependence of the electro-mechanical properties of $[001]_C$ cut and poled relaxor ferroelectric lead indium niobate – lead magnesium niobate – lead titanate, $x\text{Pb}(\text{In}_{1/2}\text{Nb}_{1/2})\text{O}_3\text{-}(1\text{-}x\text{-}y)\text{Pb}(\text{Mg}_{1/3}\text{Nb}_{2/3})\text{O}_3\text{-}y\text{PbTiO}_3$ (PIN-PMN-PT) single crystals was characterized under combined stress and electric field loading. Increasing the PIN and PT concentrations in compositions near the morphotropic phase boundary affected the piezoelectric, dielectric, and compliance coefficients, and the ferroelectric, pyroelectric, and thermal expansion coefficients, as well as the ferroelectric rhombohedral to ferroelectric orthorhombic phase transformation thresholds. The combinations of stress and electric field that induced the phase transformations were determined as a function of temperature. The results indicate that the linear response regime can be increased by modifying the composition, but this reduces the piezoelectric, dielectric, and compliance coefficients. This may be a desirable trade off in device design where linearity and low loss are important to the application.

The results of this study have been accepted for publication in *Smart Materials and Structures* [119] and submitted for publication in *IEEE Transactions on Ultrasonics, Ferroelectrics, and Frequency Control* [120].

5.1. Introduction

Relaxor ferroelectric ternary lead indium niobate – lead magnesium niobate – lead titanate, $x\text{Pb}(\text{In}_{1/2}\text{Nb}_{1/2})\text{O}_3\text{-}(1\text{-}x\text{-}y)\text{Pb}(\text{Mg}_{1/3}\text{Nb}_{2/3})\text{O}_3\text{-}y\text{PbTiO}_3$ (PIN-PMN-PT) single crystals were developed with the goal of expanding the thermal, mechanical, and electrical operating ranges while reducing the temperature dependence of the material coefficients. The operating electric field range of binary lead magnesium niobate – lead titanate, $(1\text{-}x)\text{Pb}(\text{Mg}_{1/3}\text{Nb}_{2/3})\text{O}_3\text{-}x\text{PbTiO}_3$ (PMN-*x*PT, $x = 0.28\text{-}0.33$) is limited by a low coercive field ($E_C \sim 0.25$ MV/m), and by a low depoling temperature ($T_{R/T} < 97$°C) and a low Curie temperature ($T_C \sim 150$°C) [35-37]. Ternary ferroelectric PIN-PMN-PT single crystals with compositions near the morphotropic phase boundary (MPB) have an increased coercive field (E_C up to 0.7 MV/m) and an increased $T_{R/T}$ and T_C ($T_{R/T}$ up to 137°C and T_C up to 200°C) [36, 39-41, 121] with electromechanical properties similar to the binary compositions [12, 60, 61]. The electromechanical properties of PIN-PMN-PT with compositions near the MPB make it useful in transducer applications such as sonar and medical ultrasound [1-5]. In resonant device applications requiring large amplitude drive electric fields, the crystals are often mechanically biased using a compressive stress preload. This can lead to non-linearity and hysteresis associated with a phase transformation. This needs to be avoided in some sonar transducer applications, but the large change of polarization over a small range of stress has been shown to be advantageous in energy harvesting applications [6].

The ternary phase diagram of PIN-PMN-PT at room temperature, zero stress, and zero electric field is shown in Figure 751. The material properties depend on composition, orientation, domain structure, and phase [17, 19]. At room temperature and zero applied load, PIN-PMN-PT occurs in the ferroelectric rhombohedral (FE_R) phase at low PT concentrations and in the

ferroelectric tetragonal (FE_T) phase at high PT concentrations [72]. These two phases are separated by a morphotropic phase boundary, a narrow region of compositions consisting of intermediary phases. The dotted curve separating the FE_R and FE_T phases represents compositions along the MPB. When the composition is close to the MPB on the rhombohedral side, the crystals exhibit enhanced electromechanical properties. The compositions that were characterized in this study are indicated by dots in Figure 5-1.

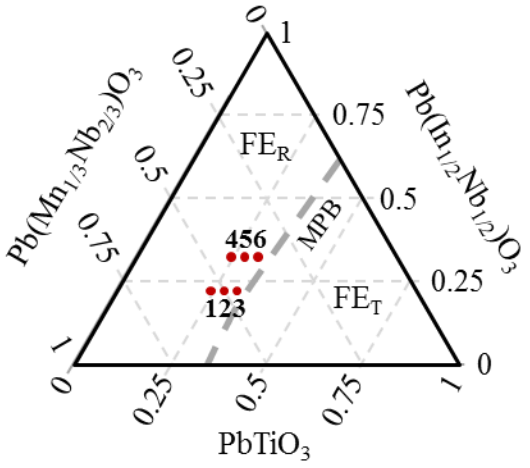

Figure 5-1. *x*PIN-(1-*x*-*y*)PMN-*y*PT room temperature phase diagram at zero stress and zero electric field. The points show the compositions used in this study.

The MPB shown in the ternary phase diagram shifts with temperature, stress, or electric field. Applied mechanical and electrical loads above a threshold amplitude induce phase transformations [16, 20, 63] with an associated jump in strain and electric displacement and an order of magnitude change in the material constants [20, 68, 116, 117]. Figure 5-2 depicts the stress and electric field induced phase transformations in $[001]_C$ rhombohedral relaxor single crystals. A FE_R crystal has eight variants with polarization in the $<111>_C$ directions, and a

ferroelectric orthorhombic (FE_O) crystal has 12 variants with polarization in the $<011>_C$ directions. The crystal variants of the $[001]_C$ cut and poled crystal relative to a cubic referenced coordinate system (Figure 5-2(a)) are shown in Figure 5-2(b). The poled crystal is initially in a four variant FE_R (4R) state with spontaneous polarization in the four $<111>_C$ directions closest to the $[001]_C$ poling direction. Application of a compressive stress (σ_{33}) in the $[001]_C$ direction drives the transition to a FE_O four variant state (4O) with polarization in the four $<110>_C$ directions perpendicular to the $[001]_C$ direction, Figure 5-2(c). In this process the polarization of each variant is believed to rotate through a monoclinic phase [122, 123]. When a bias stress drives the material to the (4O) state, an electric field (E_3) of sufficient amplitude applied in the $[001]_C$ direction will drive the crystal back to the (4R) state, overcoming the effect of the stress preload, Figure 2(d). Passing back and forth through the phase transformation results in non-linearity and hysteresis in strain and polarization. Finkel et al. characterized the strain discontinuity as a function of stress in one composition of $[001]_C$ PIN-PMN-PT associated with the FE_R-FE_O transformation [75].

In this work the effect of composition on the large field behavior of PIN-PMN-PT single crystals was characterized under thermal, electrical, and mechanical loads. The concentration of PIN and PT on compositions near the MPB was found to affect the linear material properties, nonlinear behavior, and the phase transformation threshold.

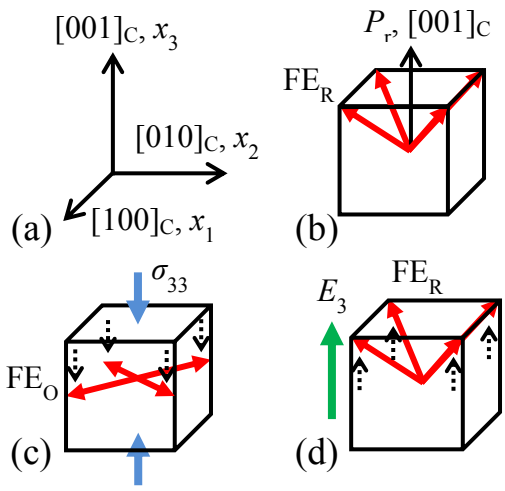

Figure 5-2. (a) The cubic axes associated with the $[001]_C$ cut. (b) The four arrows in the $[111]_C$ directions indicating the (4R) variants. (c) Application of compressive stress in $[001]_C$ drives the FE_R-FE_O transformation to the (4O) state. (d) Electric field drives the material back to the (4R) state.

5.2. Experimental Approach

5.2.1. *Specimen Preparation*

Relaxor PIN-PMN-PT single crystal specimens were grown by the Bridgeman growth method and were provided by H. C. Materials Corporation. The specimens were cut and poled in the $[001]_C$ orientation and had dimensions of 4x4x4 mm^3. Six compositions were provided: 1) 0.24PIN-0.48PMN-0.28PT, 2) 0.24PIN-0.46PMN-0.30PT, 3) 0.24PIN-0.44PMN-0.32PT, 4) 0.32PIN-0.40PMN-0.28PT, 5) 0.32PIN-0.38PMN-0.30PT, and 6) 0.32PIN-0.36PMN-0.32PT, as labeled in Figure 5-1. Gold electrodes were sputtered onto the $(001)_C$ and $(00\bar{1})_C$ faces.

The crystals were arranged into three element, 4x4x12 mm^3 stacks, shown schematically in Figure 5-3. The remanent polarization of adjacent specimens was in alternating directions and

the 12 mm axis was aligned with $[001]_C$. 0.05 mm thick copper shims with patterned holes to reduce in-plane stiffness were used to make electrical contact to the central crystal. Adjacent crystals were bonded to the copper shims with silver epoxy and wires were attached to alternate electrodes. Strain gauges were attached to opposite sides of the middle crystal. Strain readings were taken from the middle crystal to avoid possible end effects. Electric displacement readings represent the average response of the three crystals in the stack.

5.2.2. *Experimental Arrangement*

The specimens were placed in a mechanical / electrical / thermal loading system as shown schematically in Figure 5-3. Stress (σ_{33}, along the 12 mm axis) was applied with a screw-driven load frame. Input voltage was applied with a 10 kV high voltage power supply and voltage cycling was controlled with a function generator. Strain (ε_{33}) was measured with a Wheatstone bridge strain gauge amplifier and electric displacement (D_3) was measured using a modified Sawyer Tower circuit. Electric displacement was calculated by dividing the charge by the 48 mm^2 electrode area of the three cubes. Electric field (E_3) was calculated by dividing the applied voltage by the 4 mm thickness. The specimens were submerged in a flourinert bath to provide electrical insulation and thermal conduction. A heating strip and thermocouple were placed within the flourinert bath to control the temperature. All signals were filtered through 72 Hz low pass filters.

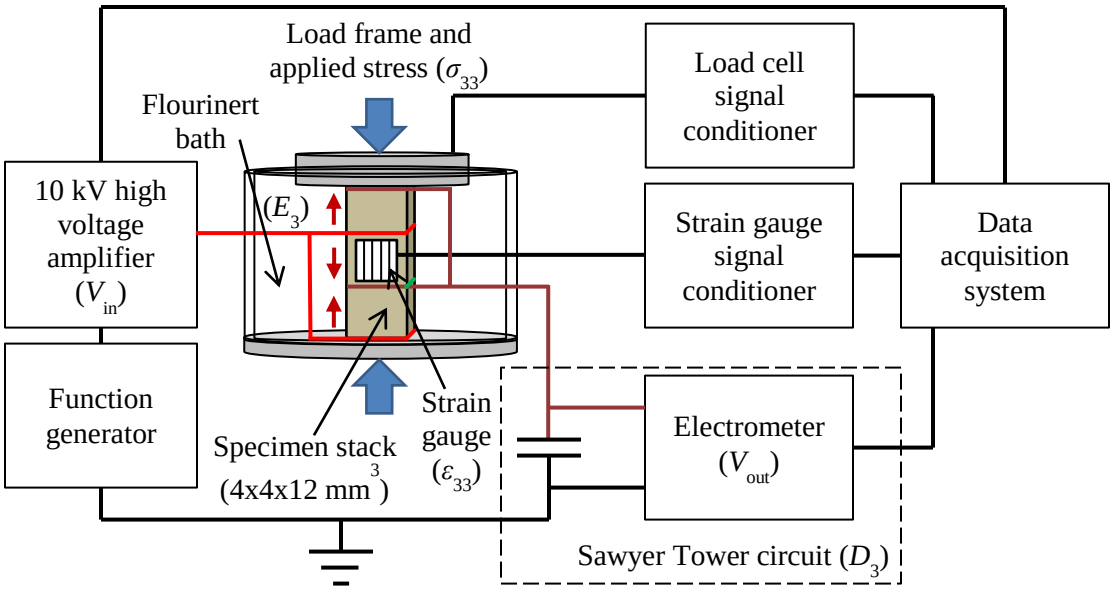

Figure 5-3. Experimental arrangement of the mechanical / electrical / thermal loading system for $[001]_C$ specimens.

The test sequence shown schematically in Figure 5-4 was used for all compositions. Electric field was first cycled linearly at a frequency of 0.2 Hz to 1.5 MV/m with zero preload stress. A compressive preload stress of -12 MPa was applied and held constant while electric field was again cycled to 1.5 MV/m. This was repeated at -24, -36, and -48 MPa. An additional electric field cycle was run after the maximum preload stress to repole the specimen. Compressive stress was then linearly cycled at a loading rate of 0.625 MPa/s to -48 MPa with zero bias electric field. The bias electric field was then applied in increments of 0.375 MV/m and held constant while stress was again cycled to -48 MPa. This was repeated for five bias electric fields: 0, 0.375, 0.75, 1.125, and 1.5 MV/m. The electrical and mechanical loading sequences were repeated at temperatures of 25°C, 35°C, 45°C, 55°C, and 65°C.

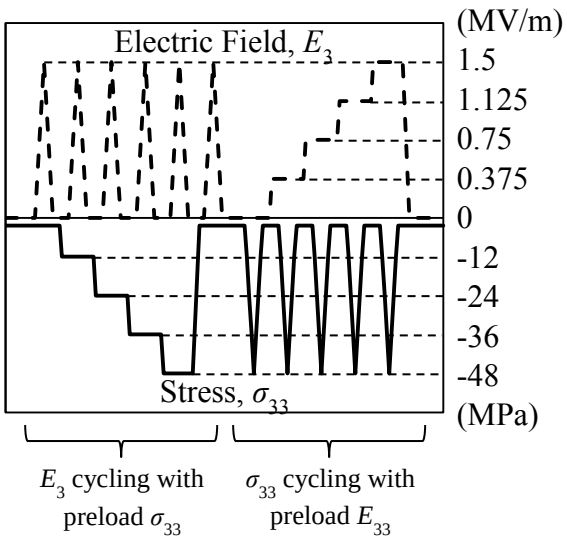

Figure 5-4. Experimental loading sequence that was repeated at temperatures of 25°C, 35°C, 45°C, 55°C, and 65°C.

5.3. Experimental Results

Experimental results shown in Figures 5-5 and 5-6 include (a) ε_{33}-E_3, (b) D_3-E_3, (c) ε_{33}-σ_{33}, and (d) D_3-σ_{33} curves at each temperature, compressive preload, and bias electric field for each of the six compositions. Figures 5-5 and 5-6 show the results for two of the compositions, 0.24PIN-0.48PMN-0.28PT and 0.24PIN-0.44PMN-0.32PT, at 25°C. The piezoelectric coefficient (d_{33}), dielectric permittivity (κ_{33}^{σ}), and compliance (s_{33}^{E}) of each composition were determined from the slopes of the linear FE_R and FE_O regions of each curve. The FE_R coefficients were determined from the slope of the curves at zero bias stress from 0 MV/m to 0.5 MV/m and at zero bias electric field from 0 MPa to -5 MPa. The FE_O coefficients were determined from the curves at maximum preload stress (-48 MPa) from 0 MV/m to 0.5 MV/m but only at temperatures where the material had been completely transformed by this stress level,

and from -43 MPa to -48 MPa at zero bias electric field. The temperature coefficients of the material properties ($\Delta d_{33}/\Delta T$, $\Delta \kappa_{33}^{\sigma}/\Delta T$, and $\Delta s_{33}^{E}/\Delta T$) were determined from the measured coefficients at the various temperatures. The thermal expansion (α_{33}) and pyroelectric (p_3) coefficients were determined from the changes in strain and electric displacement with temperature from 25°C to 65°C. The results for each composition are listed in Table 5-1 for 0.24 PIN concentration and Table 5-2 for 0.32 PIN concentration. Two data points were clear outliers and were omitted.

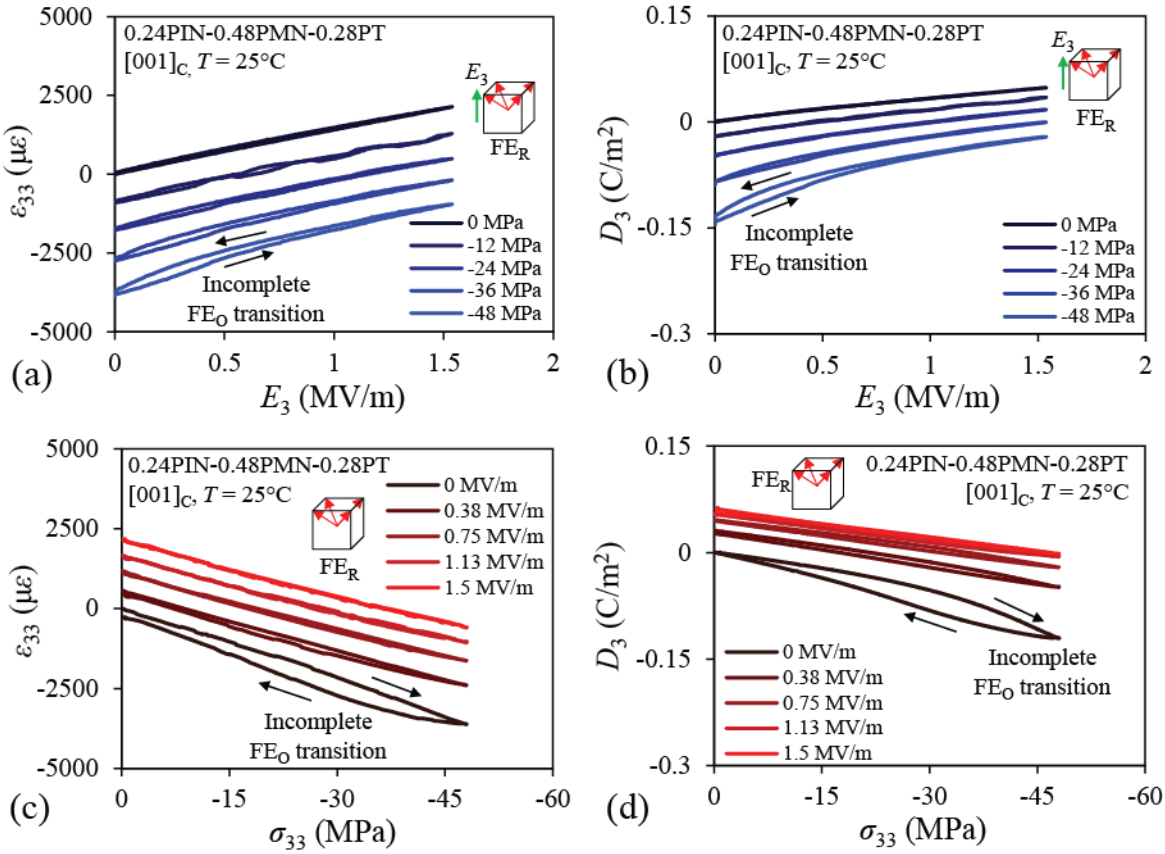

Figure 5-5: Behavior of $[001]_C$ 0.24PIN-0.48PMN-0.28PT at 25°C: (a) ε_{33}-E_3, (b) D_3-E_3, (c) ε_{33}-σ_{33}, and (d) D_3-σ_{33}. Although some non-linearity is apparent at the higher stress levels, the FE_R-FE_O transformation was incomplete. Arrows indicate the loading path direction.

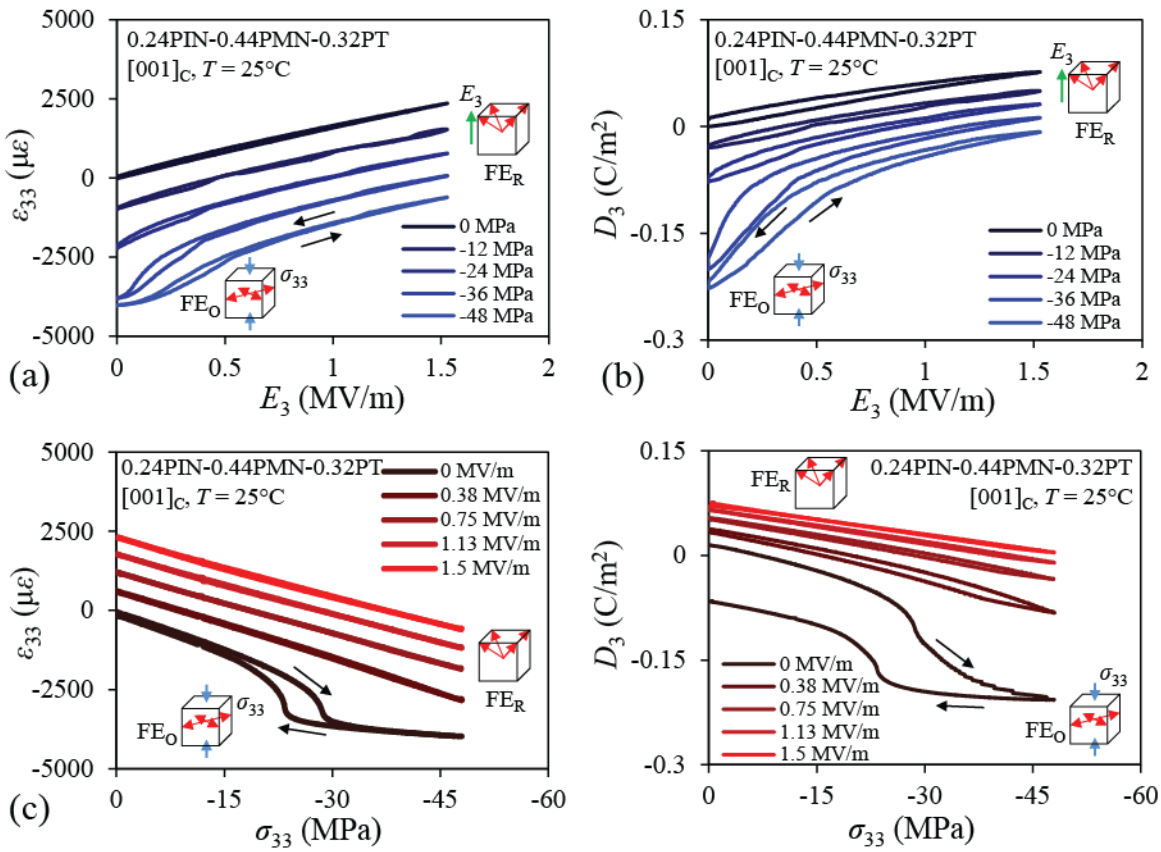

Figure 5-6: Behavior of $[001]_C$ 0.24PIN-0.44PMN-0.32PT at 25°C under mechanical and electrical loading: (a) ε_{33}-E_3, (b) D_3-E_3, (c) ε_{33}-σ_{33}, and (d) D_3-σ_{33}. The stress driven FE_R-FE_O transformation is apparent at zero electric field as the stress is increased in (c) and (d). The reverse transformation at a constant bias stress is seen in (a) and (b) when the bias is above the transformation threshold. Arrows indicate the loading path direction.

Table 5-1. Experimentally measured FE_R and FE_O material coefficients for each composition with 0.24 PIN concentration. There is little change in the material properties within a single phase with increasing bias field or stress preload.

Composition	Material Property	T (°C)	0.28 PT		0.30 PT		0.32 PT	
			FE_R	FE_O	FE_R	FE_O	FE_R	FE_O
0.24 PIN	Piezoelectric d_{33} (ε_{33}/E_3, pCN^{-1})	25	1400	--	1700	397	1690	416
		35	1590	--	1640	278	1706	415
		45	1899	--	1840	397	1850	425
		55	2080	--	1800	321	1920	419
		65	2430	338	1705	391	1870	221
		$\Delta d_{33}/\Delta T$	25.5	--	1.04	--	7.80	--
	Dielectric $\kappa_{33}^{\sigma}/\kappa_0$ (κ_0=8.855e^{-12} Fm^{-1})	25	4580	--	6280	--	5330	--
		35	5230	--	5750	--	5640	--
		45	6640	--	6330	--	7160	--
		55	6370	--	6520	--	6160	--
		65	5810	--	8140	--	8010	--
		$\Delta\kappa_{33}^{\sigma}/\Delta T$	36.0	--	52.5	--	58.8	--
	Compliance s_{33}^{E} (10^{-12} Pa^{-1})	25	70	--	75	21	76	16
		35	79	12	74	16	76	16
		45	89	12	73	21	83	14
		55	89	14	73	18	82	14
		65	88	15	76	14	84	13
		$\Delta s_{33}^{E}/\Delta T$	0.46	--	0.03	--	0.02	--
	Thermal expansion α_{33} ($\mu\varepsilon K^{-1}$)	--	-6.3	--	-7.2	--	-4.1	--
	Pyroelectric p_3 ($\mu Cm^{-2}K^{-1}$)	--	-414	--	-382	--	-314	--

Table 5-2. Experimentally measured FE_R and FE_O material coefficients for each composition with 0.32 PIN concentration. There is little change in the material properties within a single phase with increasing bias field or stress preload.

Composition	Material Property	T (°C)	0.28 PT		0.30 PT		0.32 PT	
			FE_R	FE_O	FE_R	FE_O	FE_R	FE_O
0.32 PIN	Piezoelectric d_{33} (ε_{33}/E_3, pCN^{-1})	25	1230	--	1620	--	1810	--
		35	1240	--	1720	--	1740	--
		45	1340	--	1770	--	1820	--
		55	1290	--	1990	--	1870	--
		65	1250	447	2200	457	--	--
		$\Delta d_{33}/\Delta T$	0.87	--	1.44	--	--	--
	Dielectric $\kappa_{33}^{\sigma}/\kappa_0$ (κ_0=8.855e^{-12} Fm^{-1})	25	4790	--	4940	--	5100	--
		35	4490	--	4710	--	6460	--
		45	5640	--	6010	--	7030	--
		55	5000	--	5580	--	7280	--
		65	6410	--	7280	--	--	--
		$\Delta\kappa_{33}^{\sigma}/\Delta T$	37.6	--	55.5	--	--	--
	Compliance s_{33}^{E} (10^{-12} Pa^{-1})	25	53	--	74	--	85	--
		35	52	--	85	--	--	--
		45	53	--	87	--	--	--
		55	54	19	95	17	--	--
		65	53	19	97	19	--	--
		$\Delta s_{33}^{E}/\Delta T$	0.02	--	0.56	--	--	--
	Thermal expansion α_{33} ($\mu\varepsilon K^{-1}$)	--	-8.4	--	-9.3	--	-6.7	--
	Pyroelectric p_3 ($\mu Cm^{-2}K^{-1}$)	--	-460	--	-453	--	-350	--

The two dimensional ε_{33}-E_3, D_3-E_3, ε_{33}-σ_{33}, and D_3-σ_{33} plots shown in Figures 5-5 and 5-6 are part of a four dimensional surface that can be represented using two three dimensional plots.

These three dimensional ε_{33}-σ_{33}-E_3 and D_3-σ_{33}-E_3 profiles give insight into the large field material behavior and are shown in Figures 5-7 and 5-8, respectively, for the specimens with 0.24 PIN composition. The reference electric displacement and strain (location of zero values on the plots) are the remanant polarization and remnant strain values of the FE_R phase. For this crystal cut the remanant polarization is 0.3 MV/m and the remanant strain is zero. The plotted values are the changes relative to the reference state.

The upper planar region is associated with the rhombohedral phase while the lower planar region that is beginning to appear at increased stress and low electric field is associated with the orthorhombic phase. The FE_R-FE_O transformation threshold is lower at higher PT concentrations and higher temperature. The nonlinear region between the two planar regions is associated with the field induced FE_R-FE_O phase transformation. The FE_R region has a much steeper slope than the FE_O region. The largest linear piezoelectric, dielectric, and compliance coefficients correspond to the FE_R region, but the overall largest coefficients occur during the phase transformation.

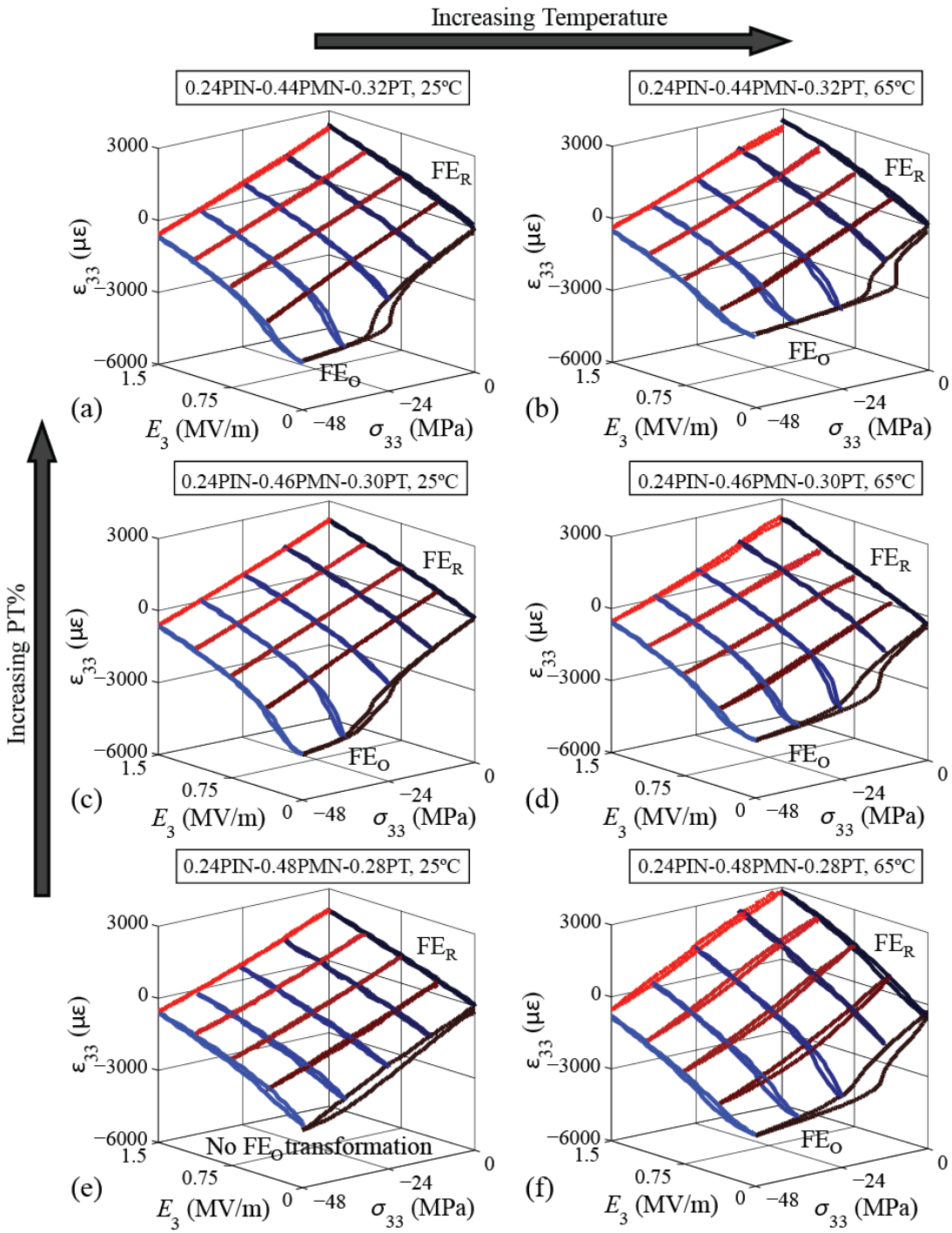

Figure 5-7. ε_{33}-σ_{33}-E_3 phase transformation profile for 0.24PIN-(1-0.24-*y*)PMN-*y*PT for (a) and (b) y = 0.32, (c) and (d) y = 0.30, and (e) and (f) y = 0.28, at (a), (c), and (e) 25°C and (b), (d), and (f) 65°C.

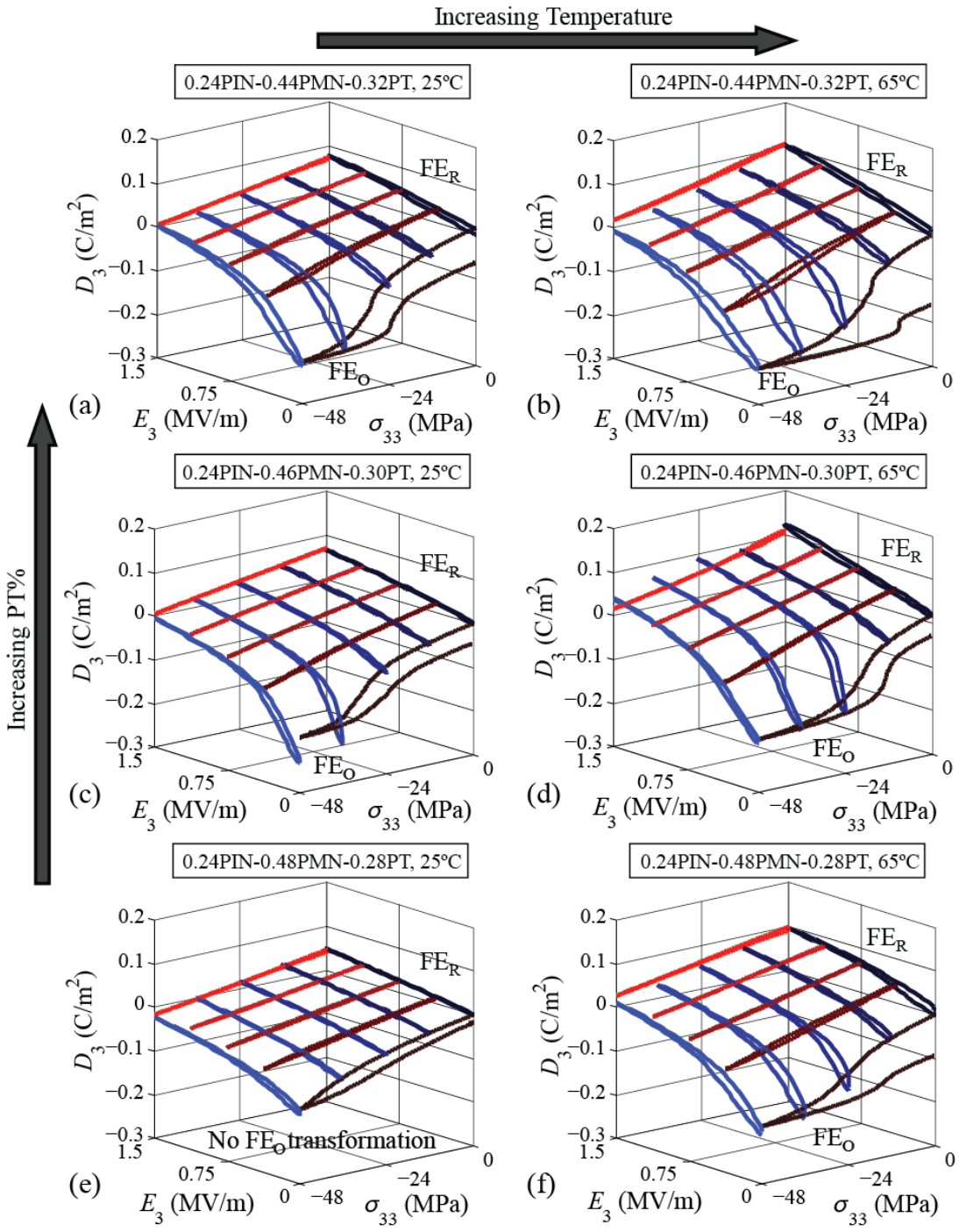

Figure 5-8. D_3-σ_{33}-E_3 phase transformation profile for 0.24PIN-(1-0.24-y)PMN-yPT for (a) and (b) y = 0.32, (c) and (d) y = 0.30, and (e) and (f) y = 0.28, at (a), (c), and (e) 25°C and (b), (d), and (f) 65°C.

5.4. Analysis and Discussion

The large reduction in remanent polarization of the zero-bias electric field stress cycles upon unloading the stress seen in Figure 5-8 (the stress loading paths that do not close) indicates mechanically induced depolarization of the specimens. When stress is applied in the $[001]_C$ direction the crystal is driven to the (4O) state where there is no net polarization. The spontaneous polarization of each domain is oriented perpendicular to the direction of applied stress. Releasing the stress results in the non-polar (8R) state unless there is a bias electric field present during unloading the stress that will return the specimen to the (4R) state.

Previously, McLaughlin et al. determined that the compliance of the secondary phase in domain engineered $[001]_C$ PMN-0.32PT closely matched the compliance of the FE_O phase in domain engineered $[011]_C$ PMN-0.32PT and was significantly smaller than the compliance of the FE_R phase [20]. Combined with the depolarization (near zero values for the dielectric coefficient) and the crystal cut and loading configuration they suggested that the depolarized secondary phase in the $[001]_C$ crystal was FE_O. As seen in Table 5-1 and Figure 5-7, there is a near order of magnitude decrease in the compliance between the initial phase and the secondary phase. Due to the similar crystal cut and loading configuration used in this study, it is assumed that the secondary phase of PIN-PMN-PT is FE_O as well.

In ferroelectric single crystals the mechanical and electrical thresholds required to induce the FE_R-FE_O transformation are linearly related [6]. This relation is a function of temperature. The minimum electric field threshold required for linear FE_R behavior of 0.24PIN-0.48PMN-0.28PT at each preload stress is plotted in Figure 5-9 for 25°C, 45°C, and 65°C. The other compositions show similar trends. There is a linear relationship between the preload stress and the minimum electric field required to achieve linear behavior. Increasing stress results in an

increase in the minimum E_3 for linearity. Increasing the temperature moves this E_3 threshold to higher amplitudes requiring larger applied electric fields to achieve linear FE_R behavior. A least squares fit of the linear E_3 threshold – σ_{33} preload resulted in equations for each composition at 25°C and 65°C. These are given in Table 5-3. These results indicate that linear response can be achieved for a given preload stress and temperature by driving the crystals about a bias electric field value and keeping the minimum electric field value above the minimum threshold for linear behavior.

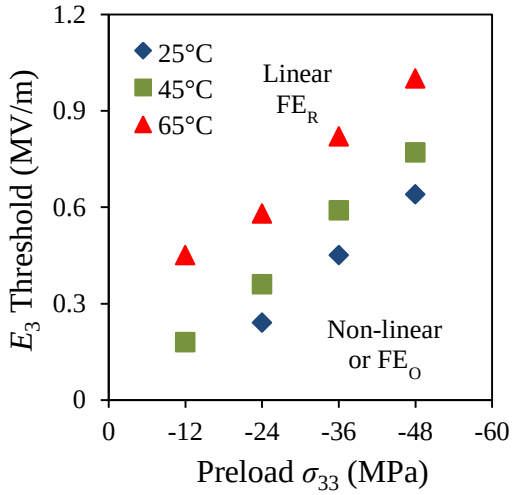

Figure 5-9. Electric field threshold for linear FE_R behavior with preload stress at each temperature for 0.24PIN-0.48PMN-0.28PT. The data point for 0 MPa preload at 65°C has been removed due to being an extreme outlier.

Table 5-3. Linear E_3-σ_{33} threshold equations at 25°C and 65°C. Data for 0.32PIN-0.36PMN-0.32PT at 65°C was not recorded.

Composition (PIN/PMN/PT)	Temperature	
	25°C	65°C
0.24/0.44/0.32	$E_3 = -0.015\sigma_{33} - 0.050$	$E_3 = -0.016\sigma_{33} + 0.250$
0.24/0.46/0.30	$E_3 = -0.012\sigma_{33} - 0.005$	$E_3 = -0.012\sigma_{33} + 0.210$
0.24/0.48/0.28	$E_3 = -0.017\sigma_{33} - 0.157$	$E_3 = -0.017\sigma_{33} + 0.240$
0.32/0.36/0.32	$E_3 = -0.016\sigma_{33} + 0.103$	--
0.32/0.38/0.30	$E_3 = -0.013\sigma_{33} + 0.053$	$E_3 = -0.013\sigma_{33} + 0.140$
0.32/0.40/0.28	$E_3 = -0.012\sigma_{33} + 0.035$	$E_3 = -0.014\sigma_{33} + 0.230$

When the forward and reverse transformation stress and electric field values are plotted as a function of temperature, the points are found to lie in a plane [20, 124]. The effect of PT concentration on this transformation threshold plane is shown in Figure 5-10. Points above this plane are in the linear FE_R regime. If a particular application requires linear FE_R behavior and a compressive bias stress, a bias electric field can be used to keep the material operating above the plane. The amount of bias field depends on the stress level, on the composition, and on the temperature. The data for the 0.24PIN-0.44PMN-0.32PT and 0.24PIN-0.48PMN-0.28PT compositions are plotted in Figure 5-10. Figure 5-10(a) shows the σ_{33}-T-E_3 threshold associated with linear FE_R behavior while Figure 5-10(b) is a rotated view of the same data showing that the data produce two nearly parallel planes for the two compositions. The other four compositions displayed similar behavior.

Equations were determined for these planes in stress, electric field, temperature space for each of the six compositions. A least squares multiple linear regression fit of the E_3 linear threshold for each σ_{33} preload and temperature resulted in planar equations for each composition. PIN-PMN-PT behavior is non-linear and hysteretic at applied electric fields below these planes.

The planar equations are given in Table 5-4. These results indicate that linear response can be achieved for a given preload stress and temperature by driving the crystals about a bias electric field value and keeping the minimum electric field value above the minimum threshold for linear behavior.

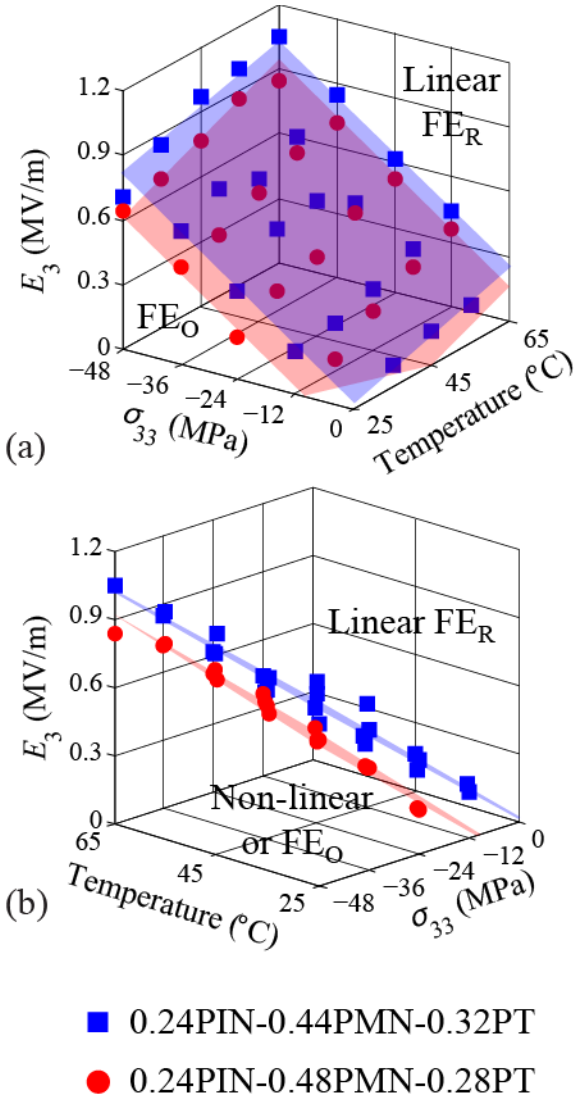

Figure 5-10. (a) Electric field threshold for linear FE_R behavior at different preload stresses and temperatures. Data is shown for 0.24PIN-0.44PMN-0.32PT (blue squares) and 0.24PIN-

0.48PMN-0.28PT (red circles). (b) The axes have been rotated to show the nearly parallel planes associated with linear FE_R behavior. The other compositions have similar behavior.

Table 5-4. E_3-σ_{33}-T equations for the plane separating linear behavior in the FE_R region from the onset of the FE_R-FE_O phase transformation. PIN-PMN-PT follows linear FE_R behavior when the applied electric field is larger than the given E_3 corresponding to a given bias stress and temperature. The behavior of PIN-PMN-PT is non-linear or FE_O at fields smaller than E_3.

Composition (PIN/PMN/PT)	Electric field amplitude for linear FE_R behavior ($x10^{-2}$)
0.24/0.44/0.32	$E_3 = -1.63\sigma_{33} + 0.564T - 12.1$
0.24/0.46/0.30	$E_3 = -1.39\sigma_{33} + 0.725T - 20.8$
0.24/0.48/0.28	$E_3 = -1.62\sigma_{33} + 0.746T - 34.8$
0.32/0.36/0.32	No data 35°C-65°C
0.32/0.38/0.30	$E_3 = -1.34\sigma_{33} + 0.479T - 4.94$
0.32/0.40/0.28	$E_3 = -1.20\sigma_{33} + 0.614T - 12.0$

5.5. Concluding Remarks

The large field strain (ε_{33}) and electric displacement (D_3) of $[001]_C$ cut d_{33}-mode FE_R PIN-PMN-PT crystals was experimentally characterized under mechanical and electrical loads at different temperatures for a range of compositions. Increasing temperature caused an increase in the linear FE_R material properties but also increased the minimum electric field bias required for linear behavior. Compositions with a larger linear response regime under combined stress, electric field, and temperature loading undergo a corresponding reduction in the piezoelectric, compliance, and dielectric coefficients. Decreasing temperature and decreasing PT concentration

in a manner that brings the composition away from the morphotropic phase boundary extends the FE_R linear regime. The effect of temperature is more pronounced for lower PIN concentrations.

When the crystals are subjected to a preload compressive bias stress, a bias electric field is required to obtain a linear response with minimal hysteresis. The minimum bias electric field increases when the crystals are under increased compressive stress preload or increased thermal loads. The trends suggest that if a particular application requires linear material behavior and a preload stress, the material selected should have a lower PT concentration. The trends suggest that a material of even lower PT content, perhaps 24% PT, with lower compliance, piezoelectric, and dielectric coefficients, would have an extended linear regime that may be beneficial to some applications.

CHAPTER 6

COMBINING EXPERIMENTS AND MODELING TO CHARACTERIZE FIELD DRIVEN PHASE TRANSFORMATION IN RELAXOR FERROELECTRIC SINGLE CRYSTALS

Field induced phase transformations in $[011]_C$ cut and poled relaxor ferroelectric single crystals can be induced by electrical or mechanical loading. Concurrent electrical and mechanical loading drives the ferroelectric rhombohedral to ferroelectric orthorhombic phase transformation at lower threshold levels than either load alone. The current experimental technique for characterization of the large field behavior including the phase transformation requires an extensive set of measurements performed under electric field cycling at different stress preloads and stress cycling at different bias electric fields repeated at multiple temperatures. Here, a mechanism based model is combined with a more limited set of experiments to obtain the same results. The model utilizes a work-energy criterion that calculates work required to induce the transformation by overcoming an energy barrier. In the relaxor single crystals, the energy barrier of phase transformations distributed over a range of field values is represented by a normal distribution of step like transformations. The results of the combined experiment / modeling approach are compared to the fully experimental approach and error is discussed.

Preliminary work was presented at the 2012 ASME Conference on Smart Materials Adaptive Structures and Intelligent Systems (SMASIS) in Stone Mountain, GA USA, and published in *Smart Materials and Structures* [125]. The results of this study have been submitted

to *Acta Materialia* [126]. Support for this work was provided by Progeny Systems through Navy SBIR Grant N00014-12-C-339.

6.1. Introduction

Relaxor ferroelectric single crystals exhibit many electromechanical properties superior to those of ferroelectric ceramics [12, 60, 61]. This has resulted in their use in applications that include advanced sonar and medical ultrasound transducers [1-5], energy harvesters [6], and as a platform to study the behavior of magnetoelectric heterostructures under biaxial strain loading [10, 11]. The electromechanical behavior is limited by electrical, mechanical, and thermally driven phase transitions [15-19]. Although this limits the linear behavior desired in acoustic transducer applications, it provides extraordinarily large changes of polarization and strain that are beneficial to the energy harvesting and magnetoelectric heterostructure applications.

The [001]c and [011]c cut and poled rhombohedral phase crystals are referred to as "domain engineered". Domain engineered crystals exhibit reduced hysteresis due to the near elimination of domain wall motion [12]. This results in a stress and electric field loading regime with linear behavior and very low loss. $[011]_C$ crystals are often mechanically pre-loaded with stress (σ_{22}) in the $[100]_C$ direction and unipolar electric field (E_3) in the $[011]_C$ direction. When this loading exceeds a transformation threshold, a field induced phase transformation from the ferroelectric rhombohedral phase (FE_R) to the ferroelectric orthorhombic phase (FE_O) occurs [68, 116, 117]. This phase transition results in non-linearity and hysteresis. The combined effects of σ_{22} and E_3 act cooperatively to drive the FE_R to FE_O phase transformation. Concurrent $[100]_C$

mechanical loading and $[011]_C$ electrical loading drive the FE_R-FE_O phase transformation at lower threshold levels than either load alone.

Figure 6-1 shows a schematic of the domain engineered state and the polarization reorientation associated with the FE_R-FE_O transformation in $[011]_C$ single crystals under electrical (Figure 6-1(b)) and mechanical (Figure 6-1(c)) loading. The observed effect of transformation is a jump in strain and electric displacement as well as a decrease in the compliance, piezoelectric, and dielectric coefficients by nearly an order of magnitude [16, 63]. The FE_R-FE_O phase transformation can display either a sharp discontinuous strain and electric displacement or a more gradual transition distributed over a range of applied field levels [63]. The relationship between the coordinate axes and the Miller indices used in the following discussion is also defined in Figure 6-1.

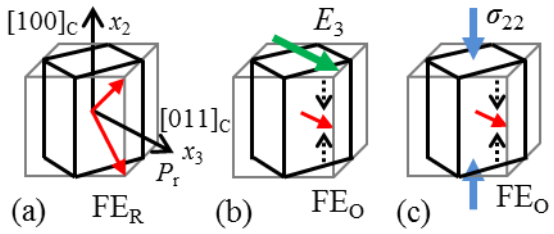

Figure 6-1: Polarization reorientation under loading for $[011]_C$ cut and poled relaxor ferroelectric single crystals. (a) At room temperature with no external loads the crystal is in a two variant rhombohedral state with volume average polarization (P_r) in $[011]_C$. Application of (b) electrical loads in $[011]_C$ and (c) mechanical loads in $[100]_C$ above the transformation threshold induce a FE_R-FE_O phase transformation to a single variant orthorhombic state with polarization in the $[011]_C$ direction.

Recent experimental characterization of $[011]_C$ ternary ferroelectric single crystal lead indium niobate – lead magnesium niobate – lead titanate, xPb($In_{1/2}Nb_{1/2}$)O_3-(1-x-y)Pb($Mg_{1/3}Nb_{2/3}$)O_3-$y$$PbTiO_3$ (xPIN-(1-x-y)PMN-yPT) provides examples of distributed and discontinuous transformation behavior. [113, 114]. Figure 6-2(a) shows the distributed strain – electric field (ε_{22}-E_3) transformation behavior of 0.24PIN-0.48PMN-0.28PT and Figure 6-2(b) shows the discontinuous transformation behavior of 0.24PIN-0.44PMN-0.32PT under electrical loading. The electric displacement – electric field (D_3-E_3), strain – stress (ε_{22}-σ_{22}) and electric displacement – stress (D_3-σ_{22}) curves display similar phase transformation profiles [113, 114].

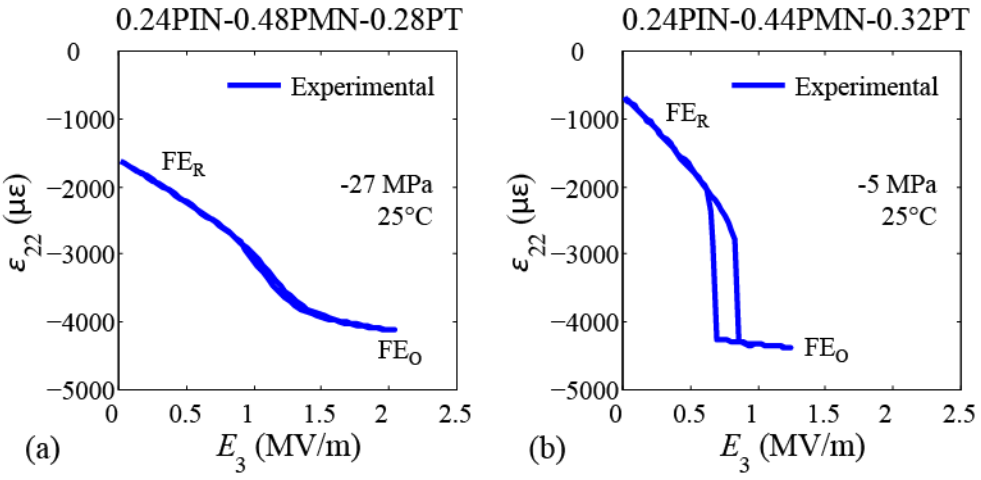

Figure 6-2: Examples of the effects of (a) a distributed phase transformation in 0.24PIN-0.48PMN-0.28PT and (b) a discontinuous phase transformation in 0.24PIN-0.44PMN-0.32PT on the ε_{22}-E_3 plots. The initial strain offset is associated with the preload stress and the compliance of the FE_R phase.

Modeling of the distributed field phase transformation is based on the observed behavior of relaxor ferroelectrics. Relaxor ferroelectrics display a phase transition when cooled from the

cubic phase that is distributed about a mean Curie temperature [62]. Chemical heterogeneity at the nanometer length scale is understood to be the origin of the broad Curie temperature region and frequency-dispersive properties of relaxor ferroelectrics [68, 69]. Hierarchical domain structures have been observed in single crystal lead magnesium niobate – lead titanate (1-*x*)$Pb(Mg_{1/3}Nb_{2/3})O_3$-*x*$PbTiO_3$ (PMN-*x*PT) with compositions close to the MPB. The domain sizes range from nanometers to millimeters and the spatial configuration of the domains is dependent on the thermal and electrical history of the specimen [127]. The material behavior and crystal structure are temperature dependent. At high temperatures the material is paraelectric. A transformation from paraelectric to the ergodic relaxor phase occurs when cooled below the Burns temperature. This cooling results in the development of nano polar regions associated with randomly distributed dipoles that give rise to enhanced dielectric and piezoelectric behavior [69]. Spontaneous polarization develops as temperature is reduced below the Curie temperature (T_C ~ 200°C for PIN-PMN-PT) and the material enters a ferroelectric phase. The morphotropic phase boundary that separates the rhombohedral phase from the tetragonal phase is tilted in the composition – temperature phase diagram. For compositions that are near this boundary and pass through it upon cooling, when the temperature is below the rhombohedral to tetragonal phase transformation temperature ($T_{R/T}$ ~ 137°C for PIN-PMN-PT), the ferroelectric tetragonal structure transforms to the FE_R structure [35, 36, 38-40] passing through a monoclinic phase.

Webber et al. [70] proposed a model based on the concept that spatial chemical and structural heterogeneities play a similar role in the distributed field-induced transformations in ferroelectric single crystals. They modeled the observed phase transformation behavior based on the volume average of the behavior of many small regions, with each region displaying an idealized discontinuous transformation. Fluctuations in the material properties about their mean

values were assumed to result in a distribution of transformation threshold fields that follow a normal distribution, with the center of the transformation defined in terms of a mean value and the spread in terms of the standard deviation. This led to simulations that closely matched experimental data. Similar models have been used in simulations of 180° domain switching [128].

The success of Webber's modeling approach suggested the possibility of greatly reducing the number of experiments necessary to fully characterize the field induced phase transformations as a function of stress, electric field, and temperature. Experimentally characterizing field induced phase transformations in relaxor single crystals requires using simultaneous combinations of stress, electric field, and temperature loading [15, 16, 18, 113]. This experimental characterization technique requires a mechanical load frame, a high voltage power supply, a strain gauge amplifier, a Sawyer Tower circuit (or equivalent method to measure the charge on the specimen), and a temperature controller. Electric field is cycled at multiple stress preloads and stress is cycled at multiple bias electric fields. This procedure is repeated at multiple temperatures. Details of the experimental procedure have been previously published [113]. The collection and analysis of this type of data is time consuming.

The following sub-sections describe a characterization approach that combines experiments with a modified modeling methodology. The model is validated through a comparison of a full set of measured stress, strain, electric displacement, and electric field plots to those generated from a single D_3-ε_{22}-E_3 measurement plus the compliance of the FE_R phase and the error is discussed.

6.2. Model Methodology

McLaughlin et al. [16] and Dong et al. [124] measured a scalar energy barrier to a field induced phase transformation. They showed that when a combination of mechanical and electrical loading that does positive work during the transformation is sufficient to overcome the energy barrier, the transformation takes place. The mechanical work density (w^{m}) is expressed in equation (6-1) as the integral of the ε-σ loading path and the electrical work density (w^{e}) is expressed in equation (6-2) as the integral of the *D*-*E* loading path,

$$w^{\mathrm{m}} = \int \sigma_{ij} \mathrm{d}\varepsilon_{ij} \tag{6-1}$$

and

$$w^{\mathrm{e}} = \int E_m \mathrm{d}D_m \,, \tag{6-2}$$

where σ_{ij} is the applied stress, E_m is the applied electric field, ε_{ij} is the strain, and D_m is the electric displacement. The indices vary from 1 to 3. For $[011]_{\mathrm{C}}$ crystals the only non-zero components of stress and electric field are σ_{22}, and E_3, and the resulting work conjugate variables are ε_{22}, and D_3. The energy barrier depends on temperature and composition and is assumed to be independent of loading path [113]. The energy barrier to the start of the transformation is taken to be equal to the work done (w^{C}) to start the transformation and can be determined by applying equation (6-3) along a measured data loading path,

$$w^{C} = \int_{0}^{\sigma_{ij}^{\text{R-O start}}} \sigma_{ij} \mathrm{d}\varepsilon_{ij} + \int_{0}^{E_{m}^{\text{R-O start}}} E_{m} \mathrm{d}D_{m} \,, \tag{6-3}$$

where $\sigma_{ij}^{\text{R-O start}}$ is the stress threshold corresponding to the start of the FE_R-FE_O transformation and $E_m^{\text{R-O start}}$ is the electric field threshold corresponding to the start of the FE_R-FE_O transformation. The mechanical and electrical loads required to induce a phase transformation have a linear relation, as shown in Figure 6-3. Equation (6-3) can be used to find the required work to begin the transformation, to drive the material part way through the transformation, or to complete the transformation.

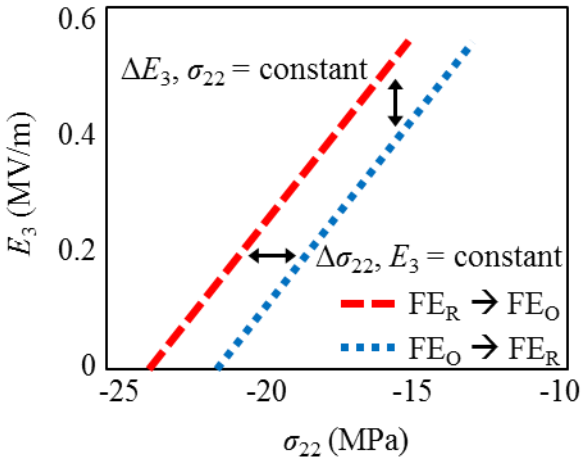

Figure 6-3. Stress and electric field driven phase transformation of PIN-PMN-PT single crystal showing hysteresis [6]. The long dashed line shows the combined forward loading criterion for the start of the FE_R-FE_O phase transformation to occur while the dotted line shows the combined reverse loading criterion for the start of the FE_O-FE_R phase transformation to occur. The horizontal arrow, $\Delta\sigma$, and vertical arrow, ΔE, denote the hysteresis between the forward and reverse mechanical and electrical loading paths at constant electric field and stress, respectively.

The model presented in this work requires ten input parameters, one made under mechanical loading and nine under electrical loading. The mechanical measurement (1) is of the compliance, s_{2222}^{E}. This measurement could also be made electrically by cutting and loading resonant bars. The nine inputs needed from the electric field cycle are shown schematically in Figure 6-4. Figure 6-4(a) shows (2) the start ($E_3^{\text{R-O start}}$) and (3) the finish ($E_3^{\text{R-O finish}}$) electric field thresholds of the transformation, (4) the transformation strain ($\Delta\varepsilon_{22}$), (5) the hysteresis width between the forward and reverse transformations (E_3^{hyst}), and (6) the piezoelectric (d_{322}) coefficient of the FE_R phase and (7) of the piezoelectric coefficient of the FE_O phase. Figure 6-4(b) shows (8) the transformation electric displacement (ΔD_3) and (9) the dielectric (κ_{33}^{σ}) coefficient of the FE_R phase and (10) the dielectric coefficient of the FE_O phase. The start and finish coercive fields are defined by a 5% change in slope from the linear FE_R or FE_O behavior, the hysteresis width is defined as the widest point between the forward and reverse electrical loading paths at zero stress, and the slopes were determined from the first 10% of the forward loading path (for the FE_R phase) and the first 10% of the unloading path after the peak amplitude was reached (for the FE_O phase). Minor hysteresis within the linear loading regime that has been shown to follow Rayleigh behavior is neglected in this model [129, 130].

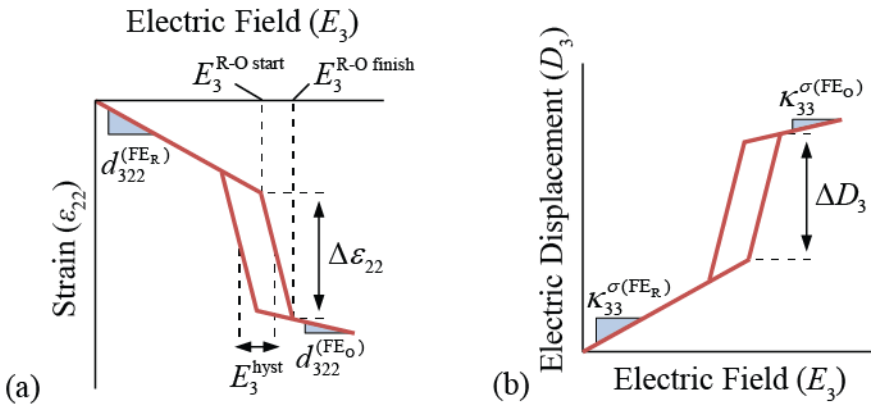

Figure 6-4: Inputs for the model from the electric field cycle through full transformation.

The procedure for constructing the curves that result from combined stress and electric field loading from the ten measured parameters is described next. The work required to reach the start of the FE_R-FE_O phase transformation was determined from electric field loading with zero preload stress using equation (6-4),

$$w^{\text{C}} = w^{\text{e, }(\sigma=0)} = \int_0^{E_3^{\text{R-O start, }(\sigma=0)}} E_3 \text{d}D_3 = \frac{1}{2} E_3^{\text{R-O start, }(\sigma=0)} D_3^{\text{R-O start, }(\sigma=0)} = \frac{1}{2} \kappa_{33}^{\sigma} \left(E_3^{\text{R-O start, }(\sigma=0)} \right)^2, \quad (6\text{-}4)$$

where w^e is the work due to electric field loading at zero stress and $E_3^{\text{R-O start, }(\sigma=0)}$ and $D_3^{\text{R-O start, }(\sigma=0)}$ are the electric field and electric displacement where transformation starts to occur at zero preload stress. This work is equal to the triangular area to the left of the D_3-E_3 curve shown in Figure 6-5(a) and could also be determined from numerical integration of the experimental data. With the measured compliance, the mechanical work (w^m) to reach the same threshold (w^c) with zero bias electric field is determined using equation (6-5),

$$w^{\mathrm{C}} = w^{\mathrm{m},\,(E=0)} = \int_0^{\sigma_{22}^{\text{R-O start, }(E=0)}} \sigma_{22}\mathrm{d}\varepsilon_{22} = \frac{1}{2}\sigma_{22}^{\text{R-O start, }(E=0)}\varepsilon_{22}^{\text{R-O start, }(E=0)} = \frac{1}{2}s_{2222}^{E}\left(\sigma_{22}^{\text{R-O start, }(E=0)}\right)^2. \quad (6\text{-}5)$$

$\sigma_{22}^{\text{R-O start, }(E=0)}$ and $\varepsilon_{22}^{\text{R-O start, }(E=0)}$ are the stress and strain thresholds when transformation starts to occur with zero bias electric field and s_{2222}^{E} is the measured mechanical compliance. This mechanical work corresponds to the area indicated in Figure 6-5(b). $\sigma_{22}^{\text{R-O start, }(E=0)}$ is thus determined using equation (6-6),

$$\sigma_{22}^{\text{R-O start, }(E=0)} = \left(\frac{2w^{\mathrm{C}}}{s_{2222}^{E}}\right)^{\frac{1}{2}}. \quad (6\text{-}6)$$

When the crystal is subjected to combined electrical and mechanical loading, the total work is the sum of the electrical and mechanical contributions, equation (6-7),

$$w^{\mathrm{C}} = w^{\mathrm{e}} + w^{\mathrm{m}}. \quad (6\text{-}7)$$

The same work based transformation criterion is used for concurrent electrical and mechanical loading. Figure 6-5(c) shows a schematic of the case of combined electrical and mechanical work. The sum of the two areas is equal to the energy barrier. This approach is used to determine the material response to electric field cycling at different stress preloads and to stress cycling at different electric field preloads.

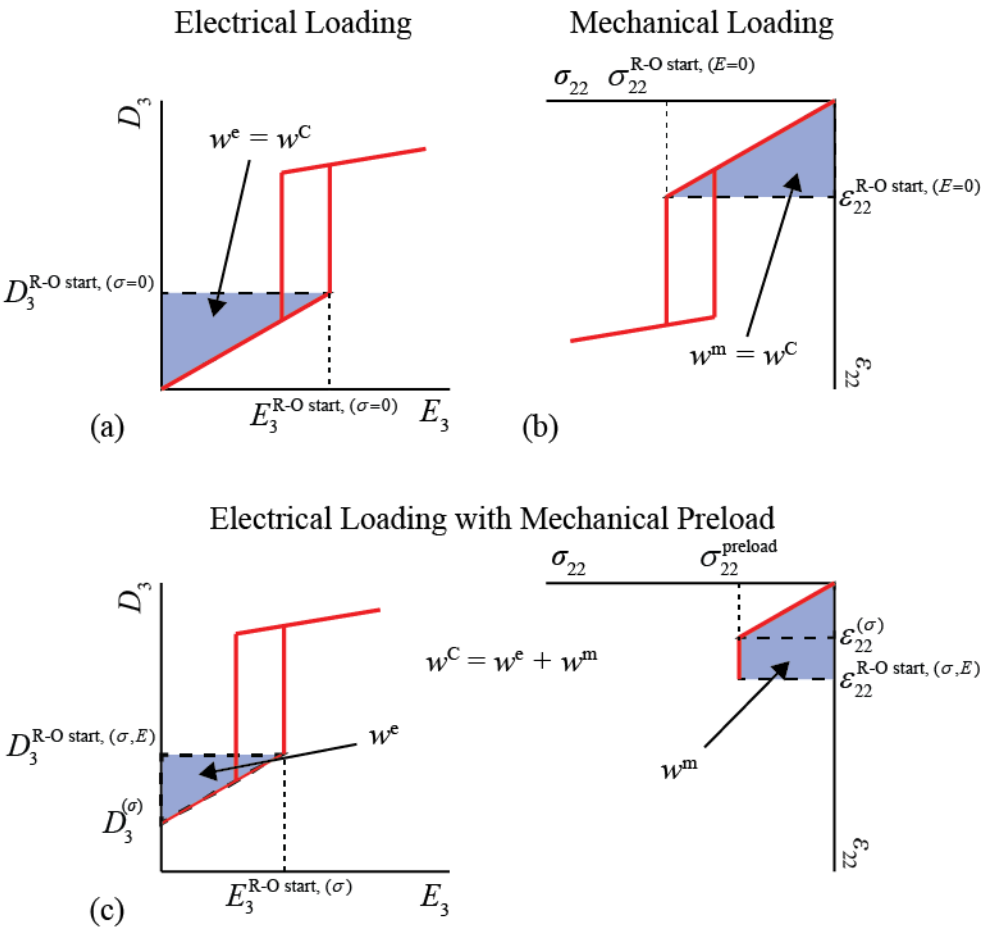

Figure 6-5: Work required to induce the FE_R-FE_O transformation. Work from (a) electrical loading, (b) mechanical loading, or (c) combined electrical and mechanical loading is constant regardless of loading path.

The use of this ten parameter model to predict the material response to loading along any path is described for the discontinuous transformation first. A full description of the material response under combined loading at a single temperature can be represented by a set of two 3D plots. The way these plots are constructed from the limited set of measurements is described with reference to Figure 6-6. The planes corresponding to the linear FE_R and FE_O regions are shown for (a) ε_{22}-σ_{22}-E_3 and (b) D_3-σ_{22}-E_3. The red curves represent the measured data. The curves on

the right hand side of each plot (D_3-E_3 and ε_{22}-E_3) are measured and the linear slope (compliance and piezoelectric coefficients) on the left side of Figures 6-6 (a) and (b) are measured as described above. The remaining portions of the curves on the left side are constructed as follows: The threshold stress for the transformation is calculated as described above. The strain jump associated with the transformation is obtained from the measured ε_{22}-E_3 curve on the right. The orthorhombic phase portion of the D_3-E_3 curve is extended back to zero-field. A line is constructed from that point to the strain value of the FEO phase determined by adding the strain jump to the strain determined from the compliance of the FE_R phase and the transformation stress. The slope of this line is the compliance of the orthorhombic phase. The unloading threshold stress is found from the D_3-E_3 measurement and the compliance of the FE_O phase. The FE_R and FE_O piezoelectric d_{322} coefficients of D_3-σ_{22} are calculated from the ε_{22}-E_3 curve. Other loading paths are determined once the electrical loading and mechanical loading paths are known. For combined mechanical and electrical loading, shown as the interior black dotted lines in Figure 6-6, when the material is subjected to a stress preload prior to electric field cycling (or a bias electric field prior to stress cycling) the preload mechanical (or electrical) work reduces the electrical (or mechanical) work required to induce transformation according to Equation (6-7).

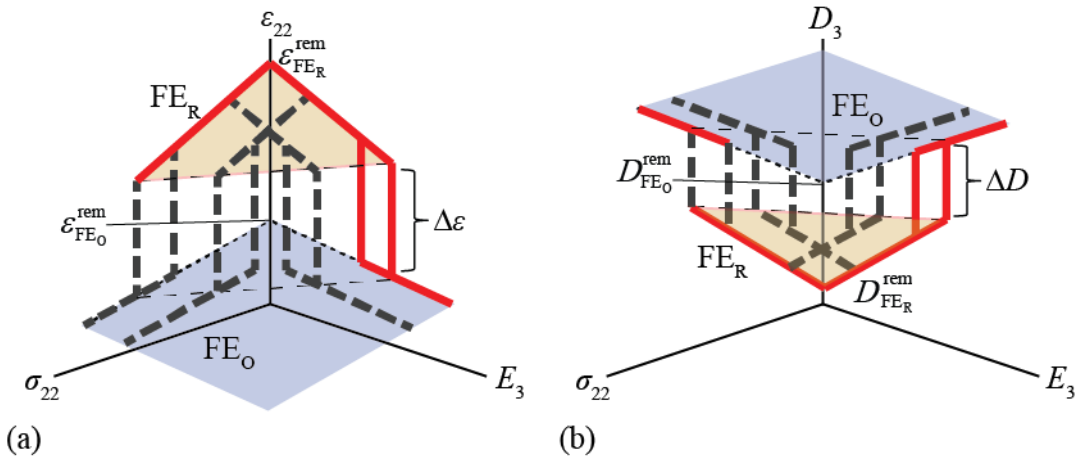

Figure 6-6: Construction of the (a) ε_{22}-σ_{22}-E_3 and (b) D_3-σ_{22}-E_3 loading paths for the discontinuous transformation. The initial planar region (low fields) is associated with the FE_R phase while the secondary planar region (large fields) is associated with the FE_O phase. The horizontal dotted lines represent the phase transformation thresholds.

The distributed phase transformation is modeled as a set of non-interacting discontinuous transformations with a normal distribution of transformation thresholds. This is based on an assumption that the distributed field induced phase transformation from the FE_R phase to the FE_O phase is governed by a mechanism similar to the spatially distributed chemical and structural heterogeneities that give rise to the diffuse Curie temperature observed in relaxor ferroelectrics [70]. The material is assumed to contain many small regions, each with a different transformation threshold. Each region is assumed to undergo an idealized discontinuous transformation between ferroelectric phases as shown in Figure 6-2(b). The result of this modeling approach is that increasing the applied field increases the volume fraction of the FE_O phase at the expense of the FE_R phase. This results in a smooth transition between phases when observed at the macroscopic scale.

The material constants of the FE_R phase are assumed to be the same for all of the untransformed regions while the material constants of the FE_O phase are assumed to be the same for all transformed regions. The transformation distribution functions for forward and reverse loading were assumed to be identical, but offset by the width of the phase transformation hysteresis loop. The normal distribution function is expressed by equation (6-8),

$$f(x) = \frac{1}{\sigma^{\text{std}}\sqrt{2\pi}} \exp\left[-\frac{1}{2}\left(\frac{x-\mu}{\sigma^{\text{std}}} \right)^2 \right], \tag{6-8}$$

where $f(x)$ represents a normal distribution of regions with an energy barrier to the start of the transformation given by $x = w^C$, where w^C is given by equation (6-7). In equation (6-8), σ^{std} is the standard deviation of the distribution of the energy barrier for each region to the start of the transformation and μ is the mean energy barrier of all of the regions to the start of the transformation. The start and finish of the distributed transformation were measured from a 5% slope change from linear. The energy barriers of the first and last regions to transform are determined using the values of $E_3^{\text{R-O start, }(\sigma=0)}$ corresponding to the start and finish of the distributed transformation and the linear permittivity of the FE_R phase with equations (6-4). These values were assigned to correspond to $\pm 2.58\sigma^{\text{std}}$ from the mean. The cumulative distribution function, $\Phi(x)$, is equal to the integral of f from zero to x. The integral over all x returns a value of one. The integral up to an intermediate value is used to represent the volume fraction of regions that have undergone the transformation.

The linear behavior of each region is described by equations (6-11) and (6-12),

$$\varepsilon_{22} = \varepsilon_{22}^{\mathrm{el}} + \varepsilon_{22}^{\mathrm{s}} = s_{2222}^{E}\sigma_{22} + d_{322}E_3 + \varepsilon_{22}^{\mathrm{s}} \tag{6-11}$$

and

$$D_3 = D_3^{\mathrm{el}} + D_3^{\mathrm{s}} = d_{322}\sigma_{22} + \kappa_{33}^{\sigma}E_3 + D_3^{\mathrm{s}}, \tag{6-12}$$

where ε_{22} and D_3 are the local strain and electric displacement, $\varepsilon_{22}^{\mathrm{el}}$ and D_3^{el} are the reversible strain and electric displacement, and $\varepsilon_{22}^{\mathrm{s}}$ and D_3^{s} are the spontaneous strain and electric displacement. s_{2222}^{E}, d_{322}, and κ_{33}^{σ} are the compliance, piezoelectric, and dielectric coefficients. The superscripts E and σ refer to coefficients measured at constant electric field and stress. The coefficients and the spontaneous values change when a transformation from the FE_R phase to the FE_O phase takes place. The volume average of the macroscale strain and electric displacement are determined using equations (6-13) and (6-14),

$$\hat{\varepsilon}_{22} = \left(1-\Phi\right)\varepsilon_{22}^{\mathrm{FE_R}} - \Phi\varepsilon_{22}^{\mathrm{FE_O}} \tag{6-13}$$

and

$$\hat{D}_3 = \left(1-\Phi\right)D_3^{\mathrm{FE_R}} - \Phi D_3^{\mathrm{FE_O}}. \tag{6-14}$$

$\hat{\varepsilon}_{22}$ and $\hat{D}_3$ are the volume average strain and electric displacement. Equations (6-13) and (6-14) were used to determine the material behavior when the crystal is in a partially transformed state where both the FE_R and FE_O phases are present.

When the total work done is higher than the energy barrier required to begin the transformation but lower than the energy barrier where the full transformation has taken place, the material is in a partially transformed state governed by equations (6-13) and (6-14). Unloading of the material from this partially transformed state requires the calculation of a new unloading path, defined by a different unloading normal distribution. The path associated with unloading a partially transformed volume is determined by multiplying the transformed volume fraction by the original hysteresis width of full transformation (if half of the material has transformed, then the hysteresis between the partially transformed forward and reverse loading paths is half of the hysteresis between the fully transformed forward and reverse loading paths). From the new hysteresis between paths, a new mean field is calculated for the reverse transformation, μ using equation (6-8), resulting in a new standard deviation for the reverse transformation, σ^{std} in equation (6-8).

6.3. Results

6.3.1. *Partial Phase Transformation Model*

To verify the partial transformation model and electric field cycle was run to 2.5 MV/m on a $[011]_C$ specimen of PMN-PT that displayed a distributed phase transformation. A second electric field cycle was then run to an amplitude of 1.75 MV/m, corresponding to completion of approximately 50% of the transformation. The model was then used to simulate the curve

corresponding to the full distributed transformation and the 50% transformation curve. Figure 6-7 displays the (a) experimental results and (b) a zoomed in image of the transformation region. Figure 6-8 shows the comparison between the experimental and simulated (a) full transformation and (b) partial transformation. The simulation closely matches the experimental data. The results for ε_{22}-E_3 are presented. The D_3-E_3 curve displays similar behavior. Although this method reproduces the partial transformation behavior in single crystals that display a distributed transformation, the remainder of this chapter is focused on the full transformation.

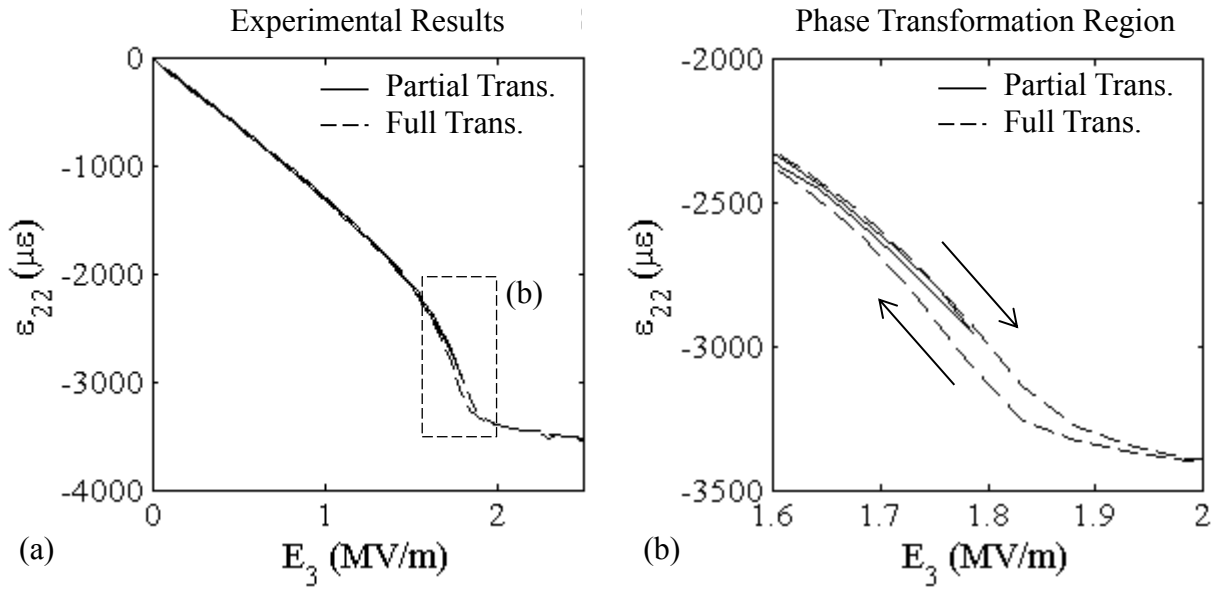

Figure 6-7: (a) Experimental strain response for electrically loaded PMN-PT through FE_R-FE_O phase transformation. (b) Expanded plot of the phase transformation region. The solid line shows the loading to 1.75 MV/m while the dotted line shows loading to 2.5 MV/m.

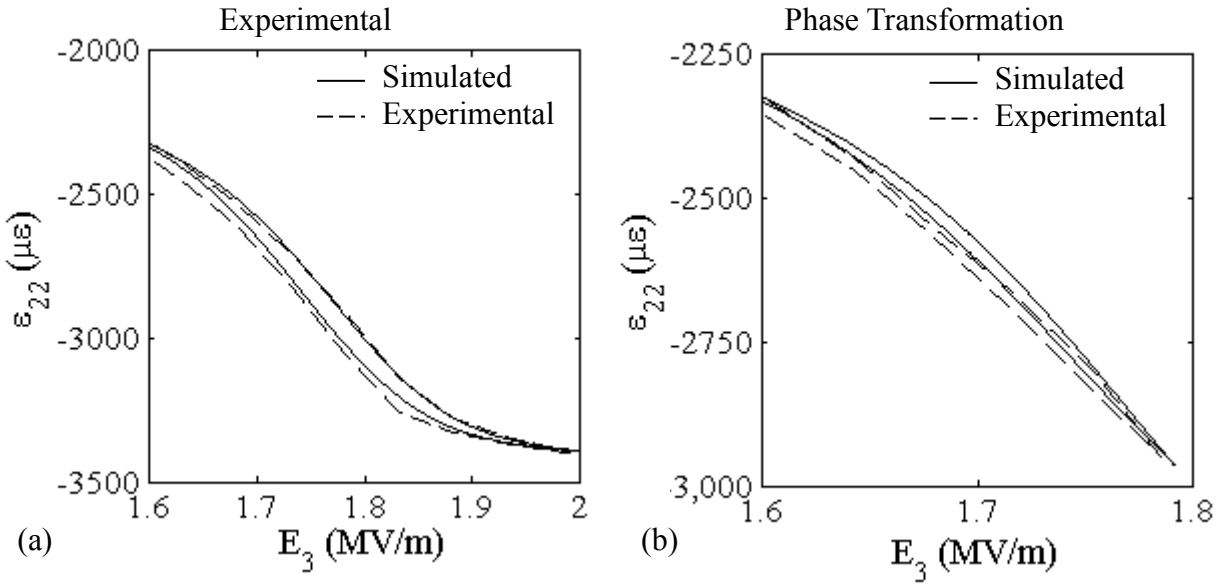

Figure 6-8: Simulated and experimental phase transformation behavior for (a) full FE_R-FE_O transformation and (b) partial transformation. The solid line shows the simulation and the dotted line shows the experimental results.

6.3.2. *Full Transformation Model*

$[011]_C$ cut and poled PIN-PMN-PT relaxor single crystal specimens were fully characterized as a function of stress, electric field, and temperature [113, 114]. To validate the model described above, the ten parameters were taken from the D_3-E_3 and ε_{22}-E_3 curves at zero stress and from the initial slope of the ε_{22}-σ_{22} curve. The model of the phase transformation was first validated for the electrical loading case by simulating both distributed and discontinuous transformations. The results are shown in Figure 6-9.

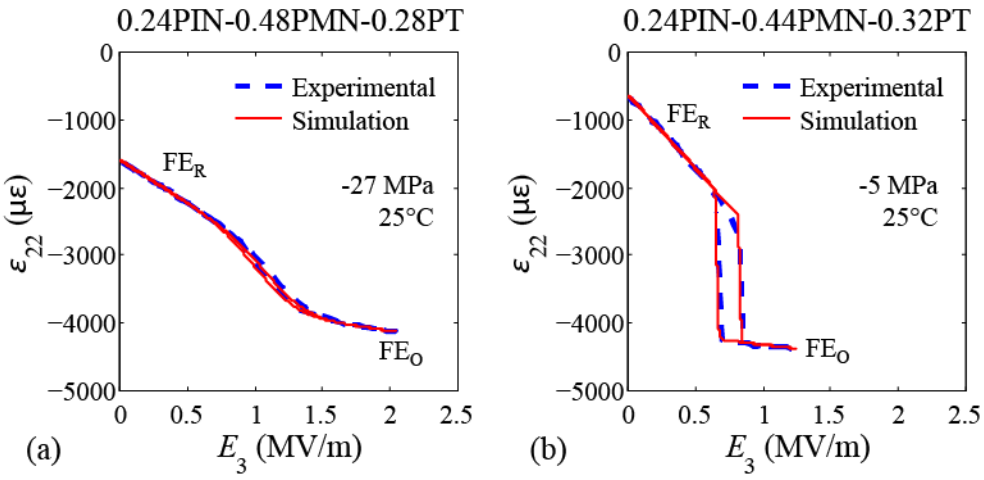

Figure 6-9: Comparison between the experimental and simulated field induced ε_{22}-E_3 phase transformation behavior for (a) distributed (0.24PIN-0.48PMN-0.28PT) and (b) discontinuous (0.24PIN-0.44PMN-0.32PT) type transformations.

In Figure 6-10 the experimentally determined data for 0.24PIN-0.46PMN-0.30PT at 65°C are shown in panes (a) and (b), and the data constructed from the zero stress D_3-E_3 curve and the zero field compliance in panes (c) and (d). Because the input to the model was taken from the electric field cycle at zero preload stress, the largest error between the simulated and experimental results occurs in the predicted ε_{22}-σ_{22} and D_3-σ_{22} curves. Figure 6-11 compares the simulated stress cycles when a bias electric field is present to the experimentally measured properties in the presence of a bias electric field for 0.24PIN-0.46PMN-0.30PT at 65°C.

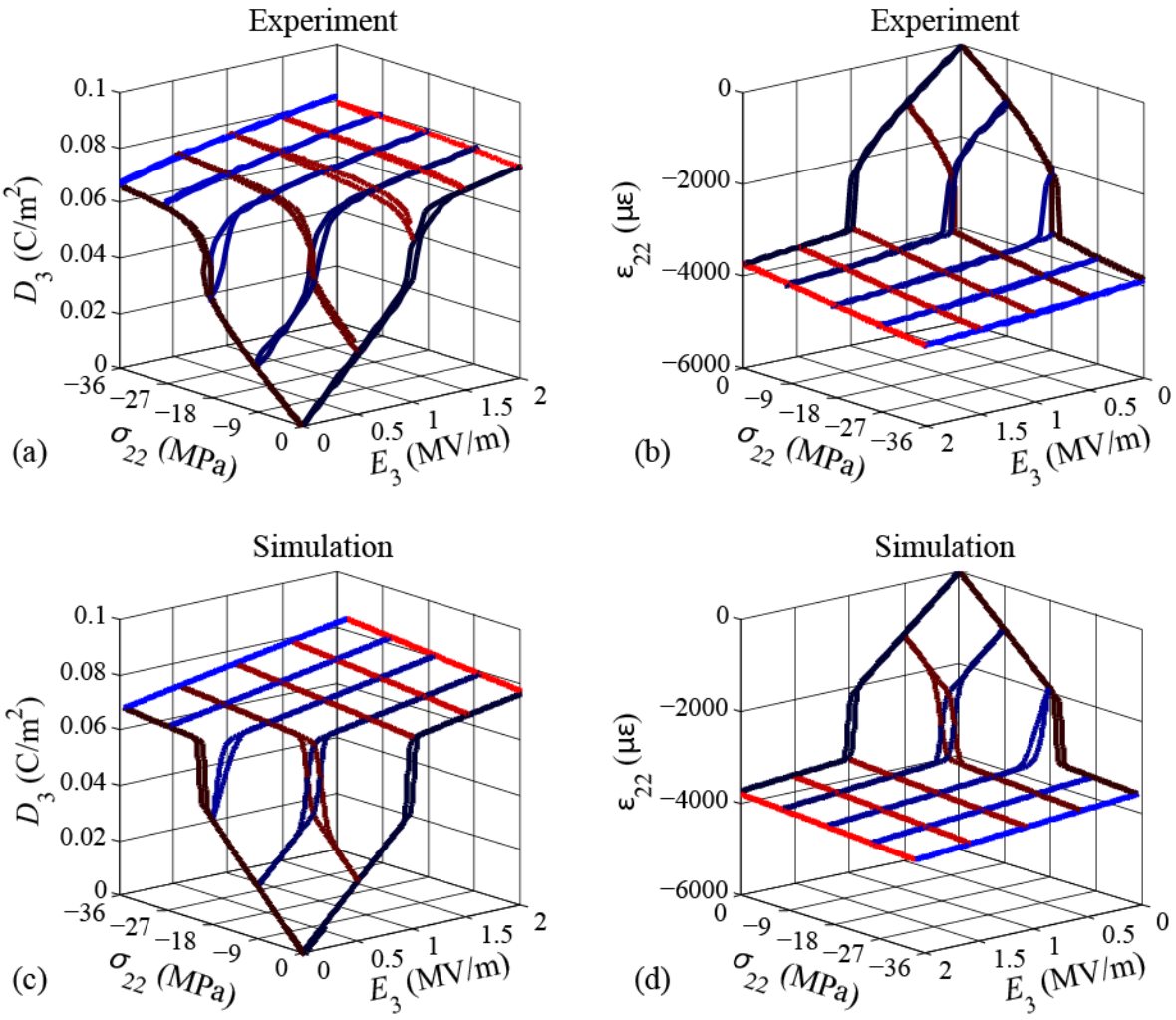

Figure 6-10: Experimentally measured (a) D_3 and (b) ε_{22}, and simulated (c) D_3 and (d) ε_{22}, under mechanical and electrical loads for 0.24PIN-0.46PMN-0.30PT at 65°C.

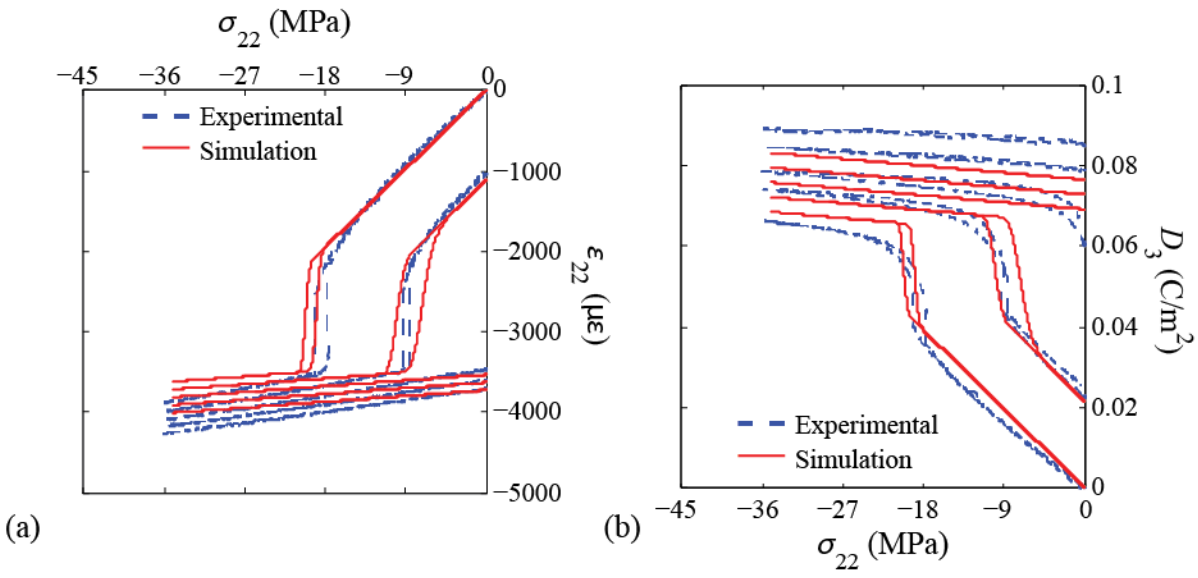

Figure 6-11: The largest error between the simulated and experimental results was for the (a) D_3-σ_{22} and (b) ε_{22}-σ_{22} curves. Data for 0.24PIN-0.46PMN-0.30PT at 65°C is shown.

6.4. Analysis and Discussion

Collection of the data shown in Figure 6-10 required extensive characterization work. The technique required equipment capable of simultaneously applying electrical, mechanical, and thermal loads while measuring the strain and electric displacement response in a controlled temperature environment. This required ten tests (an electric field cycle through the transformation at five preload stresses and a stress cycle through the transformation at five bias electric fields). The ten tests were repeated at 5 temperatures for a total of 50 measurements for a single composition. The approach based on more limited measurements and the model presented reduced the number and complexity of the experiments necessary for characterization of $[011]_C$, piezoelectric d_{32}-mode, relaxor ferroelectric single crystals to one electric field cycle through full transformation while measuring strain and electric displacement and one measurement of

compliance, repeated at each temperature. This eliminates the requirement for a load frame if the compliance is measured using a resonance method.

The largest source of error between the model and the experimental results is observed in the D_3-σ_{22} curves. The predicted portions of the stress driven curves are the entire D_3-σ_{22} loops and the transformation region and FE_O region of the ε_{22}-σ_{22} loops. As can be seen in Figure 6-11, the predicted ε_{22}-σ_{22} curves have the right shape through the transformation but the transformation thresholds under combined loading are slightly off. The difference between the predicted electric displacement and the measured electric displacement is larger. The source of this error is not clear. It could be that there is a difference in what is taking place in the material when loaded mechanically vs. electrically that is not captured by the model, or it could be measurement error in the electric displacement measurement.

The compliance of the FE_O phase was inferred and not directly measured. The experimentally measured FE_R compliance (s^E_{2222}) was directly determined from the measured ε_{22}-σ_{22} curve. This results in a difference between the simulated and experimental FE_O compliance. The piezoelectric FE_R and FE_O coefficients of the stress cycle were assumed to be equal to d_{322} calculated from the electric field cycle (ε_{22}/E_3). At 65°C these coefficients were nearly identical to the experimentally calculated results. However, the zero-stress electric displacement predicted using the measured d_{322} was significantly smaller than the experimental results as the bias electric field was increased. This error could be associated with drift in the charge measurement from the Sawyer Tower circuit that was used to measure the electric displacement when a constant electric field was applied prior to stress cycling, or it could be the result of the stress cycles having been run at a different loading rate than the electric field cycles. It is possible that the error in the measurements is larger than the error in the simulated data.

Figure 6-12 shows the difference (error) between the experimentally measured stress transformation threshold and the simulated stress transformation threshold for 0.24PIN-0.46PMN-0.30PT as a function of temperature. The data points show the experimental values while the error bar shows the predicted values. The simulation almost always predicted a larger stress transformation threshold than the experiment. The error was largest at 25°C and smallest at 65°C. Table 6-1 list the experimental stress threshold, simulated stress threshold, and the absolute error for four compositions: 0.24PIN-0.44PMN-0.32PT, 0.24PIN-0.46PMN-0.30PT, 0.32PIN-0.36PMN-0.32PT, and 0.32PIN-0.38PMN-0.30PT. The decreasing error with increasing temperature trend is consistent for all four compositions. The error was observed to increase slightly as the FE_R-FE_O transformation behavior changed from discontinuous (higher PT concentrations) to distributed (lower PT concentrations).

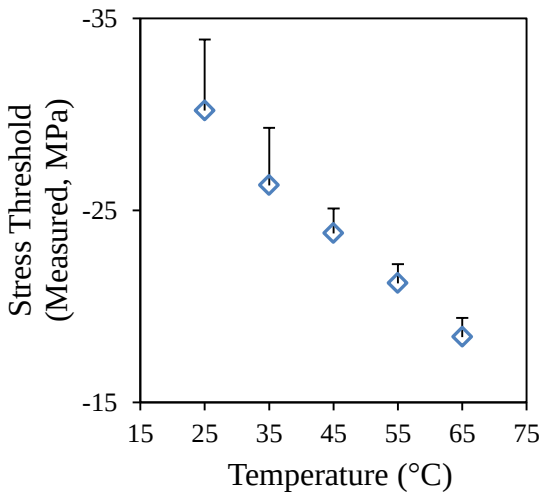

Figure 6-12: Stress threshold error for 0.24PIN-0.46PMN-0.30PT. The data points show the experimental values while the error bar shows the predicted stress threshold from the simulation.

Table 6-1: Stress threshold error for the four compositions (PIN/PMN/PT) that were simulated.

Composition (PIN/PMN/PT)	Temp (°C)	Experimental $\sigma^{\text{R-O start}}$ (MPa)	Simulated $\sigma^{\text{R-O start}}$ (MPa)	Absolute Error (MPa)
0.24/0.44/0.32	25	-18.3	-20.2	-1.9
	35	-16.0	-19.4	-3.4
	45	-13.6	-16.6	-3.0
	55	-11.1	-12.2	-1.1
	65	-9.3	-10.6	-1.3
0.24/0.46/0.30	25	-30.2	-33.9	-3.7
	35	-26.3	-29.3	-3.0
	45	-23.8	-25.1	-1.3
	55	-21.2	-22.2	-1.0
	65	-18.4	-19.4	-1.0
0.32/0.36/0.32	25	-26.6	-30.8	-4.2
	35	-23.2	-28.1	-4.9
	45	-21.4	-23.8	-2.4
	55	-19.3	-20.9	-1.6
	65	-15.1	-16.8	-1.7
0.32/0.38/0.30	25	--	--	--
	35	--	--	--
	45	-27.0	-30.5	-3.5
	55	-24.5	-28.4	-3.9
	65	-21.7	-25.5	-3.8

6.5. Concluding Remarks

A modified model of the FE_R to FE_O phase transformation was developed and used to predict the phase transformation behavior of $[011]_C$ relaxor single crystals under combined stress and electric field loading. The results were compared to measurements for four compositions of PIN-PMN-PT over a range of temperatures from 25°C to 65°C. The difference between the

measured and simulated stress threshold for transformation was found to be less than 5 MPa for all compositions at 25°C and the error decreased at higher temperatures. The fifty experiments that combine electrical, mechanical, and thermal loading required for full characterization of a relaxor ferroelectric single crystal at five temperatures were reduced to ten experiments that can be performed using entirely electrical loading. These were a measurement of the strain and electric displacement during electrical loading through full transformation, and a measurement of the mechanical compliance, repeated at five temperatures.

This characterization method based on a combination of a limited number of measurements and a mechanism based model provides a number of benefits. It offers a simplified means of verification of the behavior of individual pieces of as-received materials or a spot check of batches of material received by device manufacturers, and it offers a simplified approach to quality control by crystal producers. The elimination of a need to apply stress enables making measurements on smaller specimens. It also enables rapid characterization of new compositions, speeding the process of compositional development and characterization and allows for rapid screening of new compositions.

Several effects were left out of the model. Loading of PMN-xPT within the FE_R phase is known to result in minor hysteresis loops that can be described by Rayleigh behavior (a first order dependence of the material coefficients on field). The concept of inhomogeneities in relaxor ferroelectrics giving rise to a set of non-interacting regions with discontinuous type transformations with a normal distribution captures the behavior of the distributed transformation reasonably well, but the accuracy of the model could likely be improved by including a micromechanical representation of the interactions between the regions in a self-consistent scheme.

CHAPTER 7

SUMMARY

Relaxor ferroelectric single crystals are a key component of many applications that require electro-mechanical coupling and are used across a wide range of industries. New compositions are being studied and the piezoelectric and electromechanical properties are being tailored to fit the specific needs of individual applications. Recently binary and ternary compositions have been manufactured with the goal of increasing the thermal operating range and increasing hardening against mechanically and electrically driven phase transformations while maintaining the extraordinary piezoelectric properties. Phase transformations are being explored for use in energy harvesting applications but need to be avoided in acoustic transducer applications. Experimental characterization of the large field ferroelectric behavior of each composition under electrical, mechanical, and thermal loads is required for the design of devices for specific applications. Experimental characterization is a lengthy process requiring multiple experiments, specialized equipment, and precise analysis. The results of this research provide an improved understanding of the large field behavior and field induced phase transformations in relaxor ferroelectrics.

In this research the characterization procedures were discussed and experimental characterization and simulation of many ferroelectric materials was presented. In Chapter 3 a technique to calculate the large field dielectric loss (tan δ) in ferroelectric materials was developed. This procedure was then demonstrated for single crystal PMN-0.32PT, ceramic poly-crystal PLZT (8/65/35), and PZT-5A ferroelectric macro-fiber composite (MFC) with interdigitated electrodes (IDEs) under various electrical, mechanical, and thermal loading

conditions. Using the dielectric loss model it was found that the results for single crystal PMN-0.32PT could be collapsed into a single curve. Tan δ was found to increase substantially in PLZT 8/65/35 due to the change of shape of the minor hysteresis loops. However, at increased electric field amplitudes, all values of tan δ converged and behaved as the inverse of the loss energy ($1/L_e$). In the MFC with the IDE configuration, dielectric loss was found to be a result of ferroelastic switching due to the field gradients present between the IDEs. For all three studies, a discussion of dielectric loss was presented in terms of domain wall motion.

The experimental characterization of ferroelectric rhombohedral (FE_R) $[011]_C$ and $[001]_C$ PIN-PMN-PT single crystals with compositions near the morphotropic phase boundary (MPB) was presented in Chapters 4 and 5. The combined electrical, mechanical, and thermal loading techniques were presented and discussed. The effect of composition on the field induced phase transformations was determined. It was found that the piezoelectric and electromechanical coefficients increased as the PT concentration was increased towards the MPB. Increasing the PIN concentration reduced the coefficients. The phase transformation behavior has a strong dependence on composition. At lower PT concentrations the single crystals displayed a distributed transformation. Increasing the PT concentration to near the MPB caused the transformation to become discontinuous. This suggests that PIN-PMN-PT with lower PT concentrations might be advantageous due to the increased linear regime while PIN-PMN-PT with higher PT concentrations might be better utilized for energy harvesting applications.

The results of the experimental characterization were presented in terms of an energy barrier to the phase transformation, when non-linearity occurs in the strain and electric displacement behavior. Stress – electric field – temperature planes were determined which corresponded to the amplitudes required for transformation. In $[011]_C$ PIN-PMN-PT, at loading

amplitudes lower than the energy barrier the material behaves linearly. In $[001]_C$ PIN-PMN-PT, for a given stress and temperature the electric field must be greater than a certain value in order to maintain linear behavior. Composition and temperature were found to significantly affect the phase transformation behavior and the energy barrier to these transformations.

A new approach to characterizing the large field behavior of relaxor ferroelectric single crystals was developed in Chapter 6. This approach is based on a combination of a work-energy based model of the driving forces for the phase transformation together with electric field loading while monitoring strain and electric displacement, and a measurement of mechanical compliance. The model was used in Chapter 6 and verified using the experimental characterization results of PIN-PMN-PT presented in Chapters 4 and 5. Using this combination of a mechanism based model with limited experiments provides a number of benefits. It offers a simplified means of verification of the behavior of individual pieces of as-received materials or a spot check of batches of material received by device manufacturers. It also offers a simplified approach to quality control for crystal producers. The model enables rapid characterization of new compositions, speeding the process of development and characterization. The elimination of a need to apply stress enables making measurements on smaller specimens.

Analysis of the experimental characterization assumed a FE_R-FE_O phase transformation based on the change in the material coefficients and the orientation of the mechanical and electrical loads. Verification of the FE_O phase was not conducted. This would require the development of a procedure to experimentally measurement the domain orientation under large applied electrical and mechanical loads.

While the model was developed and verified for $[011]_C$ materials, careful consideration must be taken into account when using similar models on other crystal cuts. $[011]_C$ and $[001]_C$

single crystals are domain engineered to have stable domain walls resulting in limited hysteresis in the linear behavior. In other ferroelectric materials mechanical and electrical loading can cause domain wall motion, inreasing the hysteresis and associated energy dissipation. The energy barrier used in the model may be affected by this increased loss. In the future, as phase field models progress and coefficients are determined for relaxor ferroelectrics, the energwilbutretics of domain formation, phase boundary motion, and material heterogeneities are anticipated to become better understood and contribute considerably to improving models like the one developed in this work.

REFERENCES

1. Uchino, K., in *Proceedings of the 4th International Conference on Electronic Ceramics and Applications*. 1994: Aachen, Germany.
2. Uchino, K., *Piezoelectric Actuators and Ultrasonic Motors*. 1996, New York: Springer-Verlag.
3. Park, S.E. and Shrout, T.R., *Characteristics of relaxor-based piezoelectric single crystals for ultrasonic transducers.* IEEE Transactions on Ultrasonics Ferroelectrics and Frequency Control, 1997. **44**(5): 1140-1147.
4. Kobayashi, T., et al., *Improved growth of large lead zinc niobate titanate piezoelectric single crystals for medical ultrasonic transducers.* Japanese Journal of Applied Physics, Part 1 (Regular Papers, Short Notes & Review Papers), 1997. **36**(9B): 6035-6038.
5. Shrout, T.R., et al., *Innovations in piezoelectric materials for ultrasound transducers.* Proceedings of the SPIE - The International Society for Optical Engineering, 1998. **3341**: 174-183.
6. Dong, W.D., et al., *Giant electro-mechanical energy conversion in 011 cut ferroelectric single crystals.* Applied Physics Letters, 2012. **100**(4).
7. Aldrich, J.B., et al. *Design of passive piezoelectric damping for space structures*. in *SPIE, Smart Structures and Materials*. 1993. Albuquerque, NM.
8. Wilbur, M.L. and Wilkie, W.K., *Active-Twist Rotor Control Applications for UAVs*. in *24th Army Science Conference*. 2004. Orlando, FL.
9. Mulcahey, B. and Spangler, R.L., *Piezos tame tough vibrations.* Machine Design, 1998. **70**(4): 60-63.

10. Wu, T., et al., *Giant electric-field-induced reversible and permanent magnetization reorientation on magnetoelectric Ni/(011) [Pb(Mg1/3Nb2/3)O3](1−x)–[PbTiO3]x heterostructure.* Applied Physics Letters, 2011. **98**(1).

11. Liu, M., et al., *Voltage-Impulse-Induced Non-Volatile Ferroelastic Switching of Ferromagnetic Resonance for Reconfigurable Magnetoelectric Microwave Devices.* Advanced Materials, 2013. **25**(35): 4886-4892.

12. Park, S.E. and Shrout, T.R., *Ultrahigh strain and piezoelectric behavior in relaxor based ferroelectric single crystals.* Journal of Applied Physics, 1997. **82**(4): 1804-1811.

13. Kuwata, J., et al., *Dielectric Losses in Bi12GeO20 Single Crystals.* Japanese Journal of Applied Physics, 1981. **20**(8): 1609-1610.

14. Ujiie, R. and Uchino, K., *Dynamical domain observation in relaxor ferroelectrics.* IEEE 1990 Ultrasonics Symposium Proceedings (Cat. No.90CH2938-9), 1990: 725-8 vol.28 vol.2.

15. Lynch, C.S., *The effect of uniaxial stress on the electro-mechanical response of 8/65/35 PLZT.* Acta Materialia, 1996. **44**(10): 4137-4148.

16. McLaughlin, E.A., et al., *Relaxor ferroelectric PMN-32%PT crystals under stress and electric field loading: I-32 mode measurements.* Acta Materialia, 2004. **52**(13): 3849-3857.

17. Viehland, D., et al., *Piezoelectric instability in < 011 >-oriented Pb((B1/3B2/3II)-BI)O3-PbTiO3 crystals.* Applied Physics Letters, 2001. **79**(7): 1006-1008.

18. Viehland, D., *Effect of uniaxial stress upon the electromechanical properties of various piezoelectric ceramics and single crystals.* Journal of the American Ceramic Society, 2006. **89**(3): 775-785.

19. Zhao, X.Y., et al., *Dielectric and piezoelectric performance of PMN-PT single crystals with compositions around the MPB: influence of composition, poling field and crystal orientation.* Materials Science and Engineering B-Solid State Materials for Advanced Technology, 2002. **96**(3): 254-262.

20. McLaughlin, E.A., et al., *Relaxor ferroelectric PMN-32%PT crystals under stress, electric field and temperature loading: II-33-mode measurements.* Acta Materialia, 2005. **53**(14): 4001-4008.

21. Liu, T., et al., *Thermodynamics of stress and electric field induced phase transition in relaxor ferroelectric crystals.* Journal of Intelligent Material Systems and Structures, 2007. **18**(4): 409-415.

22. Curie, J. and Curie, P., *Development by Pressure of Polar Electricity in Hemihedral Crystals with Inclined Faces.* Comptes Rendus (France), 1880. **91**: 294-295.

23. Lippman, G., Ann. Chim. Phys., 1881. **24**.

24. Curie, J. and Curie, P., *Contractions et dilations produites par des tensions electriques dans les cristaux hemiedres a faces inclinees.* Comptes Rendus (France), 1881. **93**: 1137-1140.

25. Langevin, M.P., *Procede et appareils d'emission et de reception des ondes elastiques sous-marines a l'aide des proprietes piezo-electriques du quartz.* Brevet francais, 1918. **505703**: 538-542.

26. Valasek, J., *Piezo-Electric and Allied Phenomena in Rochelle Salt.* Physical Review, 1921. **17**(4): 475-481.

27. von Hippel, A., et al., *High dielectric constant ceramics.* Industrial & Engineering Chemistry, 1946. **38**(11): 1097-1109.

28. Wul, B.M. and Goldman, I.M., *Dielectric constants of titanates of metals of the second group.* Dokl. Akad. Nauk SSSR, 1945. **46**: 154-157.

29. Jaffe, B., et al., *Properties of piezoelectric ceramics in the solid-solution series lead titanate-lead zirconate-lead oxide: Tin oxide and lead titanate-lead hafnate.* J. Res. Natl. Bur. Stand., 1955. **55**(5): 239-254.

30. Crawford, A.E., *Lead zirconate-titanate piezoelectric ceramics.* British Journal of Applied Physics, 1961. **12**(10): 529.

31. Moulson, A.J. and Herbert, J.M., *Electroceramics: materials, properties, applications*. 1990, London; New York: Chapman and Hall.

32. Jaffe, B., et al., *Piezoelectric ceramics*. 1971, London and New York: Academic Press. 562-563.

33. Zhang, S., et al., *Elastic, Piezoelectric, and Dielectric Properties of 0.71Pb(Mg1/3Nb2/3)O3–0.29PbTiO3 Crystals Obtained by Solid-State Crystal Growth.* Journal of the American Ceramic Society, 2008. **91**(2): 683-686.

34. Cao, W.W., ed. *Full-set material properties and domain engineering principles of ferroelectric single crystals*. Handbook of Advanced Dielectric, Piezoelectric and Ferroelectric Materials - Synthesis, Characterization and Applications, ed. Ye, Z.G., 2008, Woodhead: Cambridge, England. 266-303.

35. Zhang, S., et al., *Characterization of Pb(In1/2Nb1/2)O3-Pb(Mg1/3Nb2/3)O3-PbTiO3 ferroelectric crystal with enhanced phase transition temperatures.* Journal of Applied Physics, 2008. **104**(6): 064106.

36. Zhang, S.J. and Li, F., *High performance ferroelectric relaxor-PbTiO3 single crystals: Status and perspective.* Journal of Applied Physics, 2012. **111**(3).

37. Hosono, Y., et al., *Dielectric and piezoelectric properties of Pb(In1/2Nb1/2)O3-Pb(Mg1/3Nb2/3)O3-PbTiO3 ternary ceramic materials near the morphotropic phase boundary.* Japanese Journal of Applied Physics, Part 1 (Regular Papers, Short Notes & Review Papers), 2003. **42**(2A): 535-538.

38. Liu, X., et al., *Complete set of material constants of Pb(In1/2Nb1/2)O3-Pb(Mg1/3Nb2/3)O3-PbTiO3 single crystal with morphotropic phase boundary composition.* Journal of Applied Physics, 2009. **106**(7): 074112-4.

39. Tian, J., et al., *Growth and improved properties of ternary piezoelectric single crystals in lead indium niobate-lead magnesium niobate-lead titanate system*, in *Ultrasonics Symposium (IUS), 2009 IEEE International*. 2009. 972-975.

40. Tian, J., et al., *Improved stability for piezoelectric crystals grown in the lead indium niobate--lead magnesium niobate--lead titanate system.* Applied Physics Letters, 2007. **91**(22): 222903-3.

41. Xu, G., et al., *Growth and electrical properties of large size Pb(In1/2Nb1/2)O3-Pb(Mg1/3Nb2/3)O3-PbTiO3 crystals prepared by the vertical Bridgman technique.* Applied Physics Letters, 2007. **90**(3): 032901-3.

42. Hosono, Y., et al., *Growth of single crystals of high-Curie-temperature Pb(In1/2Nb1/2)O3-Pb(Mg1/3Nb2/3)O3-PbTiO3 ternary systems near morphotropic phase boundary.* Japanese Journal of Applied Physics Part 1-Regular Papers Short Notes & Review Papers, 2003. **42**(9A): 5681-5686.

43. Hosono, Y., et al., *Crystal growth of Pb(In1/2Nb1/2)O3-Pb(Mg1/3Nb2/3)O3-PbTiO3 and Pb(Sc1/2Nb1/2)O3-Pb(Mg1/3Nb2/3)O3-PbTiO3 piezoelectric single crystals using*

the solution Bridgman method. Japanese Journal of Applied Physics, Part 1 (Regular Papers, Short Notes & Review Papers), 2003. **42**(9B): 6062-6067.

44. Chen, J., et al., *Ultra-wideband surface acoustic wave resonator employing Pb(In1/2Nb1/2)O-3-Pb(Mg1/3Nb2/3)O3-PbTiO3 crystals.* Applied Physics Letters, 2012. **100**(2).

45. Luo, J., et al. *Elastic, piezoelectric and dielectric properties of PIN-PMN-PT crystals grown by Bridgman method*. in *Ultrasonics Symposium, 2008. IUS 2008. IEEE*. 2008.

46. Yu, P., et al., *Growth and pyroelectric properties of high Curie temperature relaxor-based ferroelectric Pb(In1/2Nb1/2)O3-Pb(Mg1/3Nb2/3)O3-PbTiO3 ternary single crystal.* Applied Physics Letters, 2008. **92**(25): 252907-3.

47. Barsoum, M.W., *Fundamentals of Ceramics*. 1997: McGraw-Hill.

48. Lines, M.E. and Glass, A.M. , *Principles and Application of Ferroelectrics and Related Materials*. 1977, Oxford: Clarendon.

49. Uchino, K., *Ferroelectric Devices*. 2009, New York: CRC.

50. Cross, L.E., ed. *Ferroelectric ceramics: Tailoring properties for specific applications*. Ferroelectric Ceramics: Tutorial Reviews, Theory, Processing and Applications, ed. N. Setter and E.L. Colla. 1993, Birkhauser: Basel. 1-87.

51. Cohen, R.E. and Krakauer, H., *Lattice dynamics and origin of ferroelectricity in BaTiO3: Linearized-augmented-plane-wave total-energy calculations.* Physical Review B, 1990. **42**(10): 6416-6423.

52. Cohen, R.E., *Origin of ferroelectricity in perovskite oxides.* Nature, 1992. **358**(6382): 136-138.

53. Yin, J., et al., *Elastic, piezoelectric, and dielectric properties of 0.955Pb(Zn1/3Nb2/3)O3-0.45PbTiO3 single crystal with designed multidomains.* Ultrasonics, Ferroelectrics and Frequency Control, IEEE Transactions on, 2000. **47**(1): 285-291.

54. Zhang, R., et al., *Elastic, piezoelectric, and dielectric properties of multidomain 0.67Pb(Mg1/3Nb2/3)O3-0.33PbTiO3 single crystals.* Journal of Applied Physics, 2001. **90**(7): 3471-3475.

55. Oates, W.S., *Fracture of Ferroelectric Materials*, in *Mechanical Engineering*. 2004, Georgia Institute of Technology.

56. Yang, W. and Chen, L.Q., *Computer-simulation of the dynamics of 180-degrees ferroelectric domains.* Journal of the American Ceramic Society, 1995. **78**(9): 2554-2556.

57. Vanderbilt, D. and Cohen, M.H., *Monoclinic and triclinic phases in higher-order Devonshire theory.* Physical Review B (Condensed Matter and Materials Physics), 2001. **63**(9): 094108/1-094108/9.

58. Dong, W.D., et al., *A finite element based phase field model for ferroelectric domain evolution.* Smart Materials and Structures, 2012. **21**(9): 094014.

59. Devonshire, A.F., *Theory of Ferroelectrics.* Advances in Physics, 1954. **3**(10): 85-130.

60. Kuwata, J., et al., *Phase transitions in the Pb (Zn1/3Nb2/3)O3-PbTiO3 system.* Ferroelectrics, 1981. **37**(1): 579-582.

61. Kuwata, J., et al., *Dielectric and Piezoelectric Properties of 0.91Pb(Zn1/3Nb2/3)O3-0.09PbTiO3 Single Crystals.* Japanese Journal of Applied Physics, 1982. **21**(9).

62. Smolenskii, G.A., *Physical phenomena in ferroelectrics with diffused phase transitions.* J. Phys. Soc. Jpn. (Suppl.), 1970. **28**: 26-37.

63. Liu, T. and Lynch, C.S., *Ferroelectric properties of [110], [001] and [111] poled relaxor single crystals: measurements and modeling.* Acta Materialia, 2003. **51**(2): 407-416.

64. Uchino, K. and Hirose, S., *Loss mechanisms in piezoelectrics: how to measure different losses separately.* Ultrasonics, Ferroelectrics and Frequency Control, IEEE Transactions on, 2001. **48**(1): 307-321.

65. Uchino, K., et al., *Loss mechanisms and high power piezoelectrics.* Journal of Materials Science, 2006. **41**(1): 217-228.

66. Härdtl, K.H., *Electrical and mechanical losses in ferroelectric ceramics.* Ceramics International, 1982. **8**(4): 121-127.

67. Jiang Yu, L. and Dan, L., *On ferroelectric crystals with engineered domain configurations.* Journal of the Mechanics and Physics of Solids, 2004. **52**(8): 1719-1742.

68. Cross, L.E., *Relaxor ferroelectrics: an overview.* Ferroelectrics, 1994. **151**(1-4): 305-20.

69. Bokov, A.A. and Ye, Z.G., *Recent progress in relaxor ferroelectrics with perovskite structure.* Journal of Materials Science, 2006. **41**(1): 31-52.

70. Webber, K.G., et al., *A distributed step-like switching model of the continuous field-driven phase transformations observed in PMN-xPT relaxor ferroelectric single crystals.* Acta Materialia, 2008. **56**(12): 2744-2749.

71. Shrout, T.R., et al., *Dielectric behavior of single crystals near the (1-x)Pb(Mg1/3Nb2/3)O3-(x)PbTiO3 morphotropic phase boundary.* Ferroelectrics Letters Section, 1990. **12**(3): 63-69.

72. Zhang, S. and Shrout, T., *Relaxor-PT single crystals: observations and developments.* IEEE transactions on ultrasonics, ferroelectrics, and frequency control, 2010. **57**(10): 2138-2146.

73. Liu, T.Q. and Lynch, C.S., *Orientation dependence of nonlinearity and hysteresis in PZN-4.5%PT single crystals I: Unipolar response.* Journal of Intelligent Material Systems and Structures, 2006. **17**(11): 953-957.

74. Liu, T.Q. and Lynch, C.S., *Orientation dependence of nonlinearity and hysteresis in PZN-4.5%PT single crystals II: Bipolar electromechanical response.* Journal of Intelligent Material Systems and Structures, 2006. **17**(10): 931-937.

75. Finkel, P., et al., *Study of phase transitions in ternary lead indium niobate-lead magnesium niobate-lead titanate relaxor ferroelectric morphotropic single crystals.* Applied Physics Letters, 2010. **97**(12): 122903-3.

76. Finkel, P., et al., *Large strain transduction utilizing phase transition in relaxor-ferroelectric Pb(In1/2Nb1/2)O3-Pb(Mg1/3Nb2/3)O3-PbTiO3 single crystals.* Applied Physics Letters, 2011. **98**(19): 192902-3.

77. Gallagher, J.A., et al., *Effect of field driven phase transformations on the loss tangent of relaxor ferroelectric single crystals.* Journal of Applied Physics, 2013. **113**(8).

78. Gallagher, J.A., et al., *Large-field dielectric loss in relaxor ferroelectric PLZT.* Smart Materials and Structures, 2014. **23**(3): p. 6.

79. Gallagher, J.A., et al., *Stress and electric field gradient contributions to dielectric loss in ferroelectrics with interdigitated electrodes.* Journal of Intelligent Material Systems and Structures, 2014.

80. Hom, C.L. and Shankar, N., *Finite element modeling of multilayered electrostrictive actuators.* Proceedings of the SPIE - The International Society for Optical Engineering, 1995. **2442**: 376-385.

81. de Silva, C.W., *Damping*, in *Vibration: Fundamentals and Practice*. 2000, CRC Press: Boca Raton.

82. Ji, K.H., et al., *Semi-empirical modeling of hysteresis compensation in magnetostrictive actuator.* 2013: 86890.

83. Haertling, G., *PLZT electrooptic materials and applications - a review.* Ferroelectrics, 1987. **75**: 25-55.

84. Cao, H., et al., *Crystal orientation dependence of dielectric and piezoelectric properties of tetragonal Pb(Mg1/3Nb2/3)O3–38%PbTiO3 single crystal.* Materials Research Bulletin, 2002. **37**(13): 2135-2143.

85. Trivijitkasem, S. and Koyvanich, K., *Characterization of lead lanthanum zirconate titanate (PLZT) ceramics sintered at various temperatures.* Kasetsart J. (Nat. Sci.), 2007. **41**: 192-197.

86. Haertling, G.H. and Land, C.E., *Hot-pressed (Pb,La)(Zr,Ti)O3 ferroelectric ceramics for electrooptic applications.* Journal of the American Ceramic Society, 1971. **54**(1): 1-11.

87. Burns, G. and Dacol, F.H., *Crystalline ferroelectrics with glassy polarization behavior.* Physical Review B, 1983. **28**(5): 2527-2530.

88. Marqués, M.I. and Aragó, C., *Microscopic model for the formation of nanodomains in relaxor materials.* Physical Review B, 2010. **81**(6): 064114.

89. Viehland, D., et al., *Origin of F spots and stress sensitivity in lantanum lead-zirconate-titanate.* Journal of Applied Physics, 1993. **74**(12): 7454-7460.

90. Viehland, D., et al., *Internal strain relaxation and the glassy behavior of La-modified lead zirconate titanate relaxors.* Journal of Applied Physics, 1991. **69**(9): 6595-6602.

91. Darlington, C.N.W., *On the changes in structure of PLZT (8.7/65/35) between 80 and 750 K.* Physica Status Solidi A, 1989. **113**(1): 63-69.

92. Akbas, M.A., et al., *Domain structure-property relations in lead lanthanum zirconate titanate ceramics.* Journal of Materials Research, 1996. **11**(09): 2293-2301.

93. Mohiddon, M.A. and Yadav, K.L., *Effect of Fe doping on dielectric, ferroelectric and pyroelectric properties of PLZT (8/65/35).* Journal of Physics D-Applied Physics, 2007. **40**(23): 7540-7547.

94. Rauls, M.B., et al., *The effect of temperature on the large field electromechanical response of relaxor ferroelectric 8/65/35 PLZT.* Acta Materialia, 2011. **59**(7): 2713-2722.

95. Jonker, G.H., *Nature of aging in ferroelectric ceramics.* Journal of the American Ceramic Society, 1972. **55**(1): 57.

96. Seon-Bae, K., et al., *Comparison of MEMS PZT Cantilevers Based on d31 and d33 Modes for Vibration Energy Harvesting.* Microelectromechanical Systems, Journal of, 2013. **22**(1): 26-33.

97. Sodano, H.A., et al., *Comparison of piezoelectric energy harvesting devices for recharging batteries.* Journal of Intelligent Material Systems and Structures, 2005. **16**(10): 799-807.

98. Song, H.J., et al., *Energy Harvesting Devices Using Macro-fiber Composite Materials.* Journal of Intelligent Material Systems and Structures, 2010. **21**(6): 647-658.

99. Sodano, H.A., et al., *An investigation into the performance of macro-fiber composites for sensing and structural vibration applications.* Mechanical Systems and Signal Processing, 2004. **18**(3): 683-697.

100. Zhao, P., et al., *Piezoelectric strain sensor/actuator rosettes.* Smart Materials and Structures, 2011. **20**(10).

101. Kawiecki, G. and Jesse, S., *Rosette piezotransducers for damage detection.* Smart Materials and Structures, 2002. **11**(2): 196-201.

102. Matt, H.M. and di Scalea, F.L., *Macro-fiber composite piezoelectric rosettes for acoustic source location in complex structures.* Smart Materials and Structures, 2007. **16**(4): 1489-1499.

103. Salamone, S., et al., *High-velocity impact location on aircraft panels using macro-fiber composite piezoelectric rosettes.* Journal of Intelligent Material Systems and Structures, 2010. **21**(9): 887-896.

104. Cutchen, J.T., *PLZT Thermal-Flash Protective Goggles - Device Concepts and Constraints.* Ferroelectrics, 1980. **27**(1-4): 173-178.

105. Hagood, N.W., et al. *Improving transverse actuation of piezoceramics using interdigitated surface electrodes*. 1993.

106. Bent, A.A., et al., *Anisotropic actuation with piezoelectric fiber composites.* Journal of Intelligent Material Systems and Structures, 1995. **6**(3): 338-349.

107. Gaudenzi, P., *On the electromechanical response of active composite materials with piezoelectric inclusions.* Computers & Structures, 1997. **65**(2): 157-168.

108. Wilkie, W.K., et al., *Low-cost piezocomposite actuator for structural control applications.* Proceedings of the SPIE - The International Society for Optical Engineering, 2000. **3991**: 323-334.

109. Beckert, W. and Kreher, W.S., *Modelling piezoelectric modules with interdigitated electrode structures.* Computational Materials Science, 2003. **26**: 36-45.

110. Bowen, C.R., et al., *Optimisation of interdigitated electrodes for piezoelectric actuators and active fibre composites.* Journal of Electroceramics, 2006. **16**(4): 263-269.

111. Chen, W. and Lynch, C.S., *Finite element analysis of cracks in ferroelectric ceramic materials.* Engineering Fracture Mechanics, 1999. **64**(5): 539-562.

112. Hwang, S.C., et al., *Ferroelectric/ferroelastic interactions and a polarization switching model.* Acta Metallurgica Et Materialia, 1995. **43**(5): 2073-2084.

113. Gallagher, J.A., et al., *Compositional Dependence of Field Induced Phase Transformation in [011]C PIN-PMN-PT Relaxor Ferroelectric Single Crystals with d32 Piezoelectric Mode.* Acta Materialia, Accepted: June, 2014.

114. Gallagher, J.A., et al., *Effects of composition and temperature on the large field behavior of [011]C relaxor single crystals.* Applied Physics Letters, Submitted: May, 2014.

115. Sun, E., et al., *Elastic, dielectric, and piezoelectric constants of Pb(In1/2Nb1/2)O3–Pb(Mg1/3Nb2/3)O3–PbTiO3 single crystal poled along [011]c.* Applied Physics Letters, 2010. **97**(3):.

116. Viehland, D. and Powers, J., *Effect of uniaxial stress on the electromechanical properties of 0.7Pb(Mg1/3Nb2/3)O3-0.3PbTiO3 crystals and ceramics.* Journal of Applied Physics, 2001. **89**(3): 1820-1825.

117. Viehland, D. and Li, J.F., *Anhysteretic field-induced rhombhohedral to orthorhombic transformation in <110>-oriented 0.7Pb(Mg1/3Nb2/3)O-3-0.3PbTiO3 crystals.* Journal of Applied Physics, 2002. **92**(12): 7690-7692.

118. Lu, Y., et al., *Phase transitional behavior and piezoelectric properties of the orthorhombic phase of Pb(Mg(1/3)Nb(2/3))O(3)-PbTiO(3) single crystals.* Applied Physics Letters, 2001. **78**(20): 3109-3111.

119. Gallagher, J.A., et al., *Compositional dependence of electro-mechanical proerties and field induced phase transformations in [001]C PIN-PMN-PT single crystals.* Smart Materials and Structures, Accepted: July, 2014.

120. Gallagher, J.A., et al., *Effects of composition and temperature on the large field behavior of [001]C relaxor single crystals.* IEEE - TUFFC, Submitted: April, 2014.

121. Luo, J., et al., *The progress update of relaxor piezoelectric single crystals*, in *Ultrasonics Symposium (IUS), 2009 IEEE International*. 2009. 968-971.

122. Davis, M., et al., *Electric-field-, temperature-, and stress-induced phase transitions in relaxor ferroelectric single crystals.* Physical Review B, 2006. **73**(1): 014115.

123. Li, Q., et al., *In-situ neutron diffraction study of Pb(In1/2Nb1/2)O3-Pb(Mg1/3Nb2/3)O3-PbTiO3 single crystals under uniaxial mechanical stress.* Journal of Applied Physics, 2012. **111**(8):.

124. Dong, W.D., et al., *Stress dependence of thermally driven pyroelectric charge release during FER-FEO phase transformations in 011 cut relaxor ferroelectric crystals.* Applied Physics Letters, 2012. **100**(26): 262909.

125. Gallagher, J.A. and Lynch, C.S., *Characterization of ferroelectric single crystals with field induced phase transformations.* Smart Materials and Structures, 2013. **22**(9): 094004.

126. Gallagher, J.A. and Lynch, C.S., *Combining experiments and modeling to characterize field driven phase transformation in relaxor ferroelectric single crystals.* Acta Materialia, Submitted: July, 2014.

127. Bai, F.M., et al., *Domain engineered states over various length scales in (001)-oriented Pb(Mg1/3Nb2/3)O3-x%PbTiO3 crystals: Electrical history dependence of hierarchal domains.* Journal of Applied Physics, 2005. **97**(5).

128. Zhao, Z.Z., et al., *Modeling 180 degrees Domain Switching Population Dynamics in Polycrystalline Ferroelectrics.* Journal of the American Ceramic Society, 2012. **95**(5): 1619-1627.

129. Davis, M., et al., *Direct piezoelectric effect in relaxor-ferroelectric single crystals.* Journal of Applied Physics, 2004. **95**(10): 5679-5684.

130. Li, F., et al., *Composition and phase dependence of the intrinsic and extrinsic piezoelectric activity of domain engineered (1-x)Pb(Mg1/3Nb2/3)O3-xPbTiO3 crystals.* Journal of Applied Physics, 2010. **108**(3): 034106-9.